

# Atmospheric Pressure Dielectric Barrier Discharges for the Surface Modification of Polypropylene

A Thesis Submitted in Partial Fulfilment of the Requirements for  
the degree of Doctor of Philosophy in the  
School of Engineering of  
Manchester Metropolitan University

By Lukas Josef Wilfried Seidelmann

Faculty of Science & Engineering  
Surface Engineering Group

December 2015

## **Declaration**

This is to certify that the material contained in this thesis has been produced by author and has not been accepted in substance for any other degree and is not currently submitted in candidature for any other academic award.

## Acknowledgement

First of all; I would like to thank my Director of Studies Prof Peter Kelly for giving me the opportunity to study in Manchester, for his continuous support and guidance and for providing an excellent atmosphere for research.

I want to express my gratitude to Prof James Bradley and Dr James Walsh from the University of Liverpool for providing the high voltage power supply for this project. Many thanks goes also to Dr Ziad Banyamin and Dr Vladimir Vishnyakov from the Manchester Metropolitan University for helping to understand the high voltage power supply and the frequent repairs.

I am grateful to Dr Simon Read, Dr Jamie Moffat, Lyndsay Armstrong, Darren Jackson, Jack Proudlock and Matthew Scott from Innovia Films Ltd. for the industrial surface treatment of the BOPP films and the helpful discussions.

Many thanks go to Anthony Dickenson and Stanley Wright of the Advanced Manufacturing Team of the Manchester Metropolitan University for their advices and for the manufacturing of the different parts of the laboratory DBD system.

Furthermore, I want to thank the students and the members of the Surface Engineering Group of the Manchester Metropolitan University for the friendly atmosphere and the exchange of ideas, in particular Antony, Brice, Carolin, Glen, Justyna, Marina, Nessima, Soheyla and Ziad.

Special thanks goes to my wife Marlene for being patient over three years and for standing by my side even if a distance of 1200 kilometres separated us.

## Abstract

Polypropylene films are widely used as packaging materials for foodstuffs, since they offer excellent barrier properties against polar substances, high elasticity, mechanical strength, transparency and chemical stability. However, the relatively low surface energy of polypropylene represents a major issue for the adhesion of printing inks and labels. To improve printability it is necessary to perform a surface activation process.

In the presented work, the atmospheric pressure dielectric barrier discharge (DBD) in nitrogen is investigated as a surface treatment method to increase the surface energy of biaxially orientated polypropylene foils. This technology creates a non-thermal plasma by applying strong electrical fields to a gas between two electrodes. The reactive species of the plasma forms new electronegative chemical groups on the surface and also etches the surface of the substrate. Both effects lead to an increase of the surface energy of the plasma treated polymer films. The crosslinking of polymer chains is also a possible effect caused by the plasma treatment.

A new plasma rig was designed for this project, including a closed plasma chamber, two different parallel electrode configuration (flat or sawtooth electrodes) and a reel-to-reel system for the transport of the polypropylene foil. The designed system allows to adjust the sizes of the gas gap and the thickness of the dielectric. In addition, the plasma chamber can be filled with every gas or gas mixture wanted.

A D-optimal design of experiments approach was utilised to study the influence of the power applied to the electrodes, the size of the gas gap and the thickness of the dielectric on the wettability of the treated polymer films. Furthermore, a flat electrode and a sawtooth electrode configuration are compared to each other. The findings of this work clearly indicate that the sawtooth electrode configuration is superior regarding the consumed electrical power and the wettability of the treated films. The optimal setting for the plasma treatment with the sawtooth electrode configuration are a low gas gap and a high power applied to the electrodes. The thickness of the dielectric has no influence on the wettability of the treated film. However, the increase of the dielectric thickness leads to an increase of the consumed power.

These findings were transferred to an industrial process, where the polymer foils were treated in a nitrogen atmosphere with admixtures of CO<sub>2</sub>, N<sub>2</sub>O and C<sub>2</sub>H<sub>2</sub> in the ppm range under the founded optimal conditions. A significant difference in the surface energies of these samples

could not be identified by contact angles measurement, but all samples showed a significantly reduced hydrophobic recovery rate in comparison to samples treated by the in the industry more conventional plasma treatment in air. The DBD surface treatment in nitrogen is therefore an important improvement for the industrial production, because the treated packaging foils can be stored longer before they are processed further without the need to refresh the surface treatment. The low hydrophobic recovery of the samples treated in the nitrogen plasma is connected to an intensified crosslinking of the polymer chains on the surface of the treated polypropylene films.

# Contents

<b>Declaration .....</b>	<b>I</b>
<b>Acknowledgement.....</b>	<b>II</b>
<b>Abstract.....</b>	<b>III</b>
<b>Contents .....</b>	<b>V</b>
<b>List of Figures .....</b>	<b>VIII</b>
<b>List of Tables.....</b>	<b>XI</b>
<b>Nomenclature.....</b>	<b>XII</b>
<b>1 Introduction .....</b>	<b>1</b>
1.1 Motivation .....	1
1.2 Research aims and contributions .....	3
1.3 Structure of the thesis.....	3
<b>2 Physical fundamentals of gas discharges.....</b>	<b>6</b>
2.1 Non-equilibrium and equilibrium plasmas.....	6
2.2 Townsend criterion for breakdown.....	9
2.3 Breakdown voltage and Paschen's Law.....	10
2.4 Discharge regimes at low pressure .....	12
<b>3 Polypropylene.....</b>	<b>16</b>
3.1 Chemical structure and properties .....	16
3.2 Uniaxial orientated polypropylene and biaxially orientated polypropylene .....	18
<b>4 The dielectric barrier discharge .....</b>	<b>23</b>
4.1 Surface and volume discharge configurations of dielectric barrier discharges ...	23
4.2 Dielectric Barrier Discharge regimes.....	26
4.2.1 The filamentary discharge .....	26
4.2.2 The space charge field of an electron avalanche .....	28
4.2.3 Discharge by Townsend or streamer mechanism .....	29
4.2.4 Atmospheric pressure glow and Townsend discharges .....	31
4.3 Interactions of the DBD nitrogen plasma with the polymer surface .....	35
<b>5 Design of the laboratory scale DBD rig.....</b>	<b>38</b>
5.1 Design of the process chamber .....	38
5.2 Reel-to-reel system with smooth profile parallel electrode configuration.....	39

---

5.3	Parallel electrode configuration with sawtooth electrode profile .....	42
5.4	Overall view on the gas chamber with reel-to-reel system and electrode configuration.....	44
5.5	High voltage power supply of the laboratory scale system and measurement of the electrical characteristics.....	45
5.6	Setup of the industrial scale DBD system.....	47
<b>6</b>	<b>Analytical techniques .....</b>	<b>49</b>
6.1	Lissajous figures .....	49
6.2	Contact angle measurement using the sessile drop method .....	52
6.3	X-ray photoelectron spectroscopy .....	56
<b>7</b>	<b>Design of Experiments: The D-optimal approach .....</b>	<b>58</b>
7.1	Principles of the design of experiment.....	58
7.2	The different regression models and the estimation of the regression coefficients .....	60
7.3	The basic experimental designs .....	62
7.4	The D-optimal design.....	64
<b>8</b>	<b>Factor analysis for the design of experiment .....</b>	<b>66</b>
8.1	Theoretical reflection of possible factors.....	66
8.2	The influence of the set function of the function generator on the voltage applied .....	67
8.3	The influence of the frequency on the electrode voltage .....	68
8.4	Dependence of the optimal frequency on the capacitance of the electrode configuration and selection of the dielectric .....	70
8.4.1	The rewind speed of the film during the treatment.....	75
8.5	The response of the experimental array and the principle surface treatment analysis process .....	76
<b>9</b>	<b>The experiment of the laboratory scale DBD system.....</b>	<b>79</b>
9.1	The design of experiments for the flat electrode configuration .....	79
9.2	The design of experiments for the sawtooth electrode configurations .....	85
9.3	Comparison of the two electrode configurations.....	94
<b>10</b>	<b>Investigation of electrical measurements during the discharge .....</b>	<b>98</b>
10.1	Observation of the voltage applied to the electrode configurations and discharge current.....	98
10.2	Analysis of the Lissajous figures: the applied power .....	100
10.3	Analysis of the Lissajous figures: Investigation of the minimum voltage for the ignition of the plasma.....	106

---

10.4	Calculation of the power applied to the gas in the gas gap of the sawtooth electrode configuration.....	109
<b>11</b>	<b>Investigation of the BOPP films treated in nitrogen with admixtures .....</b>	<b>116</b>
11.1	The surface energy of the treated BOPP films treated on the industrial DBD system.....	116
11.2	Results of the XPS measurements .....	120
11.3	Films treated with higher concentrations of the admixtures .....	125
<b>12</b>	<b>Conclusions .....</b>	<b>131</b>
<b>13</b>	<b>Future work .....</b>	<b>133</b>
<b>14</b>	<b>References .....</b>	<b>134</b>
	<b>Appendix A: Circuit diagram of the amplifier .....</b>	<b>144</b>
	<b>Appendix B: Matlab program code for the low-pass filter .....</b>	<b>145</b>
	<b>Appendix C: Matlab program code for calculating the phase difference.....</b>	<b>146</b>
	<b>Appendix D: Error calculation for the surface energy .....</b>	<b>147</b>

## List of Figures

Figure 1: Evolution of the free electron temperature $T_e$ and of the heavy particles temperature $T_g$ with the pressure in a mercury plasma arc [6].....	7
Figure 2: Different plasmas with their electron temperatures and plasma densities [8]...	8
Figure 3: Development of an electron avalanche in an uniform electrical field [10].....	9
Figure 4: Breakdown voltage of different gases as a function of the pressure, $p$ , and electrode distance, $d$ , in a parallel plate configuration [11].....	11
Figure 5: Characteristic current-voltage diagram for low pressure DC discharges [12]	13
Figure 6: Polypropylene with 1-methylethylane as repeating unit.....	17
Figure 7: Atactic, isotactic and syndiotactic configuration of polypropylene.....	17
Figure 8: Mechanical, optical and barrier properties of BOPP and cast PP films with a thickness of 25 $\mu\text{m}$ in each case in machine direction (MD) and transverse direction (TD) according to [18].....	19
Figure 9: The three-layer structure BOPP film investigated in this project.....	22
Figure 10: Different dielectric barrier discharge configurations for surface and volume discharges according to [14, 45].....	24
Figure 11: Industrial DBD configuration for the surface treatment of polymer foils ....	25
Figure 12: Single streamer (left picture) and a multitude of streamers (right picture) of the filamentary discharge in nitrogen at atmospheric pressure.....	26
Figure 13: Single microdischarge channel of a filamentary discharge according to [46]	27
Figure 14: Space charge field of a single electron avalanche according to [10].....	28
Figure 15: Development of the Townsend discharge according to [10].....	29
Figure 16: Development of the filamentary discharge in the manner of the streamer mechanism according to [10].....	30
Figure 17: Discharge current of the filamentary and the Townsend discharge in nitrogen from [68].....	35
Figure 18: Dielectric barrier discharge plasma chamber.....	39
Figure 19: Design of the parallel electrode configuration with smooth surfaces.....	40
Figure 20: Reel-to-reel system.....	41
Figure 21: Pathway of the BOPP film during the plasma treatment.....	41
Figure 22: The three different sawtooth electrodes used in this project with 1, 3 and 5 teeth.....	43
Figure 23: Reel-to-reel system with sawtooth electrode configuration.....	44
Figure 24: Reel-to-reel system with flat electrode configuration inside the vacuum chamber.....	45
Figure 25: Experimental setup of the laboratorial scale DBD system.....	47
Figure 26: Industrial DBD system in open position.....	48
Figure 27: Idealised Lissajous figure of a DBD driven by sinusoidal voltage.....	50
Figure 28: Contact angle between the liquid and solid phase.....	52
Figure 29: Good and poor wettability indicated by use of a Dyne pen with a surface energy of 38 $\text{mN/m}$ to a BOPP film with untreated and plasma treated regions	55
Figure 30: Experimental design by changing only one separate value at a time without reaching the optimal response area according to [110].....	58

---

Figure 31: Symmetrical distribution of experiments around the standard reference experiment as centre point of an experimental array with three factors on two levels .....	59
Figure 32: The full factorial, the fractional and the central composite design for an experimental array with three factors on two levels.....	63
Figure 33: Two level full factorial Taguchi design with three-factor inner array and two-factor outer arrays.....	64
Figure 34: Influence of the set function of the function generator on the voltage applied to the electrode configuration .....	68
Figure 35: Influence of the frequency on the amplitude of the applied voltage .....	69
Figure 36: Dependence of the optimal frequency on the air gap distance and the kind of dielectric covering one electrode .....	70
Figure 37: Optimal frequency plotted against the product of inductivity, $L$ , and the capacitance of the electrode configuration, $C_{conf}$ .....	72
Figure 38: Measurement of the rewind speed of the film with different sizes of the gas gap and varies voltages applied to the DC motor.....	75
Figure 39: Investigation of a treated sample with contact angle and Dyne Inks and Pens.....	78
Figure 40: Influence of the current on the water contact angle for the flat electrode configuration .....	82
Figure 41: Influence of the dielectric thickness on the water contact angle for the flat electrode configuration .....	82
Figure 42: Influence of the gas gap size on the water contact angel for the flat electrode configuration .....	83
Figure 43: Influence of the current set on the DC power supply and the thickness of the dielectric on the water contact angle of the treated BOPP samples calculated for a constant gas gap of 2.0 mm. ....	84
Figure 44: Influence of the current set on the DC power supply and the size of the gas gap on the water contact angle of the treated BOPP samples calculated for a constant dielectric thickness of 1.26 mm.....	84
Figure 45: Influence of the current on the water contact angle for the sawtooth electrode configurations.....	88
Figure 46: Influence of the gas gap size on the water contact angle for the sawtooth electrode configurations.....	88
Figure 47: Sample of experiment 4 treated with the 5 tooth sawtooth electrode configuration .....	89
Figure 48: Sample of experiment 6 treated with the 5 tooth sawtooth electrode configuration .....	90
Figure 49: Sample of experiment 7 treated with the 5 tooth sawtooth electrode configuration .....	90
Figure 50: Plasmas of experiment 1 (left) and 4 (right) without applied BOPP film (five teeth electrode).....	92
Figure 51: Plasmas of experiment 1 (left) and 4 (right) with applied BOPP film (five teeth electrode).....	92
Figure 52: Plasmas of experiment 9 (left) and 5 (right) without applied BOPP film (five teeth electrode).....	93

Figure 53: Arc discharges ignited at both ends of the sawtooth electrode with one tooth, bypassing the dielectric .....	94
Figure 54: Measured voltage applied to the five tooth electrode configuration and the resulting discharge current for experiment 1 of the corresponding experimental array .....	98
Figure 55: Measured voltage applied to the flat electrode configuration and the resulting discharge current for experiment 1 of the corresponding experimental array .....	99
Figure 56: Lissajous figure of the experimental array of the five tooth electrode with the settings of experiment 1 .....	101
Figure 57: Lissajous figure of the experimental array of the flat electrode configuration with the settings of experiment 1 .....	101
Figure 58: Influence of the current on the consumed electrical power for the flat electrode configuration .....	102
Figure 59: Influence of the dielectric thickness on the consumed electrical power for the flat electrode configuration .....	103
Figure 60: Influence of the gas gap size on the consumed electrical power for the flat electrode configuration .....	103
Figure 61: Influence of the current on the consumed electrical power for the sawtooth electrode configurations.....	104
Figure 62: Influence of the dielectric thickness on the consumed electrical power for the sawtooth electrode configurations .....	104
Figure 63: Minimum voltage for the ignition of the plasma and the effective voltage applied to the electrode configuration with the five tooth sawtooth electrode depending on the thickness of the dielectric .....	108
Figure 64: Discharge and displacement current of experiment 1 of the experimental array with the five tooth sawtooth electrode configuration .....	112
Figure 65: Calculation of the plasma current by the subtraction of the displacement current from the discharge current of experiment 1 of the experimental array with the five tooth sawtooth electrode configuration .....	112
Figure 66: Influence of the current setting on the discharge power for the sawtooth electrode configuration with five teeth.....	113
Figure 67: Influence of the dielectric thickness on the discharge power for the sawtooth electrode configuration with five teeth .....	113
Figure 68: Extension of the electrical field by increasing the dielectric thickness for the sawtooth configuration with one tooth visible through the ignition of additional filaments .....	115
Figure 69: The polar part, the dispersive part and the surface energy of the BOPP films treated by the industrial DBD system with admixtures of acetylene .....	117
Figure 70: The polar part, the dispersive part and the surface energy of the BOPP films treated by the industrial DBD system with admixtures of nitrous oxide.....	118
Figure 71: Surface energy versus time data for the BOPP samples treated by the industrial DBD system.....	119
Figure 72: XPS wide scan of BOPP sample treated in pure nitrogen.....	120
Figure 73: XPS narrow scan (Carbon 1s) of the BOPP sample treated in pure nitrogen.....	121

Figure 74: XPS narrow scan (Nitrogen 1s) of the BOPP sample treated in pure nitrogen .....	121
Figure 75: XPS narrow scan (Oxygen 1s) of the BOPP sample treated in pure nitrogen	122
Figure 76: Nitrogen and oxygen content of the samples treated by the industrial DBD system with the reactive gas acetylene .....	123
Figure 77: Nitrogen and oxygen content of the samples treated by the industrial DBD system with the reactive gas nitrous oxide .....	123
Figure 78: The polar part, the dispersive part and the surface energy of the BOPP films treated by the laboratory DBD system with admixtures of acetylene .....	126
Figure 79: The polar part, the dispersive part and the surface energy of the BOPP films treated by the laboratory DBD system with admixtures of nitrous oxide .....	126
Figure 80: The polar part, the dispersive part and the surface energy of the BOPP films treated by the laboratory DBD system with admixtures of carbon dioxide.....	127
Figure 81: Aging behaviour of the BOPP samples treated in nitrogen with the laboratory DBD system .....	128

## List of Tables

Table 1: The different stretching technologies, their equipment and products .....	20
Table 2: The various applications of BOPP as plain film and multilayer structure with the used range of thickness .....	22
Table 3: Breakdown voltage, mean free pathway for electrons and first ionisation energy for different gases at atmospheric pressure according to [10].....	32
Table 4: Different characteristics and conditions for the Atmospheric Pressure Townsend Discharge and the Atmospheric Pressure Glow Discharge [56].....	34
Table 5: Electron-molecule collision processes [51] .....	36
Table 6: Total surface energy, the polar and dispersive part of the testing liquids [109]	54
Table 7: Relative permittivity and breakdown strength of different ceramics [118] .....	74
Table 8: Experimental design for the flat electrode configuration with the optimal frequency at which the experiments were performed.....	81
Table 9: Design of experiment for the sawtooth electrode configurations .....	86
Table 10: The optimal frequencies used for the different sawtooth electrode configurations.....	87
Table 11: Different pressure settings for the nitrogen gas line and the gas cartridge for achieving the different concentrations of the admixtures in the nitrogen gas ..	125
Table 12: Characteristics for the rough estimation of the energy densities of the surface treatments with the laboratory and the industrial DBD system .....	130

## Nomenclature

### List of Abbreviations

AC	Alternating current
APGD	Atmospheric Pressure Glow Discharge
APTD	Atmospheric Pressure Townsend Discharge
ATR-FTIR	Attenuated total reflection Fourier transform infrared spectroscopy
BOPP	Biaxially oriented polypropylene
DBD	Dielectric barrier discharge
DC	Direct current
DoE	Design of Experiments
EVOH	Ethylene vinyl alcohol
LMWOM	Low molecular weight oxidised molecules
PA	Polyamides
PECVD	Physical enhanced chemical vapour deposition
PET	Polyethylene terephthalate
PP	Polypropylene
PVDC	Polyvinylidene chloride
PVOH	Polyvinyl alcohol
XPS	X-ray photoelectron spectroscopy

### Greek letters

$\alpha$	Townsend first ionisation coefficient	[1/m]
$\beta$	Townsend secondary ionisation process	[-]
$\gamma_l$	Surface energy of the test liquid	[mN/m]
$\gamma^d$	Dispersive part of the surface energy of the liquid	[mN/m]
$\gamma^p$	Polar part of the surface energy of the liquid	[mN/m]
$\gamma_s$	Surface energy of the solid substrate	[mN/m]
$\gamma_s^d$	Dispersive part of the surface energy of the solid	[mN/m]
$\gamma_{sl}$	Interfacial tension of the solid and liquid phase	[mN/m]
$\gamma_s^p$	Polar part of the surface energy of the solid	[mN/m]
$\varepsilon$	Permittivity of the vacuum	[F/m]

$\varepsilon_i$	Relative permittivity of an insulator	[-]
$\Theta$	Contact angle	[degree]
$\lambda$	Mean free pathway	[m]
$\varphi$	Phase angle	[degree]

### Latin letters

$A$	Constant in the Paschen's law	[V/Pam]
$A_E$	Electrode area	[m <sup>2</sup> ]
$A_{dis}$	Discharge area	[m <sup>2</sup> ]
$B$	Constant in the Paschen's law	[-]
$c_{conf}$	Capacitance of the DBD configuration	[F]
$c_d$	Capacitance of the solid dielectric	[F]
$c_g$	Capacitance of the gas	[F]
$c_i$	Capacitance of an insulator between two electrodes	[F]
$c_{meas}$	Capacitance of the measurement capacitor	[F]
$d$	Size of the gas gap	[m]
$d_i$	Thickness of the insulator	[m]
$E_0$	Applied electrical field between two electrodes	[V/m]
$E_a$	Space charge field of an electron avalanche	[V/m]
$f$	Frequency	[Hz]
$f_0$	Resonant frequency	[Hz]
$h$	Width of the electrode	[m]
$I_{plasma}$	Plasma current	[A]
$L$	Inductivity	[H]
$p$	Pressure	[Pa]
$P_d$	Discharge power	[W]
$P_{el}$	Electrical power	[W]
$q$	Electrical charge	[C]
$T$	Cycle duration	[T]
$t$	Time	[s]
$T_e$	Electron temperature	[K]
$T_g$	Heavy particle temperature	[K]

---

$v$	Speed of the polymer film	[m/s]
$V$	Voltage	[V]
$V_a$	Voltage applied to the electrode configuration	[V]
$V_b$	Breakdown voltage	[V]
$V_d$	Voltage drop across the measurement capacitor	[V]
$V_{die}$	Voltage drop over the dielectric layer	[V]
$V_{eff}$	Effective voltage	[V]
$V_{gap}$	Gas gap voltage	[V]
$V_{min}$	Minimum voltage to ignite a DBD	[V]
$W_d$	Energy density	[W/m <sup>3</sup> s]
$W_{el}$	Electrical energy	[J]
$W_{kin}$	Kinetic energy	[J]

# 1 Introduction

## 1.1 Motivation

Polymers are often the material of choice for the manufacturing of a wide range of products because of their numerous valuable properties and their relatively low cost. The variety of different kinds of plastics and their diverse physical bulk properties, such as mechanical strength, chemical resistance or elasticity, make it possible to find suitable materials for many applications. However, in most cases the surface properties do not meet the necessary requirements and need a specific treatment, which adds functionalities to the surface without changing the bulk properties. For example, polyolefins suffer from the problem, that their adhesion and wettability to hydrophilic substances is very low. This causes problems such as low printability, delamination and poor bonding to coatings and adhesives. It is estimated, that about 70% of the total plastics produced require a surface modification technique before they can be processed further [1].

There are several methods, which are currently used for surface treatment and include: chemical treatment, flame treatment and plasma treatment. In all cases the surface energy of the polymer is increased by insertion of electronegative chemical groups into the surface. In addition, the surface also often becomes etched. The etching removes amorphous regions of the polymer, while crystalline parts stay largely unaffected. This effect leads to increased roughness, which also improves the adhesion of water-based inks or glues to the polymer by capillary action.

For chemical treatments, the polymer is immersed into a solution including different acids, bases or chlorinating agents, which oxidise and etch the surface of the polymer, but can also penetrate into the polymer and change the bulk properties. Another problem is the huge amount of solvent waste produced, which is expensive to dispose of and is often ecologically damaging.

Flame treatments use mixtures of oxygen and hydrocarbon gas to create oxidising flames close to the polymer surface. The process is hard to control and it is imperative to find the right treatment properties for the respective substrate. Over-treatment damages the surface, while insufficient application of this technology does not increase the surface energy of the polymer sufficiently [2, 3].

The term plasma treatment includes low pressure and atmospheric pressure plasma surface treatments. Both technologies utilize strong electrical fields, which create electrical discharges in gases. During the discharge, excited gas particles are generated. They react immediately with the polymer surface where new functional groups are formed. The creation of free radical sites on the plastic surface leads to crosslinking of polymer chains, which also increases the surface energy.

The low-pressure method uses an inert gas atmosphere with admixtures of oxygen under vacuum conditions (1mTorr – 1Torr) and an excitation by direct current (DC) or alternating current (AC) with radio or microwave frequency. The treatment creates a homogenous plasma and is one of the most effective processes in regards to treatment time and increased surface energy. However, the expensive vacuum equipment, such as pumps and vacuum chamber, and the difficulty of implementation of in-line production make this technology unsuitable for industrial manufacturing.

The atmospheric pressure plasma method, which is also known as corona treatment, is created by AC at hertz to kilohertz frequencies applied in air at atmospheric pressure. The corona treatment consists of two electrodes; one of these is covered with a dielectric material. The technical setup is thus very similar to the dielectric barrier discharge (DBD). This treatment method is used in this project. However, it is only possible to create non-uniform plasmas with a corona treatment. Another problem is the creation of low molecular weight oxidised molecules (LMWOM) on the polymer surface, which form a loosely bonded layer on the surface. This layer increases the surface energy of the polymer, but can be easily removed through polar solvents, causing hydrophobic recovery and delamination of coatings, printing inks or adhesives [2, 3].

The DBD is a cheap alternative to the low-pressure plasma and is in addition suitable for reel-to-reel production in industry, because it works at atmospheric pressure like the corona treatment. The problem of LMWOM can be prevented by removing oxygen from the process through the use of nitrogen instead. Small admixtures of reactive gases such as carbon dioxide, nitrous oxide or acetylene can also be added to form different chemical groups on the surface of the treated polymer [4].

## 1.2 Research aims and contributions

The aim of this PhD-project was to investigate the DBD in nitrogen gas at atmospheric pressure as a surface treatment method for polyolefin packaging foils. This plasma technology offers the possibility of enhancing or replacing existing industrial methods, which are currently utilised.

The DBD technology was implemented first on the laboratory scale. Suitable factors, which influence the surface treatment process, were identified and then optimised regarding the enhanced wettability of the plasma treated films and the electrical power consumption. For the optimisation a D-optimal design of experiments was utilised. The findings were afterwards transferred to the industrial process, where admixtures like nitrous oxide, carbon dioxide and acetylene were added to the nitrogen gas. The admixtures should influence the types of chemical groups, which were incorporated by the plasma treatment into the surface of the treated packaging foils, and thus the surface energy of the treated polymer films.

The treated substrates were investigated by contact angle measurements with different test liquids and X-ray photoelectron spectroscopy to identify the elements incorporated by the plasma treatment and to study the effects to the surface energy. The surface energy of the treated films was also observed over a longer period of time by measuring the contact angles over 30 days to estimate the time stability and the hydrophobic recovery rate.

## 1.3 Structure of the thesis

This thesis is divided into the parts: theoretical background, experimental set-up, methods and procedures, results and discussion and as the final part, the conclusion. The theoretical background comprises Chapter 1 to 4 and introduces the polypropylene substrate, which is treated by the DBD and gives detailed information about the physical principles of gas discharges. Furthermore, the DBD technology and the different discharge regimes, which can be ignited with the DBD technology, are explained.

The experimental setup is presented in Chapter 5 and includes the designed plasma rig with the vacuum chamber, the reel-to-reel system, the different electrode configurations and the high voltage power supply. In addition, also the utilised industrial DBD systems is introduced. Chapter 6 and Chapter 7 explain the used methods and procedures to investigate the treated polymer foils and to analyse the discharge power during the plasma treatment. That

includes X-ray photoelectron spectroscopy (XPS) and contact angle measurement, as well as the necessary equations for the calculation of the surface energy of the investigated polymer foils. The diagnostic tool “Lissajous figures” for the electrical parameters during the discharge is also explained in Chapter 6. Chapter 7 introduces the Design of Experiments (DoE) approach and explains the benefits of the D-optimal design.

The results and discussion part can be found in the Chapters 8, 9, 10, and 11. An extensive description of the obtained results of the conducted experiments is given. The conclusion can be found in Chapter 12, which summarizes the main findings of the results and discussion part. This thesis ends with suggestions for future research aims.

A more detailed description of the individual chapters is given in the following:

**Chapter 1:** Gives an overview of the different surface treatment methods for increasing the surface energy of polyolefin packing foils and explains their drawbacks in comparison to the DBD technology. Additionally, the aim and the approach of this PhD project are listed.

**Chapter 2:** Describes, how gas discharges are ignited by strong electrical fields. The physical fundamentals and the necessary conditions, as well as the different discharge regimes at low pressure are explained.

**Chapter 3:** Introduces the polypropylene substrate, which is surface treated during this project. The structure from the monomer to the multilayer packaging foil is presented. The various orientation technologies and their relevance for polypropylene films is explained

**Chapter 4:** Discusses the DBD technology for surface and volume discharges. The different discharge regimes and their mechanisms are presented.

**Chapter 5:** Introduces the custom designed laboratory DBD system. The gas chamber, the reel-to-reel system, the various electrode configurations and the associated high voltage power supply are explained. Furthermore, the production scale DBD system is also described here.

**Chapter 6:** Reviews the different measurement and analytical methods utilised during this project. This includes the Lissajous figures, contact angle measurement and the X-ray photoelectron spectroscopy.

**Chapter 7:** Introduces the basics of the ‘design of experiments’ approach and explains the advantages of the D-optimal designs.

**Chapter 8:** Describes the first experiments utilising the laboratory DBD system, which were undertaken to identify suitable factors for the optimisation of the plasma treatment.

**Chapter 9:** Presents the results of the D-optimal experimental arrays for the flat electrode configuration and the sawtooth electrode configurations with the factors: size of the gas gap, thickness of the dielectric and current setting on the DC power supply.

**Chapter 10:** Discusses the influence of the factors on the consumed power during the plasma treatment. Especially, the impact of the dielectric thickness is investigated in detail.

**Chapter 11:** Introduces the results of the packaging films treated by the industrial DBD system in nitrogen and nitrogen with admixtures up to a concentration of 100 ppm. The hydrophobic recovery of these films was observed over 30 days. The films treated by the industrial and the laboratory DBD system are compared regarding their aging behaviour.

**Chapter 12:** Summarises the results and the findings of this PhD-project

**Chapter 13:** Suggests possibilities for further research aims regarding the surface treatment of polyolefin foils in nitrogen plasmas

**Appendix A:** Illustrates the circuit diagram of the amplifier utilised in the laboratory DBD system

**Appendix B:** Presents the Matlab program code for the low-pass filter

**Appendix C:** Contains the Matlab program code for calculating the phase difference between two sinusoidal signals

**Appendix D:** Offers the equations used to calculate the error of the polar part, the dispersive part and the entire surface energy

## 2 Physical fundamentals of gas discharges

Plasma is besides solid, liquid and gas regarded as the fourth state of matter. Plasma makes up more than 99% of the visible matter in the universe. It is a gaseous mixture of negative and positive ions, excited atoms or molecules, their electrically neutral forms, electrons and photons. The amount of negative and positive charged particles is equal, so it is overall quasi-neutral. The transition from the gas to the plasma state is reached by applying electromagnetic radiation, thermal or electric energy to the gas. Depending on the gas pressure, the type and the amount of energy transferred to the gas, different categories of plasmas are established. They are classified into the nonthermal equilibrium plasmas and thermal equilibrium plasmas. This chapter discusses how these two kinds of plasma states are established by electrical fields and their physical fundamentals.

### 2.1 Non-equilibrium and equilibrium plasmas

Free electrons and ions are present in every gas. They are created via ionisation processes caused by cosmic or radioactive radiation, as well as UV-light. There are around  $10^7$  of electron-ion pairs present per second in one cubic metre of any gas at atmospheric pressure [5]. These free electrons are important for the initiation of the electrical breakdown and are therefore called seed electrons. If an electrical field is supplied to a gas, the Coulomb force accelerates the seed electrons towards the anode. The kinetic energy,  $W_{kin}$ , gained during the acceleration is dependent on the mean free pathway,  $\lambda$ , the electrical charge,  $q$ , and the strength of the electrical field,  $E$ , as shown in Equation 1. The acceleration is interrupted when the electron collides with a heavy gas particle. Particles without charge are not directly affected by the electrical field.

$$W_{kin} = q \cdot E_0 \cdot \lambda \quad (1)$$

As a result of the extreme mass difference between electrons and ions, electrons receive much more kinetic energy through the electrical field. As pressure increases, the amount of transferred energy from the electrical field to ions becomes more and more negligible. However, this difference of energy between electrons and heavy particles can be compensated

for by transferring energy through collisions. Thermal equilibrium between heavy particles and electrons is reached, if the two species have the same energy.

Electrons transfer their kinetic energy directly to the heavy particles by elastic collisions. This mode of energy transfer is ideal if the collision partners have the same mass. This is not the case here. Thus, electrons are only able to transfer small amounts of their kinetic energy with each collision, meaning that it is necessary for a large number of elastic collisions to occur for attainment of thermal equilibrium. This is only possible if the gas pressure is high enough. On the one hand, a lower gas pressure is beneficial, because the mean free pathway is than increased and the electrons are able to reach higher kinetic energies. On the other hand, if the gas pressure is too low, collisions between electrons and heavy gas particles are too rare to ensure enough energy is transferred and thermal equilibrium is not established. This correlation is illustrated in Figure 1, where the temperatures of the free electrons and of the heavy particles in a mercury plasma arc are shown as functions of the gas pressure. The thermal equilibrium is in this case established after reaching a pressure of around 10 kPa.

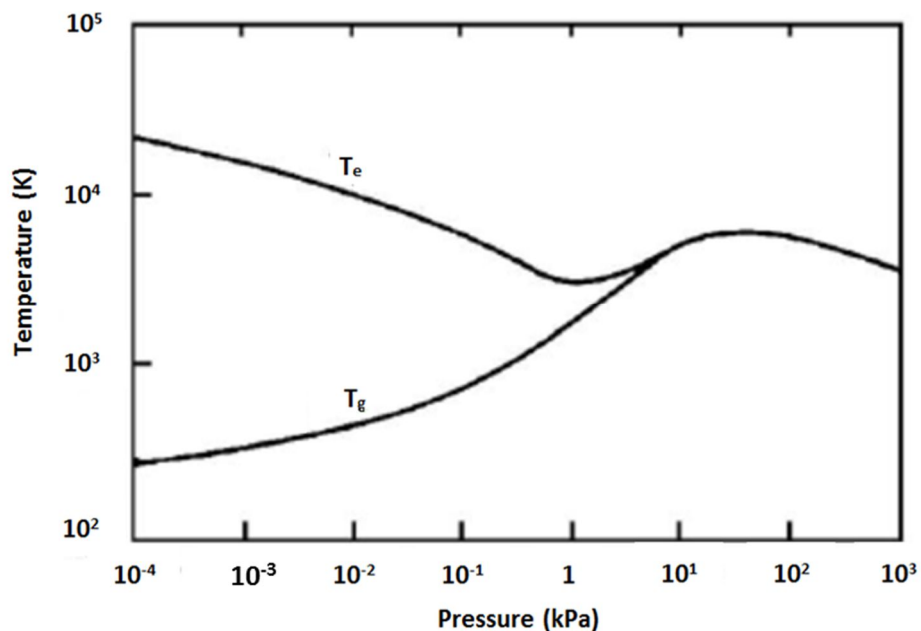


Figure 1: Evolution of the free electron temperature  $T_e$  and of the heavy particles temperature  $T_g$  with the pressure in a mercury plasma arc [6]

Besides the elastic collisions, inelastic collision between electrons and heavy particles are also possible. These collisions create the reactive species of the plasma; the ions and excited states. The accelerated electrons thereby transfer their kinetic energy to one of the bonding electrons of a heavy particle. The bonding electron is then converted from its ground energy state to a higher state or even released completely. The products of this process are free radicals, electrons and ions. As there are more collisions in general between electrons and heavy particles at higher pressures, these plasmas contain more ions and free electrons [5, 7].

It can be summarised that plasmas at higher pressures are more likely to be hot plasmas at thermal equilibrium. The temperature of their free electrons and heavy particles is the same and amounts to about 10 000 K. A typical example is the arc plasma. In contrast, non-equilibrium plasmas are cold plasmas. The temperature of the heavy particles reaches values between 300 K and 1000 K and is considerably lower than the temperature of the free electrons, which range between 10 000 K and 100 000 K. Furthermore, the electron density of non-thermal plasmas is lower than that of thermal plasmas. A typical example of a non-thermal plasma is the glow discharge. Figure 2 shows different examples of non-thermal and thermal plasmas, their electron temperatures and plasma densities [8, 9].

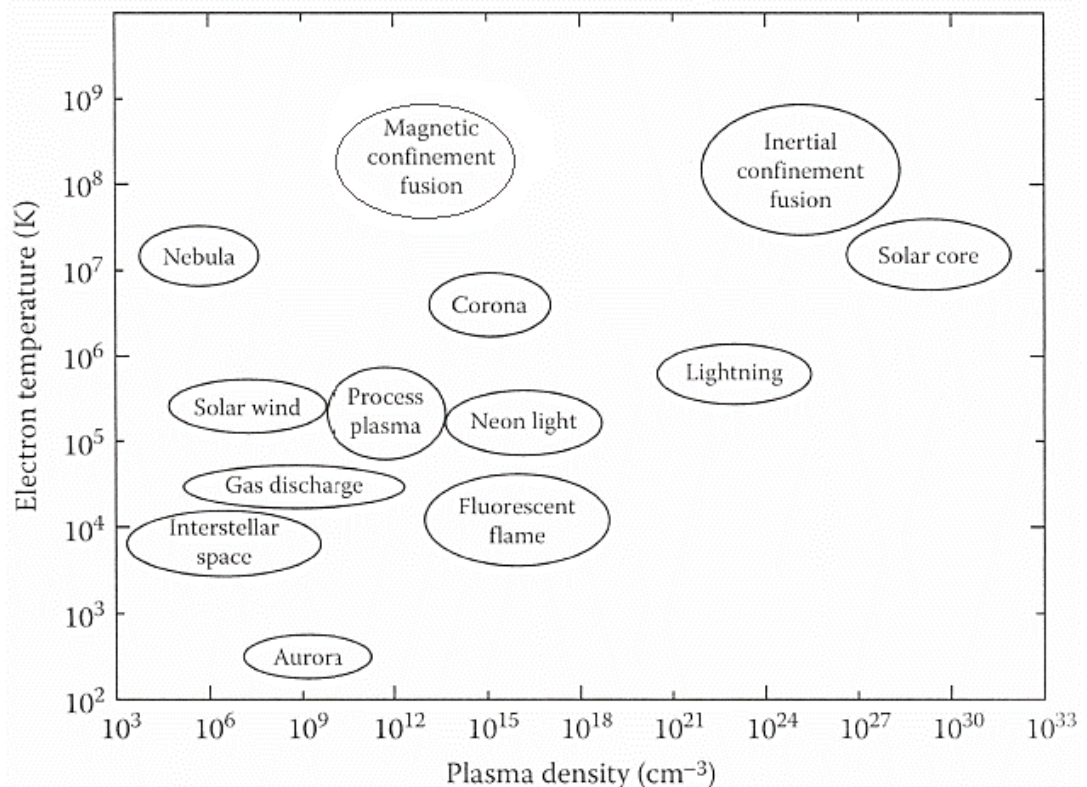


Figure 2: Different plasmas with their electron temperatures and plasma densities [8]

## 2.2 Townsend criterion for breakdown

If a voltage is applied across two parallel electrodes, which are separated by a gas gap, a discharge initially occurs, when the applied voltage exceeds the breakdown voltage. The gas changes from an insulator to a conductor through the creation of free electrons and ions, which are free charge carriers. The mechanism corresponds to the ionisation process by inelastic collision between free electrons and heavy gas particles described in Section 2.1.

Every time, when a free electron ionises a heavy gas particle, the number of free electrons is increased by one, because a new free electron is released by the process. Since several ionisations take place in succession, more and more electrons are released. This sequence of ionisations, which starts with one seed electron, is often compared with an avalanche because of the exponential increase of free electrons. The electron avalanche starts near the cathode and travels towards the anode. It is stopped when it reaches the anode. Figure 3 illustrates the development of an electron avalanche in a uniform electrical field.

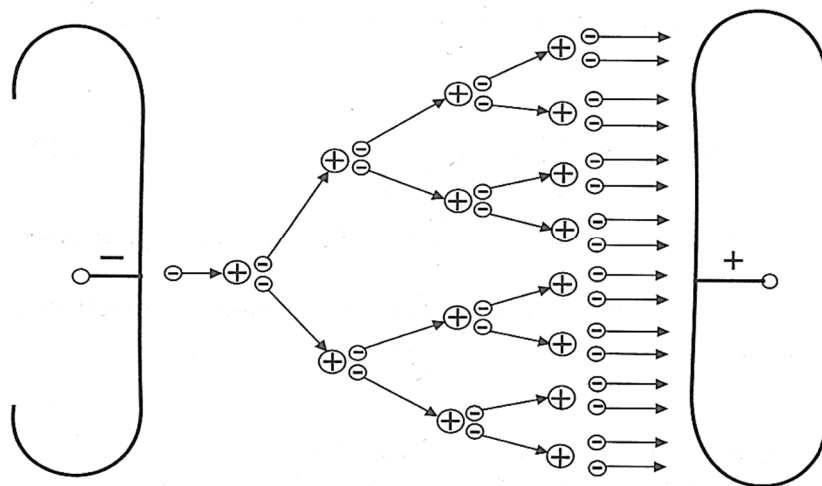


Figure 3: Development of an electron avalanche in an uniform electrical field [10]

In order to be able to cause ionisation by collision with a heavy particle, the free electron must have gained an amount of kinetic energy, which is at least equal to the ionisation energy of the heavy particle. The amount of energy received by the electrical field depends mainly on the electrical field strength, the pressure and the kind of used gas. The size and the atomic or molecular nature of the heavy particles, as well the pressure, influence the mean free pathway. If the energy is not sufficient for ionisation, the electron will excite or heat the

collision partner. The probability that an electron will cause an ionisation event is described by the Townsend first ionisation coefficient,  $\alpha$ . This value indicates the mean number of ionisations made by a single electron per metre travelled through the gap between the two electrodes for a given uniform electrical field.

Another process to create new free electrons is their release from the cathode through the collision of excited particles, positive ions or photons with the cathode. This effect is important to preserve the discharge, especially for gap distances smaller than one centimetre and discharges at higher pressures. The Townsend secondary ionization coefficient,  $\gamma$ , is defined as the average number of electrons produced at the cathode per electron generated by the primary ionisation process. The secondary Townsend coefficient depends on the electrical field strength, the gas pressure and the cathode or the dielectric material, which may be covering the cathode.

The Townsend criterion for breakdown is given by Equation 2 and is valid for electropositive gases, which produce cations instead of anions during the electrical breakdown. The Townsend criterion implies that every seed electron must be able to produce at least another electron by a primary or secondary ionisation process on its way through the gap between the electrodes with the distance,  $d$ , in order that the discharge is maintained [5, 7, 10].

$$\beta(e^{\alpha d} - 1) = 1 \quad (2)$$

### 2.3 Breakdown voltage and Paschen's Law

Paschen's Law was defined by Friedrich Paschen in 1889 and is described by Equation 3. In contrast to the Townsend criterion, where the sustainability of the plasma is determined by the reproduction of free electrons, Paschen's Law defines the breakdown voltage,  $V_b$ . The breakdown voltage is a function of the gas pressure,  $p$ , and the size of the gas gap,  $d$ . Paschen's Law is valid for uniform electrical fields. The coefficients A and B are constants and depend on the gas, which fills the gap between the two electrodes [11].

$$V_b = \frac{A \cdot (pd)}{\ln(pd) + B} \quad (3)$$

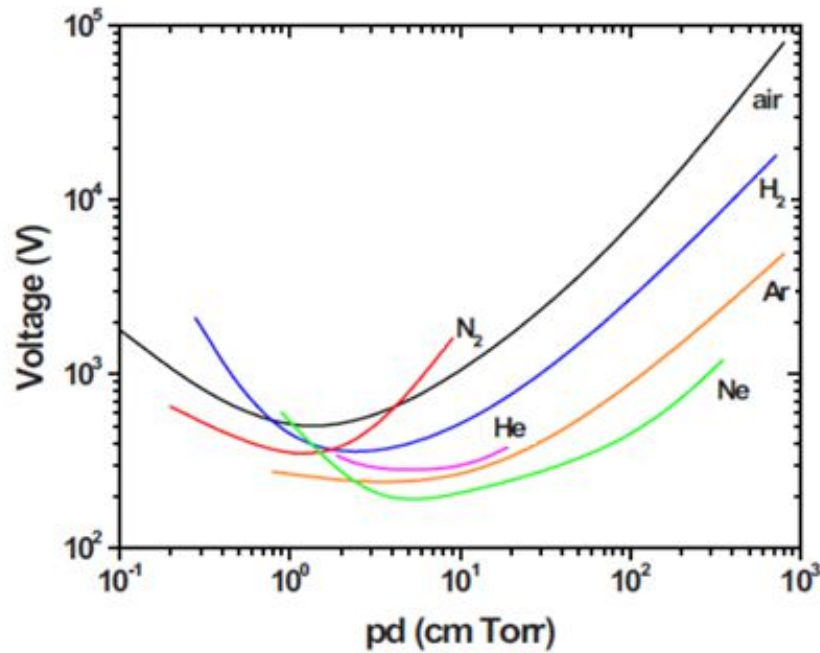


Figure 4: Breakdown voltage of different gases as a function of the pressure ,  $p$ , and electrode distance,  $d$ , in a parallel plate configuration [11]

Figure 4 illustrates the breakdown voltages for different gases for variant products of pressure and electrode distance. Every gas has a unique voltage versus the product of pressure and distance function and a minimum breakdown voltage. On the right side of this minimum, the increase of the product of pressure and electrode distance leads to higher breakdown voltages. The reason is shown by Equation 1. With increased pressure or distance, the average kinetic energy of the free electrons becomes lower, because a higher pressure reduces the mean free pathway for the electrons and a larger distance between the electrodes decreases the strength of the electrical field. The last correlation is described by Equation 4. In both cases the kinetic energy of the free electrons is reduced and with this their probability to cause an ionisation event. The only way to compensate for this is to increase of the applied voltage in order to balance the higher breakdown voltage.

$$E_0 = \frac{V}{d} \quad (4)$$

On the left side of the minimum, the breakdown voltage increases with the reduction of the product of pressure and electrode distance, which increases on the one side the kinetic energy of the free electrons by a higher electrical field (reduction of the electrode distance), or by the increase of the mean free pathway (reduction of the pressure). But on the other hand the probability that an electron collides with a heavy gas particle is lowered. The pressure determines the concentration of the heavy particles and the distance limits the volume where ionisations are possible. A reduction of both values leads to lower collision rates between electrons and heavy gas particles. To sustain the plasma with a lower collision rate, it is necessary that more collisions produce ionisation events. This is only possible if more electrons receive the necessary ionisation energy through the electrical field, which can be achieved by increasing the applied voltage

The minimum breakdown voltage of the Paschen curve is the point, where the ratio of average free electron kinetic energy gained and the collision rate between free electrons and heavy particles reach an optimum. The minimum breakdown voltages are placed in the range of  $10^0$  and  $10^1$  cmTorr in Figure 4. The breakdown voltages at atmospheric pressure (760 Torr) grow relatively fast with increase of the gap distance between the electrodes. Therefore, the gap must be kept small (millimetre range) under these conditions to prevent an unfavourable enlargement of the breakdown voltage. Besides pressure and gap distance, also the type of gas filling the gap has a strong influence on the breakdown voltage. The atomic radius and the atomic or molecular character of the gas and the gas pressure influence the mean free pathway of the free electrons. The ionisation energy of the gas particles defines the kinetic energy, which must be reached by the free electrons to cause ionisation. In Figure 4, it is shown, that the Paschen curves of the atomic gases neon, argon and helium are all placed lower than the molecular gases hydrogen, air and nitrogen, even though the ionisation energy of the noble gases are higher in comparison to the molecular gases.

If the applied voltage exceeds the breakdown voltage, the plasma is ignited. Further increase of the voltage leads then to the establishment of different discharge regimes. The properties and abilities of these discharge regimes are discussed in the next chapter.

## 2.4 Discharge regimes at low pressure

If DC voltage is applied to two parallel plate electrodes, which are separated through a gas gap, different discharge regimes can be established in the gas depending on the amplitude of

the applied voltage. A typical current-voltage diagram for low pressure discharges is demonstrated in Figure 5, where the different discharge regimes are marked by the points A to K.

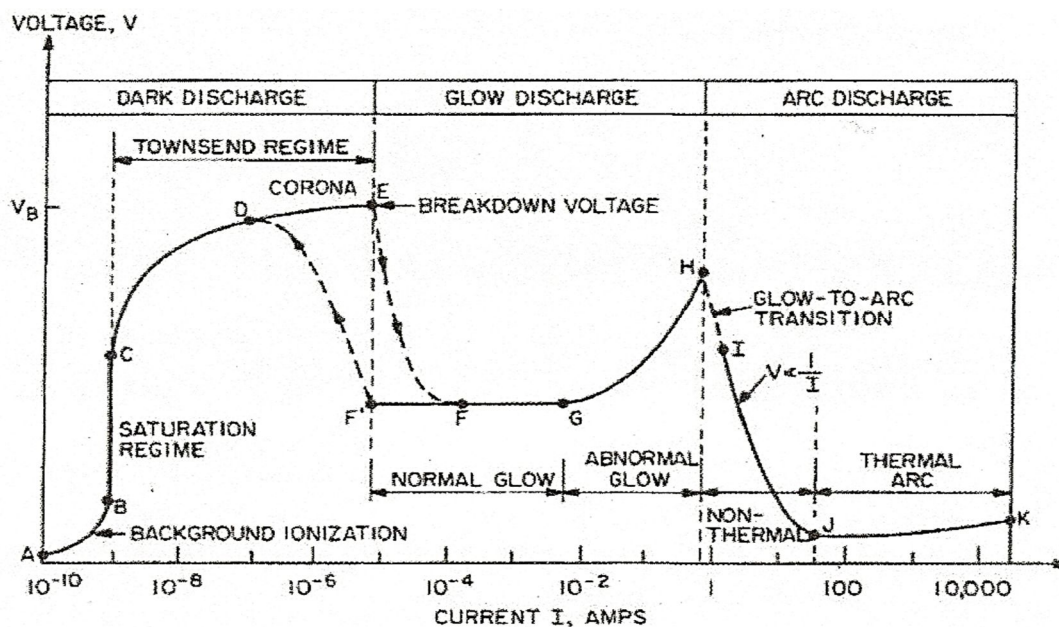


Figure 5: Characteristic current-voltage diagram for low pressure DC discharges [12]

As already described in the Section 2.1 and 2.2, free charge carriers are created by ionisation processes in every gas. If the established electrical field affects the gas, the free electrons of the gas are accelerated towards the anode. Therefore, a low current can be measured at low applied voltages. The current increases when the voltage is increased until all electrons, which are created by background ionisation, are gathered by the electrical field. This behaviour is shown in section A-B in Figure 5. In section B-C, the current is constant, because the kinetic energy gained by the free electrons is still not high enough for ionisation processes and thus the amount of electrons stays constant. In the Townsend regime (section C-E), the electrons are able to ionise heavy gas particles by inelastic collisions and create additional free electrons. Thereby, electron avalanches are established and the current rises exponentially with increased voltage. If the electrodes have sharp edges or peaks, corona discharges can occur in the area of D-E, because the locally increased field concentration exceeds the breakdown field strength of the gas. All discharges in the section A-E are invisible for the human eye and are therefore called dark discharges.

At point E the breakdown voltage is reached and an electrical breakdown occurs. The electron avalanches create such a huge amount of electrons that the potential difference between the electrodes collapses and the current is increased over several magnitudes without increasing the voltage. In the region of the normal glow discharge (section F-G) the plasma spreads over the area of the electrodes and becomes visible due to the creation of sufficient excited states. At the point G the whole area of the electrodes is covered and the current can only be raised further by relatively strong increases of the voltage. The discharge in this area (G-H) is called an abnormal glow.

In section H-I the glow discharge changes to an arc discharge. The highly heated cathode releases additional electrons by thermionic emission, thus a lot more collisions between free electrons and heavy particles are possible, which leads to an increase of the plasma temperature. Because of the high amount of free charge carriers in the gap between the electrodes, the electric resistance of the plasma is reduced dramatically and the free electrons reach the anode more easily. Therefore, a strongly reduced voltage is enough to preserve the discharge. From the points I to G, the temperature of the arc plasma rises, but the temperature of the free electrons and the heavy particles still differ from themselves. The thermal equilibrium is finally reached at point J.

The main differences between the glow and the arc discharge are the homogeneity of the plasma, the plasma temperature and the mechanism of how electrons are mainly emitted from the cathode. The glow discharge creates homogenous plasma and is therefore used for the uniform deposition of thin films in magnetron sputtering technology. In contrast, the arc discharge is strongly spatially limited and does not cover the whole electrode surface, which means, that the plasma is inhomogeneous. Furthermore, electrons are emitted from the cathode by thermionic emission at the arc discharge, whereas at the glow discharge electrons are emitted by collisions of excited particles or ions with the cathode.

If the same parallel electrodes configuration is used at atmospheric pressure instead of low pressure, the discharge behaviour would be the same from point A till to point E. However, the plasma does then not turn into a glow discharge, but changes into an arc discharge with only a small rise of the voltage. As a result of the higher ionisation rate at atmospheric pressure, conductive channels of free charge carriers are created between the electrodes. The electrons can now travel directly from the anode to the cathode with almost no electric resistance, which leads to a massive increase of the current. One channel takes over finally the

transport of the electrons, while the others disappear. The remaining channel is the plasma arc [10, 13, 14].

Creation of an arc plasma at atmospheric pressure is avoided by significantly reducing the amount of electrons being transferred between the two electrodes. The simplest way to do this is the increase of the electric resistance by the integration of a dielectric material between the two electrodes. This technology is called dielectric barrier discharge (DBD) and will be introduced in Chapter 4. The following chapter introduces the polypropylene packaging foil, which is treated by the nitrogen plasma.

### 3 Polypropylene

This chapter presents the multilayer polypropylene packing foil which is treated in this project by the nitrogen plasma. The different properties of the polypropylene foil and the orientation technologies to enhance these properties are explained. Furthermore, information about the different fields of application of polypropylene packaging foils is given.

#### 3.1 Chemical structure and properties

Polypropylene (PP) is a versatile semi-crystalline thermoplastic material, which can be used in many commercial applications. Its moderate production costs and its favourable properties make it the second most produced plastic in the world by weight. It is only exceeded by polyethylene [5]. PP is produced by the polymerisation of propylene.

The key properties of PP are its high heat and chemical resistance, a high strength-to-weight ratio, a very good clarity and great environmental stress cracking resistance. It can be processed through injection moulding, blow moulding, extrusion and thermoforming. The most important drawbacks of PP are a poor UV-light stability and low surface energy, which is typical of all polyolefins.

Polymers chains are generally made up of small identical chemical repeat units. The nature of these units, together with their configuration within the polymer molecule, partially defines the properties of the polymer. Other important characteristics are the molecular weight distribution and the degree of crystallinity. In the case of polypropylene the repeating unit is 1-methylethylene. Because the chemical structure of 1-methylethylene contains a chiral carbon atom, different positions of the methyl group cause stereoisomerism, which makes PP to an optically active macromolecule. Figure 6 shows PP with its repeating unit 1-methylethylene.

In principle, three different stereochemical forms of PP are possible: isotactic, syndiotactic and atactic. The isotactic configuration has all substituents on the same side, i.e. all the asymmetric carbon atoms are of the same formal (R or S). In contrast, the substituents of a syndiotactic polymer have alternating positions. In the atactic configuration, the substituents are randomly distributed. The three different configurations of PP are shown in Figure 7.

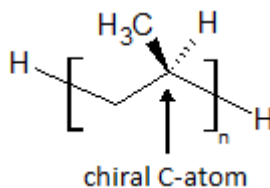


Figure 6: Polypropylene with 1-methylethylene as repeating unit

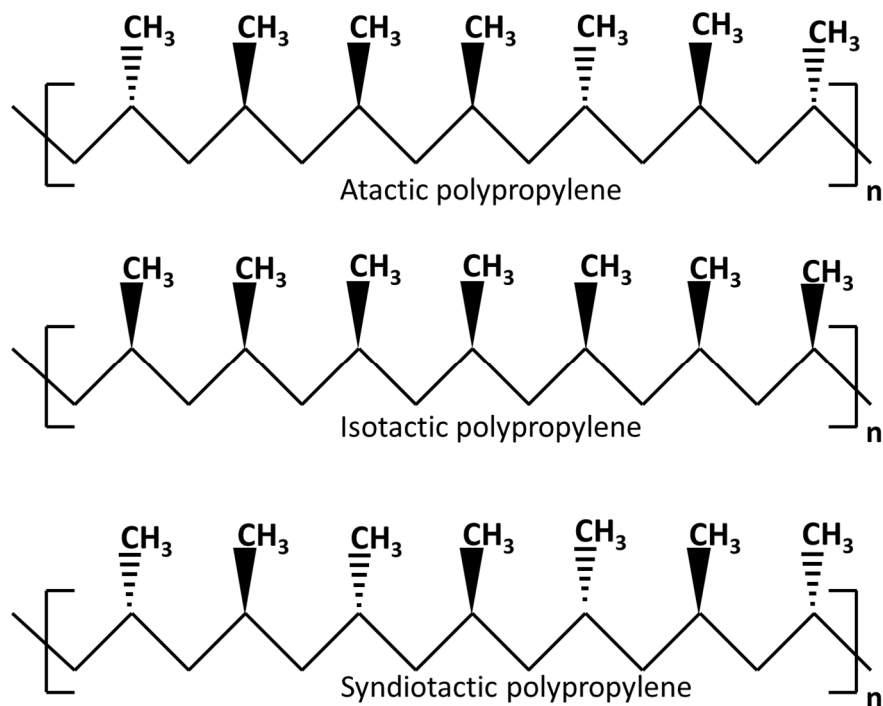


Figure 7: Atactic, isotactic and syndiotactic configuration of polypropylene

The syndiotactic and especially the atactic PP have a less ordered structure, which reduces the crystallinity, melting point, density and stiffness. The atactic form is amorphous and the syndiotactic form is semi-crystalline. The isotactic is thus the main PP configuration produced for commercial use. However, an increase of the amount of atactic PP in a mainly isotactic formulation increases the stretchability of the polymer. The individual structure of PP depends on the type of catalyst used in the polymerisation process. Typical isotactic PP's range from 40 to 70% crystallinity [15].

Isotactic polypropylene crystallises in three different modifications: the monoclinic  $\alpha$ -structure, the hexagonal  $\beta$ -structure, the orthorhombic  $\gamma$ -structure. In all of the crystal structures the chain is packed in the lattice as a left (L) or right handed (R) helix structure. The  $\alpha$ -

structure is the most thermodynamically stable structure. The helices align to form crystallites which then associate to form sheet-like lamellae. Secondary lamellae perpendicularly grow off the primary lamellae and are thus connecting the primary lamellae. This cross-hatched microstructure forms spherulites.  $\beta$  crystallinity is observed when the PP is cooled below its melting point. The polymer chains do not have the time to form the thermodynamically stable  $\alpha$  crystallinity. PP with  $\beta$ -structure has a lower density and lower melting point than PP with  $\alpha$ -structure. The  $\beta$ -phase is metastable relative to the  $\alpha$ -phase. Isotactic PP can also exist in  $\gamma$ -crystallinity. However, this form rarely arises from processing conditions. The  $\gamma$ -crystallites also form a cross-hatched structure like the  $\alpha$ -phase. The crystallites grow in two directions at the same time, resulting in a highly crystalline, high density material [16] [17].

Cast PP (not orientated) films are not normally chosen for flexible packaging, because their properties do not meet the necessary requirements. To improve the characteristics, the used films are stretched in one or in both directions. The resulting products are referred to as uniaxially orientated PP and biaxially orientated PP (BOPP), respectively.

### **3.2 Uniaxial orientated polypropylene and biaxially orientated polypropylene**

The market for flexible packaging requires polymer films that fulfil protective functions, product design, as well as economic and environmental aspects. Product protection is attained by providing high barriers against water vapour and oxygen permeation through the packaging. Besides this, high quality seals are also required. Good product appearance requires high-gloss transparent packaging films with excellent printability. Low production costs are achieved by good material utilisation and high-speed packaging lines. Recyclability and a maximum packaging effect at minimum material use guarantee that the environmental aspects are satisfied.

To ensure that PP films reach these requirements they are stretched during production in one or both directions. This leads to orientation of the previously partially random polymer chains. The orientated PP has significantly increased mechanical, optical and barrier properties, in contrast to non-orientated PP. Figure 8 shows the enhanced characteristics of BOPP in comparison to cast PP.

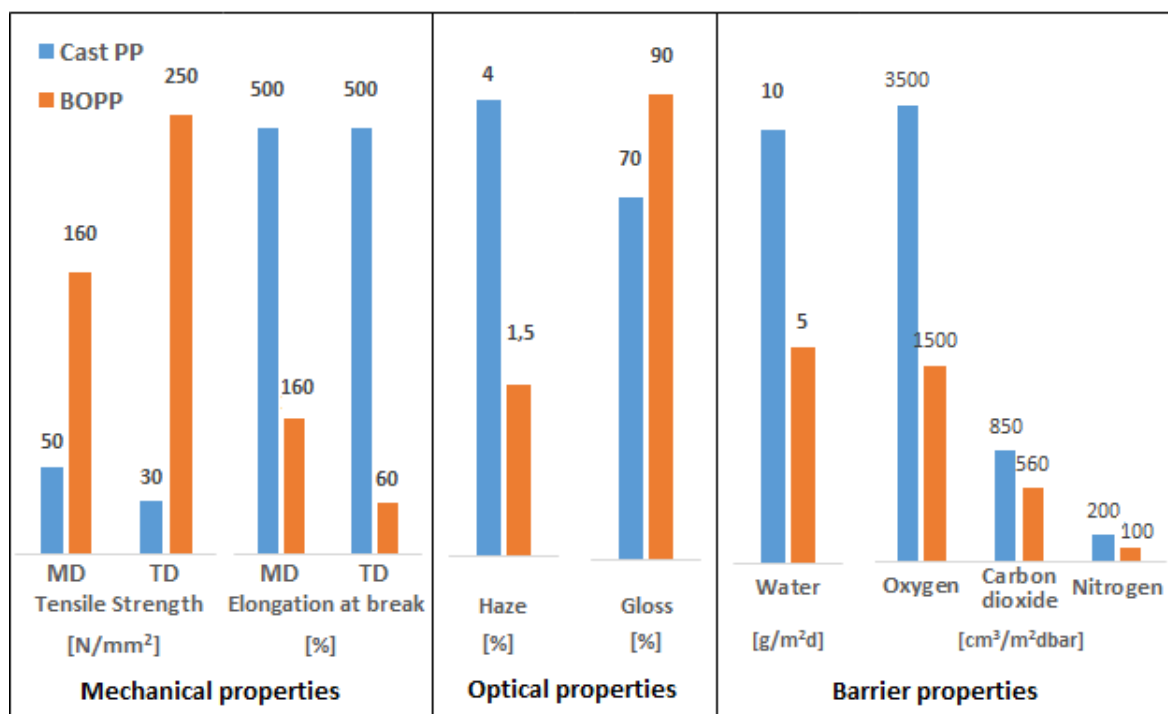


Figure 8: Mechanical, optical and barrier properties of BOPP and cast PP films with a thickness of 25  $\mu\text{m}$  in each case in machine direction (MD) and transverse direction (TD) according to [18]

The existing orientation technologies are distinguished in the orientation draw direction and the related stretching process. The films can be stretched longitudinally ('machine direction') and crosswise ('transverse direction'), in only one direction or both. The stretching in two dimensions can be performed sequentially or simultaneously.

The machine direction orienter uses two rollers with different speeds to stretch the film longitudinally. In contrast, the transverse direction orienter elongates the polymer in the cross direction by heating the film and stretching it on a tenter frame. The product of these two technologies is uniaxially orientated PP. It is also possible to combine the two stretching technologies, which results in sequential stretching in both directions. This product is BOPP. The 'double bubble process' is another stretching technology used to produce BOPP simultaneously. Initially, a circular tube is extruded. Through heat and injection of pressurised air, the tube inflates to a bubble, which causes the biaxial stretching. Depending on the process method different polymer films with different characteristics are manufactured. They are used for different products, which are shown in Table 1.

Table 1: The different stretching technologies, their equipment and products

Stretching process	Equipment	Typical products
Machine direction stretching (uniaxial orientation)	Machine direction orienter	Tear stripes, tapes, breathable films
Transverse direction stretching (uniaxial orientation)	Tenter frame	Shrink sleeves
Sequential stretching (biaxial orientation)	Machine direction orienter and tenter frame	Packaging films, tapes, labels, industrial films
Simultaneous stretching (biaxial orientation)	Double bubble	Packaging films, shrink films

Besides PP, the stretching technologies are also utilised for the orientation of polyethylene terephthalate, polystyrene, polyvinyl chloride and polyamide. However, BOPP has by far the biggest share of the orientated film market (66%). Over six million tons of BOPP are produced every year [18].

The main field of application is packaging, where BOPP is used as plain film and multilayer film with heat sealable properties. The skin layers of the multilayer structures consist of coextruded PP copolymer, which have a lower melting point than the BOPP core layers. Thus, it is possible to seal the packaging foil at temperatures, which are not deforming or damaging to the interior layers. The simplest multilayer structure is a three-layer film with two outer heat sealable skin layers and one core layer. Besides this, five-layer and seven-layer films exist. Their benefits in comparison to the three-layer film are improved characteristics, such as better optical or barrier properties, and cost advantages. Expensive additives are admixed in thinner intermediate layers, which reduces the necessary quantity and thus the production costs. Table 2 lists the different kinds of BOPP films and their typical thicknesses and applications.

BOPP films are also used in converting processes, such as vacuum coating, metallisation and lamination to add additional layers composed of e.g. aluminium, silicon oxide, alumin-

ium oxide, polyvinylidene chloride, polyvinyl alcohol and ethylene vinyl alcohol copolymers. In this case, the aim is the enhancement of the barrier properties and, as appropriate, the protection against sun light. To ensure that the coated or laminated layers do not disengage or deadhere from the substrate, the surface energy of the PP must be close to that of the coating layer. Polyvinylidene chloride, polyvinyl alcohol and ethylene vinyl alcohol are polar polymers. Aluminium and the ceramics silicon oxide and aluminium oxide all have high surface energies. BOPP has a low surface energy of about 30 mN/m. In order to maximise the adhesion between the BOPP and the coating or the laminated layer, the surface energy of the BOPP must be increased to a minimum of 42 mN/m. The surface energy of the BOPP is also important for the wettability by printing inks. To achieve good printability, the BOPP needs a surface energy of at least 37 mN/m [19]. During this project, an atmospheric pressure plasma treatment method was investigated as a means of increasing the surface energy of BOPP.

The BOPP film utilised for this project has a three-layer structure with two polyolefin heat sealable skin layers and a clear BOPP core layer. The heat sealable skin layers are made of a propylene-ethylene copolymer and have a thickness with up to 3  $\mu\text{m}$ . The glass transition temperature of the skin layers is reduced relative to the BOPP core layer by the addition of the ethylene to the propylene in the copolymer. This ensures that the melting point of the heat sealable skin layers is lower than the melting point of the core layer, which allows to heat seal the BOPP film at temperatures, which do not affect the core layer. One of the skin layers is corona treated, the other one is untreated (Figure 9). The untreated side was plasma treated with the DBD and investigated. The thickness of the whole film was 50  $\mu\text{m}$ . The next chapter will explain the physical fundamentals and the properties of the plasmas utilised.

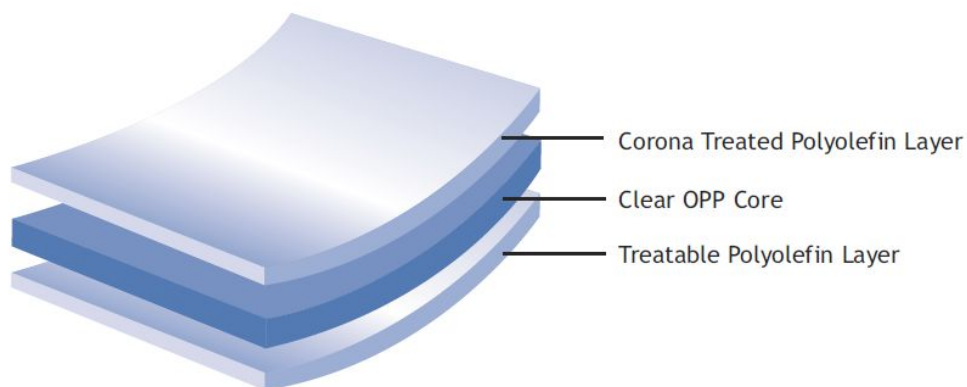


Figure 9: The three-layer structure BOPP film investigated in this project

Table 2: The various applications of BOPP as plain film and multilayer structure with the used range of thickness

Industrial tapes	Laminated metallised	Electrical proposes	General purposes	General Purpose	Opaque and white	Packaging purposes
30-40 µm	10-50 µm	3-20 µm	15-50 µm	12-40 µm	30-40 µm	30-80 µm
Pressure sensitive tapes	Brochures catalogues	Cable insulation	Flower over-wrappings	Textiles (shirt packaging)	Food packaging (light sensitive)	Food packaging (bakeries, cheese, noodles...)
Box sealing tapes	Print lamination	Capacitors	Stationary goods (photo albums, envelopes...)	Metallising (crisps, snacks)	Hygiene articles	
Masking tapes	Carton boxes		Release films	Cigarette over-wrappings	Labels	Cosmetics
	Cosmetic boxes			Shrinkable films		
	Food packaging			Twist films (sweets)		
<b>Plain film</b>				<b>3-Layer heat sealable film</b>		<b>5-7 Layer heat sealable film</b>

## 4 The dielectric barrier discharge

The DBD creates highly non-equilibrium cold plasmas at atmospheric pressure. This technology offers the advantages of low temperature plasmas, including homogeneity and low temperature, without the restriction of vacuum conditions. Thus, the DBD is most suitable for the surface treatment of heat sensitive polymers and can be established easily in industrial production. The possible DBD configurations, their applications and the different discharge regimes are discussed in this chapter.

### 4.1 Surface and volume discharge configurations of dielectric barrier discharges

DBD systems consist of two electrodes, which are separated by a gas gap of a few millimetres. At least one of the two electrodes is covered by a dielectric material. The arrangement of the two electrodes is coaxial cylindrical or parallel. A high AC voltage supplies the electrodes and creates the electrical field, whereas the dielectric dramatically reduces the current during the discharge and thus inhibits the development of an arc discharge. As a result of the high voltage, only dielectrics with high electrical strength are suitable. The most common materials are ceramics, glass and specific polymers such as silicones.

The gas breakdown starts like the Townsend breakdown with the creation of electron avalanches through the acceleration of seed electrons by the electrical field. The electron avalanches grow from the anode to the cathode. When the electrons reach the dielectric, they cannot pass through it and accumulate on the dielectric surface. The only way to remove them, is changing the polarisation of the electrical field. When the polarisation has changed, the accumulated electrons act as seed electrons and new electron avalanches can grow now in the opposite direction. The change of the polarisation necessitates the use of AC instead of DC. The typical frequencies applied range between 1 kHz to 100 kHz.

The DBD is used in many applications, such as exhaust gas purification [20, 21], ozone production [22-24], excimer ultraviolet lamps [25], medical sterilisation [26, 27], plasma display panels [28], plasma actuators as flow controllers [29, 30], water purification [31-34] and coating with precursors by plasma deposition systems (physical enhanced chemical vapour deposition) [35-44]. DBD is furthermore used to modify polyolefin surfaces in order to

promote wettability, printability, coatability and adhesion. This is of particular interest to the field of packaging in the field of packaging.

The different configurations are distributed in surface DBDs and volume DBDs. Surface DBDs have in contrast to the volume DBDs no gas gap, because it is replaced by a dielectric. Therefore the discharge occurs in the space between the two electrodes on the surface of the dielectric. Figure 10 shows different DBD configurations for surface and volume discharges.

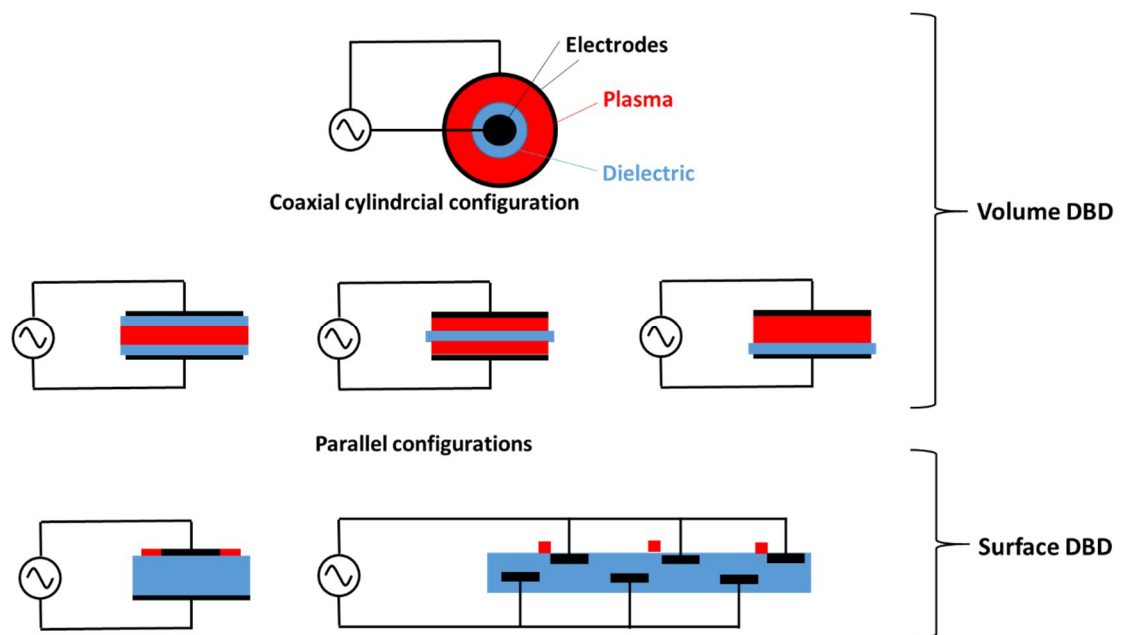


Figure 10: Different dielectric barrier discharge configurations for surface and volume discharges according to [14, 45]

For the treatment of polyolefin foils in the packaging industry the parallel volume DBD is mainly applied. However, the industrial machines vary from the configurations shown in Figure 10. In industry, the upper electrode is a roller or drum, which transports the packing foil through the plasma. A flexible dielectric is placed on the roller and the polymer film lies on the dielectric. There is no gas gap between the dielectric and the film to ensure, that the plasma is not established on the backside of the film, which would lead to the treatment of both polymer surfaces. The lower electrode has a curved shape to match the drum in order that the two electrodes are coaxial and parallel to each other. In addition, the lower electrode is corrugated perpendicular to the machine direction. As a consequence the plasma is only ignited, where the distance between the two electrodes is minimal and is thus highly concentrated on the top of the corrugated electrode. The width and the diameter of the roller are typically in the order of a few metres. The speed of the film during the treatment ranges up

to a few hundred meters per minute. The necessary power to sustain the discharge reaches tens of kilowatts. A typical arrangement of an industrial DBD system for polymer film treatment is illustrated in Figure 11.

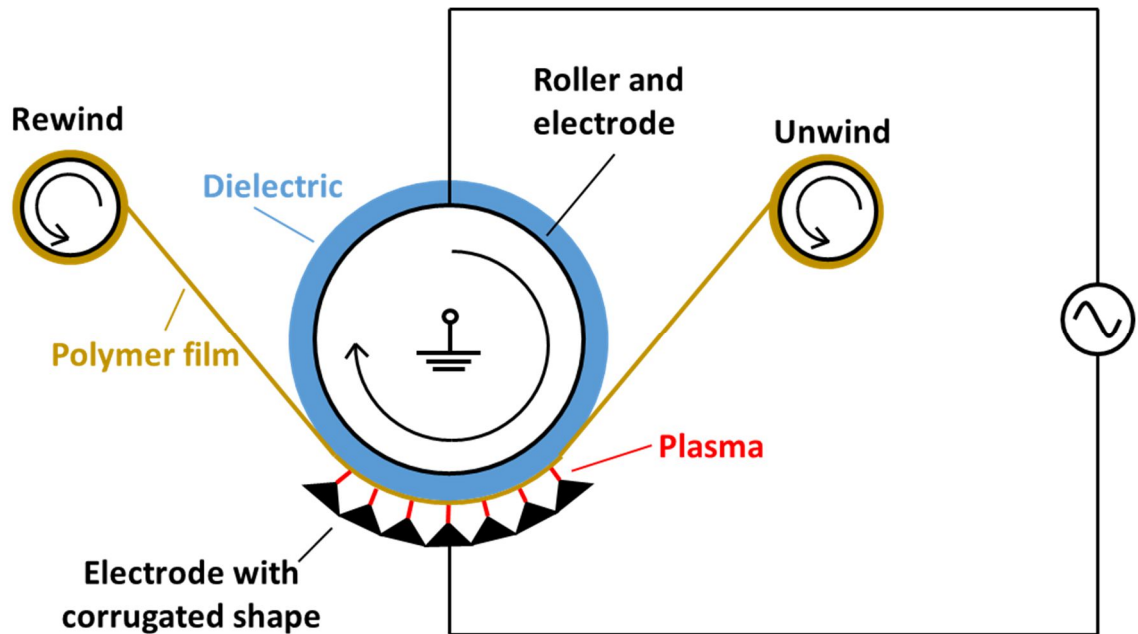


Figure 11: Industrial DBD configuration for the surface treatment of polymer foils

The configuration, shown in Figure 11, is often misunderstood. The corrugated shape of the lower electrode and the name ‘corona treatment’ implies that the discharge would be a corona discharge and not a DBD [46]. Corona discharges are established when the electrical field is significantly enhanced at sharp edges or thin wires. This is also the case in the configuration in Figure 11 through the use of the electrode with the corrugated shape. However, the corona discharge occurs locally around the sharp edge or thin wire and does not extend to the counter electrode. The discharge of the configuration, illustrated in Figure 11, crosses the whole gas gap and reaches the dielectric of the roller electrode and can be thus easily identified as DBD. The term ‘corona treatment’ means a surface treatment with DBD in air and is not correlated with the corona discharge [47].

## 4.2 Dielectric Barrier Discharge regimes

DBDs at atmospheric pressure are classified into the inhomogeneous filamentary discharge and homogeneous or diffuse forms. The type of discharge is dependent on the operating parameters such as amplitude, frequency and waveform of the voltage applied, the capacitance and surface properties of the dielectric material and of the uncovered electrode, the gap distance between the electrodes and the composition of the gas in the gap. The discharge regimes are established through different breakdown mechanisms. While the mechanism, which lead to homogeneous discharges, match with the mechanism at low pressure created by applied DC voltages, discussed in Chapter 2, the filamentary mode is a new sort of non-thermal plasma.

### 4.2.1 The filamentary discharge

The filamentary discharge is the most often used plasma form for industrial surface treatment of polymer foils at atmospheric pressure. The ignition of this discharge does not need special requirements and is thus easily established. If the applied AC voltage exceeds the breakdown voltage, the discharge occurs in the form of several thin single filaments, also called micro-discharges or streamers, in the gas gap between the two electrodes. The filaments are spatially and temporally separated from each other. The filamentary discharge is therefore classified as inhomogeneous. Figure 12 shows a single streamer and a multitude of streamers of the filamentary discharge in nitrogen at atmospheric pressure.

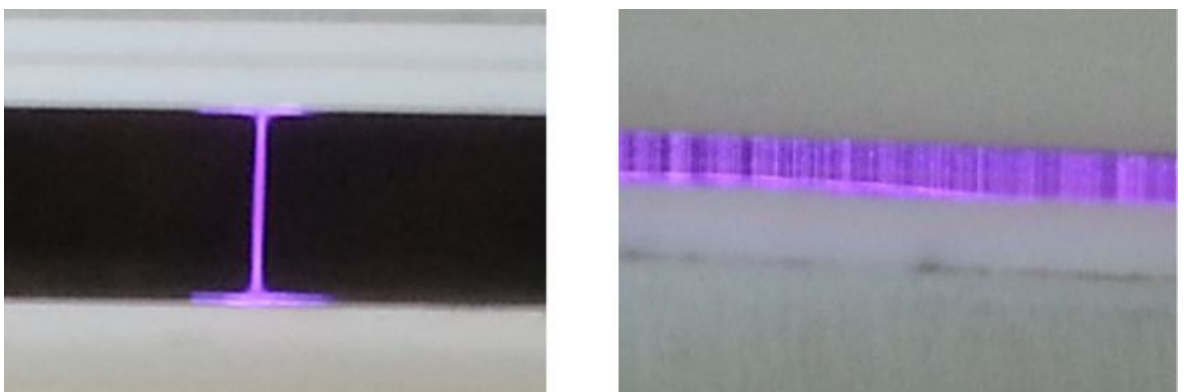


Figure 12: Single streamer (left picture) and a multitude of streamers (right picture) of the filamentary discharge in nitrogen at atmospheric pressure

The filaments occur every half cycle of the applied voltage and collapse after a short life time (ca. 100 ns). The amount of ignited filaments increases as the applied power increases.

They are randomly distributed in time and space between the two electrodes, however there is a memory effect due to the charge accumulation on the dielectrics. This memory effect leads to the reignition of the filaments always at the same positions, because the breakdown voltage is reduced due to the higher amount of seed electrons. These additional seed electrons are accumulated on the dielectric by the previous filament. This process entails a patterned formation of the filaments.

Kogelschatz [45] also discusses the aspect of accumulated electrons reducing the applied electrical field through their negative charge. As a result, the filaments ignite at positions where the filaments have not occurred during the previous half cycle, because the electrical field is stronger there. The frequency and the amplitude of the applied AC voltage are the crucial physical quantities that determine, which effect of the accumulated electrons is dominating and thus whether the filaments are patterned or not. If the DBD system is operated with high voltage and low frequency settings, the filaments are not reignited at the same positions. While low voltage and high frequencies lead to patterned formation of the filaments. Unfortunately, Kogelschatz does not give further information about exact values for the amplitude or frequency.

The form of a single filament is widely cylindrical with a radius of about  $100\ \mu\text{m}$  and spreads into a larger surface discharge at the surface of the dielectrics, as shown in Figure 13. The electron density within a filament amounts to  $10^{14}\ \text{cm}^{-3}$ . The current density can reach up to  $10^3\ \text{A cm}^{-2}$ . These values match with those of an atmospheric pressure glow discharge. Thus, and because of the non-equilibrium character of the microdischarges, these can be counted as locally limited transient high-pressure glow discharges [9, 46].

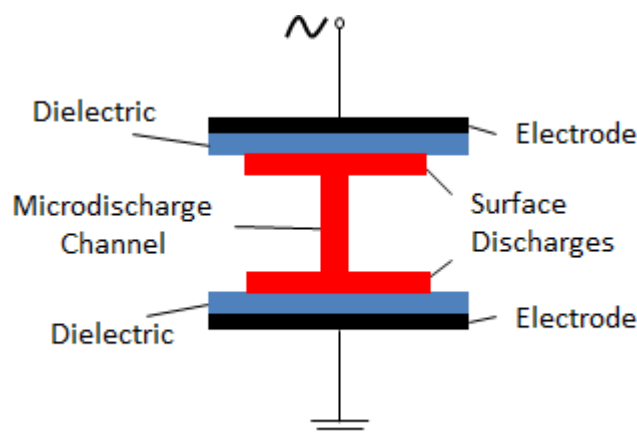


Figure 13: Single microdischarge channel of a filamentary discharge according to [46]

### 4.2.2 The space charge field of an electron avalanche

The Townsend mechanism implies the development of electron avalanches through the ionisation of heavy gas particles by free electrons. The electron avalanches move straight from the cathode to the anode. The free electrons of a single avalanche are spatially concentrated. Their quantity rises exponentially during movement towards the anode. The cations, which have been created during the ionisation processes, remain behind the free electrons. The space, where the free electrons are concentrated, is called the head of the avalanche. The stem is the region, where the cations are located. Due to the high concentration of free charge carriers in the stem and the head of an avalanche, the avalanche has a space charge field,  $E_a$ . The strength of the space charge field depends on the quantity of created free charge carriers. Figure 14 illustrates a single electron avalanche with the negative charged head, the positive charged stem and the resulting space charge field.

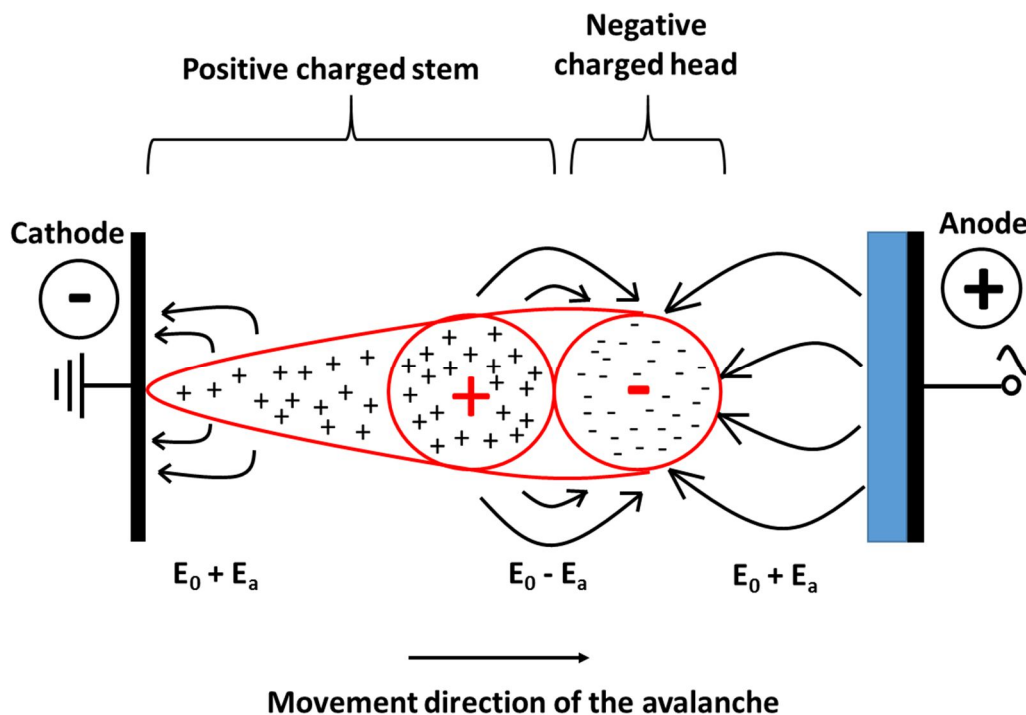


Figure 14: Space charge field of a single electron avalanche according to [10]

The space charge field interacts with the polarities of the electrodes and can thus distort the uniform electrical field. The intensities of the applied field is increased toward the head and the stem of the avalanche by the amount of the space charge field ( $E_0 + E_a$ ) and reduced in

the positive charged region just behind the head ( $E_0 - E_a$ ). Depending on the strength of the distortion two different discharge mechanisms are possible, these are the Townsend mechanism and the streamer mechanism.

#### 4.2.3 Discharge by Townsend or streamer mechanism

The Townsend mechanism starts with the development of several electron avalanches. The space charge fields of these avalanches are weak in comparison to the applied electrical field, thus the distortion of the applied field is negligible. The electrical field between the electrodes stays uniform and the avalanches move straight towards the anode. The result is the creation of a spatially homogenous plasma like the glow discharge, which covers the whole electrode surface. The discharge of the Townsend mechanism is shown in Figure 15.

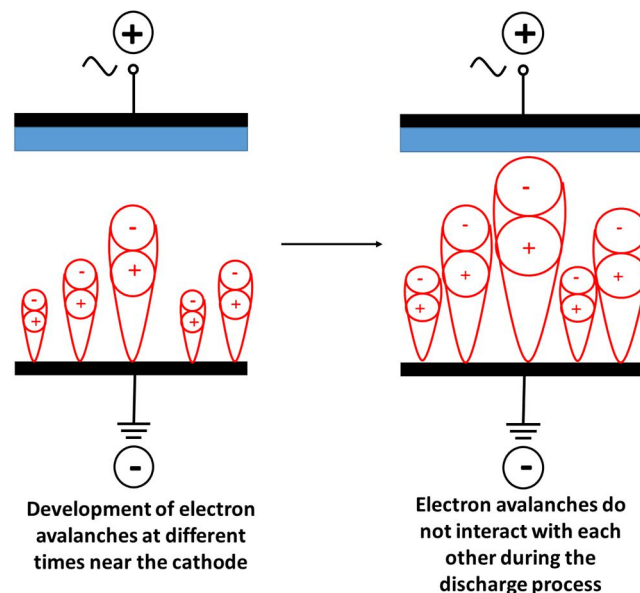


Figure 15: Development of the Townsend discharge according to [10]

The filamentary breakdown mechanism starts the same way as the Townsend discharge. However, Raether confirmed in 1939 that the necessary time for the development of a filament is shorter than would be expected from the Townsend mechanism [48]. Afterwards, Raether, Loeb and Meek developed the streamer mechanism [49, 50], which explains the filament formation with the space charge creation of the free charge carriers.

In contrast to the Townsend mechanism, the space charge field is not negligible in the streamer mechanism. The reason is, that the first electron avalanche creates a critical amount of free charge carriers and the space charge field of this avalanche distorts strongly the applied electrical field. As a result, the later starting avalanches are directed into the stem of

the first avalanche, because the field intensity of the stem is strongly increased through the space charge field of the cations. The electrons of the secondary avalanches and the cations of the first avalanche form a conductive channel between the two electrodes, which is visible as filament. The streamer mechanism is illustrated in Figure 16.

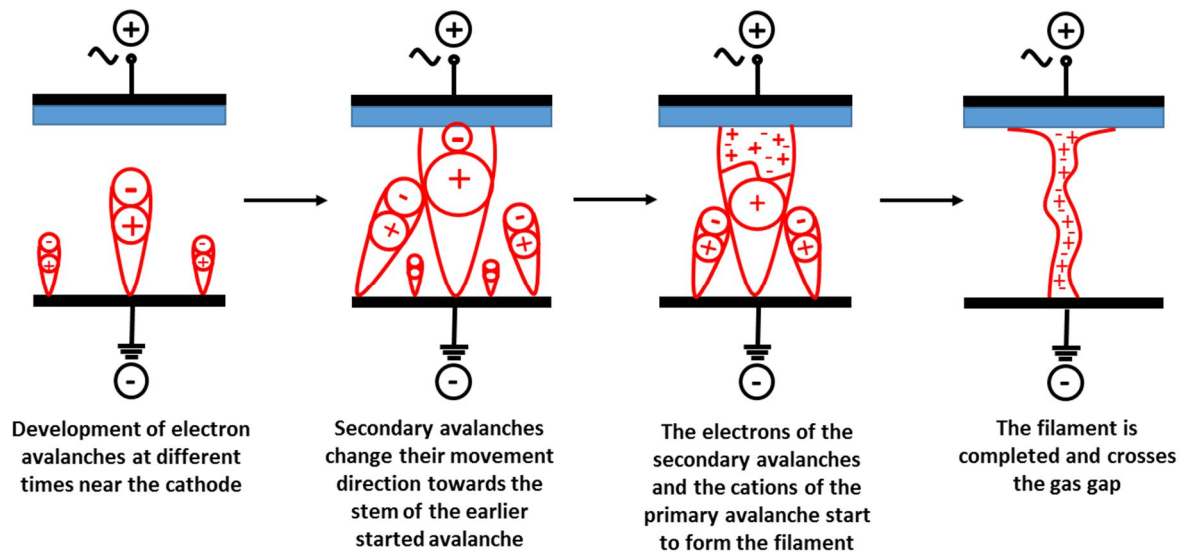


Figure 16: Development of the filamentary discharge in the manner of the streamer mechanism according to [10]

Whether or not, the discharge develops from the streamer or the Townsend mechanism, is heavily depends on the amount of free charge carriers created in a single avalanche. The Meek criterion defines this amount to  $10^8$  ionisations [10, 51]. If a single avalanche reaches this quantity of ionisations, the homogeneous applied electrical field gets distorted by the space charge field. Instead of a homogenous plasma, a multitude of filaments is ignited and the plasma is thus spatially limited. The faster development time of the streamer mechanism in comparison with the Townsend mechanism can also be explained with the space charge field, which significantly increases the electrical field at the head of the avalanche (Figure 14). As a consequence, the free electrons at the head receive more kinetic energy and the avalanche crosses the gas gap faster.

DBD plasmas ignited at atmospheric pressure are mostly filamentary, because the high concentration of heavy gas particles leads automatically in the most cases to a breakdown by the streamer mechanism. If the pressure is reduced to vacuum conditions, the discharge follows the Townsend mechanism and the plasma created is homogenous, provided that the applied voltage stays near the breakdown voltage. This is due to the low concentration of heavy gas particles making it almost impossible for the Meek criterion to be fulfilled.

Massines et al. [52] defines the transition from Townsend to streamer mechanism by the product of pressure and gas gap distance. If this product exceeds the value of 20 Torr·cm, the discharge follows the streamer mechanism. If this value is not reached, the plasma is ignited according to the Townsend mechanism. However, this definition is not valid for helium, neon, argon and nitrogen, because it is possible to ignite homogenous plasmas with these gases at atmospheric pressure.

Homogenous plasmas are favoured as a method for increasing the surface energy of polyolefin foils, as the modification is uniformly applied, resulting in a high quality film. Homogeneous plasmas can also be ignited at atmospheric pressure, however special conditions are required, so that the Meek criterion is not satisfied. These kinds of plasmas are known as atmospheric pressure glow discharges (APGD) and atmospheric pressure Townsend discharge (APTD).

#### **4.2.4 Atmospheric pressure glow and Townsend discharges**

The first researcher, who started to study homogeneous DBD discharges at atmospheric pressure was Okazaki et al. in 1988 [53, 54]. They were able to create uniform discharges in different gases such as helium and argon. They named the discharges obtained atmospheric pressure glow discharges and could show that highly specific conditions, such as electrode structure, frequency and amplitude of the power supply, gap distances and type of dielectric material, will lead to glow discharges in certain gases.

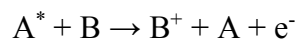
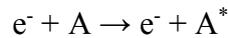
Massines et al. [40, 47, 55-57] further investigated the nature of homogeneous discharges in helium, neon, argon and nitrogen. They detected that the homogeneous discharge mechanism of helium, neon and argon is similar to the DC glow discharges at low pressure and has the same voltage and current characteristics. To be able to understand, why the Meek criterion is not fulfilled in these discharges at atmospheric pressure, it is necessary to discuss two specific properties of this group of gases: the ionisation energy and the molecular size. Helium, neon and argon are atomic noble gases, thus their ionisation energies are relatively high and they have comparable small atomic radii. Their small size leads to a higher mean free pathway for the free electrons, which results in lower breakdown voltages. The combination of low breakdown voltage and high ionisation energy dramatically limits the quantity

of ionisations within a single electron avalanche. Table 3 gives an overview of the breakdown voltage at atmospheric pressure, the mean free pathway for electrons and the first ionisation energy of gases, which are used for the DBD.

Table 3: Breakdown voltage, mean free pathway for electrons and first ionisation energy for different gases at atmospheric pressure according to [10]

	<b>Breakdown voltage</b> [kV/cm]	<b>Mean free pathway electrons</b> [ $\mu\text{m}$ ]	<b>Ionisation energy</b> [eV]
Helium	3.7	1.10	24.6
Neon	4.2	0.7	21.5
Argon	6.5	0.39	15.7
Air	32.0	0.37	-
Nitrogen	33.0	0.35	15.7

However, the high ionisation energy and the low breakdown voltage are not sufficient to explain the homogenous character of the plasmas ignited. The second important point is that the direct ionisation via inelastic collisions is in competition with Penning ionisation in these glow discharges. The Penning ionisation needs two steps to create additional free electrons. An electron excites a heavy gas particle, which then ionises another heavy gas particle:



The Penning ionisation is slower than the direct ionisation. As a result, when Penning ionisation and the direct ionisation are in competition with each other, the total amount of ionisations is reduced, because fewer electrons are created directly. The Meek criterion is thereby not satisfied and a glow discharge is established at atmospheric pressure. But this is only possible for the noble gases helium, neon and argon, which are relatively expensive and thus not suitable for industrial processes.

APGD in nitrogen at atmospheric pressure does not exist. However, creation of an atmospheric pressure Townsend discharge is possible. This kind of plasma has been intensely

studied in recent years [58-67]. The Townsend discharge in nitrogen is of great interest, because a homogeneous discharge is ignited in a relatively cheap gas, which makes this technology suitable for industrial applications. The Townsend discharge or dark discharge is a low current, self-sustained plasma with a comparatively low space charge and is thus also a homogeneous discharge. The Townsend discharge is ignited by a weak electrical field, with applied voltages being less than the breakdown voltage. Normally, plasmas cannot be ignited under such conditions, because the seed electrons are not able to sustain the discharge with enough ionisations. However, it is possible to increase the quantity of electrons via their emission at the cathode dielectric. Excited states collide with the dielectric and release additional free electrons from there. The electrons released have been attached to the dielectric by electron avalanches in the half cycle before and need relatively low energies to be set free. The released electrons are accelerated through the electrical field in the direction of the anode and can create further electrons via ionisation of heavy gas particles.

If the amount of emitted electrons is high enough, the plasma is ignited at voltages less than the breakdown voltage. This is also shown by the Townsend criterion for gas breakdown (Equation 2). When voltages less than the breakdown voltage are applied, the first Townsend coefficient,  $\alpha$ , is reduced and the augmentation of the electrons is lowered to a value less than one. The plasma is thus no longer self-sustaining. In order that, the augmentation of the electrons exceeds a value of one and the plasma is able to maintain itself, the second Townsend coefficient,  $\gamma$ , must compensate for the reduction of the first Townsend coefficient,  $\alpha$ . The secondary electron emission is the important factor to sustain the discharge. The Penning ionisation in the APTD is nevertheless as necessary as it is in the APGD to reduce the direct ionisations in the gas and keep the discharge homogeneous. Table 4 summarises the characteristics and conditions for the APGD and the APTD.

The APTD can be successfully ignited with experimental setups on the laboratory scale. However, APTD is also very unstable and can easily turn into the filamentary mode, which is problematic for industrial applications. Specific conditions are necessary to prevent the discharge becoming inhomogeneous. Both electrodes must be covered with a dielectric to maximise the emission of secondary electrons. The gas gap must be smaller than 1 mm in order that volume effects (direct ionisation) are kept small compared to the surface effects (secondary electron emission). The biggest problem however is that very high purity nitrogen gas must be used, because even very low impurities (other gases) quench the metastable species of the nitrogen plasma and thus cause the filamentary discharge. Brandenburg et al.

[67] showed for example that oxygen concentrations above 800 ppm are enough to change the APTD to the filamentary mode.

Table 4: Different characteristics and conditions for the Atmospheric Pressure Townsend Discharge and the Atmospheric Pressure Glow Discharge [56]

	<b>APTD</b>	<b>APGD</b>
Electron density maximum [ $\text{cm}^{-3}$ ]	$10^7 - 10^8$	$10^{10} - 10^{11}$
Ions density maximum [ $\text{cm}^{-3}$ ]	$10^{10}$	$10^{11}$
Metastable of the dilution gas	$10^{13}$	$10^{11}$
Current density [ $\text{mA}/\text{cm}^2$ ]	0.1 - 10	10 - 100
Gas voltage variation around the current maximum	Constant (Townsend plateau)	Decrease (cathode fall formation)
Dilution gases	$\text{N}_2$	Penning mixture in He, Ne, Ar
Typical frequency range [kHz]	< 10	> 1
Power for a 10 kHz excitation	Some $\text{W}/\text{cm}^3$	Some $0.1 \text{ W}/\text{cm}^3$

The filamentary and the homogeneous modes can often be readily distinguished with the human eye, because the homogeneous discharge forms are uniformly distributed over the electrode area, whereas the filamentary discharge consists of spatially divided filaments. However, it is possible, that the filaments overlap with each other with the result that the discharge looks homogeneous. Therefore, measurement of discharge current is a much more definitive method for identification of the type of discharge occurring. In the filamentary mode there are a multitude of current transients of nanosecond durations. In contrast, the Townsend and glow discharges show a single peak of microsecond duration with each voltage half cycle. Figure 17 illustrates the discharge current and the applied sinusoidal voltage of the filamentary and the Townsend discharge in nitrogen.

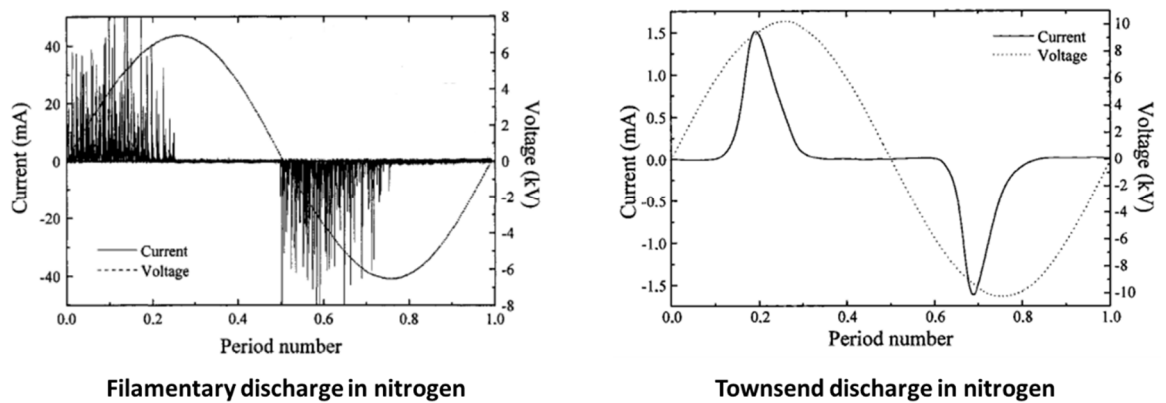


Figure 17: Discharge current of the filamentary and the Townsend discharge in nitrogen from [68]

The current peaks indicate ignition of the plasma. The plasma is extinguished, when the applied voltage drops under a certain threshold, which is necessary to sustain the discharge and is then reignited in the next half cycle.

Another method for ignition of glow discharge plasmas at atmospheric pressure involves the use of the nanosecond repetitive pulsed technology. This technology uses short unipolar or bipolar high voltage pulses with a duration of 10-100 ns [40, 51]. The repetition frequency reaches the kHz range. As a result of the short pulse duration, the discharge stays uniform, because the electron avalanches do not have the necessary time to attain the critical level of ionisations, which avoids the transition to the filamentary discharge. This technology offers the possibility to ignite stable glow discharges in gases such as air [69-83] and nitrogen [72, 80, 84]. However, this technology is currently too expensive for industrial applications, where sinusoidal AC power supplies are still widely used.

### 4.3 Interactions of the DBD nitrogen plasma with the polymer surface

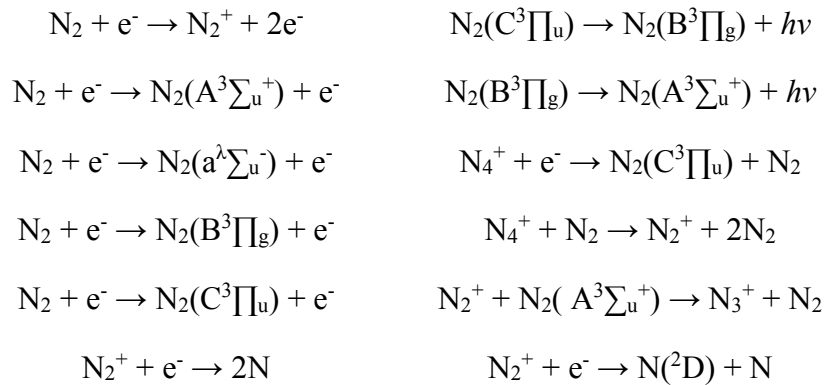
Before the interactions of the excited molecules with the polymer surface are discussed, a general review about possible electron-molecule collision processes within a nitrogen DBD plasma is given. The electron-molecule collision processes are categorised into elastic and inelastic collisions. The elastic collisions transfer thermal energy from the electrons to the molecules. The inelastic collision create the reactive species of the plasma, the ions, the

excited species and radicals. The inelastic electron-molecule collisions processes can be further classified into excitation and ionisation reactions. The diverse collision processes between electrons and gas molecules are summarised in Table 5.

Table 5: Electron-molecule collision processes [51]

Collision process	Process
Elastic	$e^- + AB \rightarrow e^- + AB$
Excitation	$e^- + AB \rightarrow e^- + AB^*$
Ionisation	$e^- + AB \rightarrow 2e^- + AB^+$
Attachment	$e^- + AB \rightarrow AB^-$
Dissociation	$e^- + AB \rightarrow e^- + A + B$
Polar dissociation	$e^- + AB \rightarrow e^- + A^+ + B^-$
Dissociative ionisation	$e^- + AB \rightarrow 2e^- + A + B^+$
Dissociative attachment	$e^- + AB \rightarrow A + B^-$

The most important excitation, de-excitation and ionisation reactions within a DBD nitrogen plasma at atmospheric pressure are given below and highlight the complexity of the plasma chemistry by the following equations (according to [85-87]):



The chemical surface reactions of the radicals created by the nitrogen plasma with the surface of the polymer foil are not well understood. However, the initiation reaction usually

involves radical formation on carbon atoms of polymer chains via interaction with plasma radicals. This leads to the formation of various functional groups as well as crosslinking of polymer chains and scission of polymer chains (the latter in particular leading to creation of LMWOM [7]). The gas utilised in the plasma process has significant influence on the kind of chemical groups incorporated on the polymer surface and also, whether crosslinking or the creation of LMWOM is dominant in the process. The latter is also dependent on the dominant degradation mechanism of the polymer under such conditions, for example polyethylene generally tends to undergo crosslinking whilst polypropylene tends to undergo chain scission [88]. In general, however, plasmas ignited in inert gases, such as noble gases or nitrogen, favour crosslinking of the polymer [89], whereas plasmas containing higher amounts of oxygen can lead to the creation of LMWOM [3].

The functional groups incorporated by the nitrogen plasma treatment were studied by Guimond S. et al. [90] and Wang K. et al. [91] using attenuated total reflection Fourier transform infrared spectroscopy (ATR-FTIR). This technology is normally not suitable to detect the changes in the treated surface of the polymer, because the plasma affects only the outermost layers (i.e. the first few nm) [92] and ATR-FTIR (with penetration depth in the micrometre range) is not surface-sensitive enough to measure these changes. To overcome this problem, the samples need to be exposed to the plasma for several seconds via static treatment. This can lead to unrepresentatively severe degradation of the polymer surface whilst the thickness of polymer affected is increased sufficiently to enable resolution of the changes using ATR-FTIR.

The chemical groups on the surface of a BOPP sample treated by an atmospheric pressure nitrogen plasma are mainly amines, amides and hydroxyls. Whilst BOPP samples treated in air plasma featured carboxylic acid, ketone and ester groups [93].

## 5 Design of the laboratory scale DBD rig

This chapter describes the design and construction of the DBD rig and the electrode configurations, which were used to examine the optimal settings for the DBD surface treatment of the BOPP film on the laboratory scale. These settings were then transferred to an industrial process. The setup of the industrial machine is also explained in this chapter. The novelty of the laboratory DBD system in comparison to the plasma rigs of other researchers is the high amount of different parameters, which can be investigated. The design of the DBD system presented in this chapter allows to compare different electrode configurations and the variation of the dielectric thickness, as well as of the electrode distance.

### 5.1 Design of the process chamber

Although the experiments in this project are performed at atmospheric pressure, the application of a vacuum chamber is useful. The vacuum chamber can be evacuated down to a pressure of 1300 Pa with the E2M5 rotary vacuum pump (Edwards High Vacuum International) and then filled with the desired process gas or gas mixture. This procedure ensures that the atmosphere in the chamber has a high purity and furthermore, the implementation of a closed chamber protects the user from the release of hazardous chemicals, which could be produced during the plasma process.

The design of the vacuum chamber includes a hollow glass cylinder, a cover plate (made of polyamide 6.6), a metal ring and three hollow metal bars. The glass cylinder is encompassed between the metal ring and the cover plate. The three metal bars are screwed to the metal ring and go through the cover plate, where they are connected to a gas supply. The metal bars have holes next to the metal ring and a connection into the chamber. Two gas connections are used to feed gases into the chamber and an additional one is used to measure the pressure inside the chamber with a differential manometer. The metal bars also form a framework to hold the chamber together.

The cover plate has three feed-throughs; one in the middle for a connection to the rotary pump and two for cable glands for the high voltage cables which will supply the electrode configuration. All metal parts of the chamber are covered with epoxy resin to avoid unwanted discharges. A bracket for the electrode configuration is inserted between two metal bars. The opening in front of the chamber can be closed with an end cap, which is screwed

to the metal ring. O-rings are placed at all necessary locations. Figure 18 shows the vacuum chamber without the end cap.

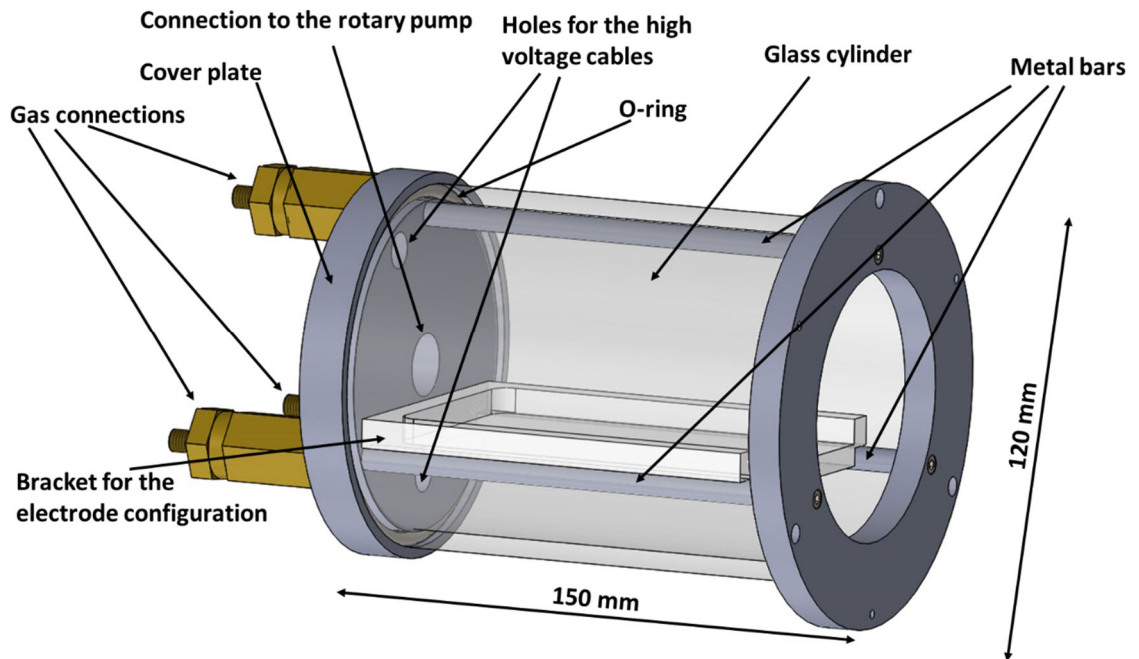


Figure 18: Dielectric barrier discharge plasma chamber

## 5.2 Reel-to-reel system with smooth profile parallel electrode configuration

The parallel electrode configuration with the reel-to-reel system was designed to be placed on the bracket within the vacuum chamber, shown in Figure 18. The parallel electrode configuration consists of two holders for the stainless steel electrodes. The electrodes have a size of  $34 \text{ mm} \times 15 \text{ mm}$  and their edges are rounded with radius of 5 mm and their borders with a radius of 1.5 mm to avoid increased electrical fields through edge effects. The holders have a central cut-out, where the electrodes are located. The electrodes are recessed flush to the holders in order that they form one continuous surface. A high voltage cable is soldered to an adhesive copper tape, which is then glued to the stainless steel electrodes. The cables are connected through the holder by a feedthrough on the backside. The remaining space in the feedthroughs was filled with epoxy resin, which prevents discharge from the electrode through the holder and holds the cables in place.

Both holders also have threaded holes and clearance holes, for four  $M4 \times 30 \text{ mm}$  long flat head screws, which locate the two holders together, with the electrodes facing each other. The gap between the electrodes is determined by the number of 0.5 mm thick vulcanised

fibre washers placed on each screw. The gap distance can therefore be changed in 0.5 mm steps by adding the required amount of washers. A sheet of a dielectric material can be clamped between the washers and the electrodes on each side in order that one or both electrodes are covered by the dielectric. The whole configuration is fixed with nuts on every screw. The material used for all parts apart from the electrodes and the washers is polyamide 6.6. Figure 19 illustrates the parallel plate configuration without dielectrics in place.

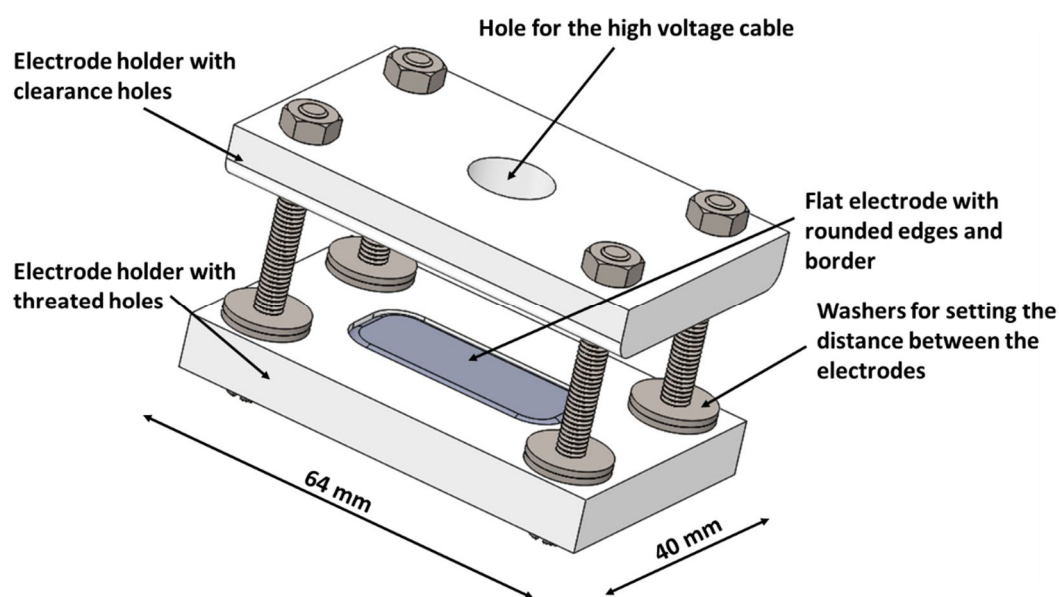


Figure 19: Design of the parallel electrode configuration with smooth surfaces

The reel-to-reel system is illustrated in Figure 20. It consists of two reels (unwind and rewind), which are mounted on a base plate with two brackets. The parallel electrode configuration is mounted on to the base plate via four threaded holes. The rewind reel is connected via two gears to a DC motor (Maxon, brushed DC motor, 2 Watt), which is connected to a DC power supply with the maximum settings of 30 V and 5 A. The cables for this are also feed through the same holes, which are already used for the high voltage cables.

At the beginning of the surface treatment, the BOPP film is coiled on the unwind reel and is then transferred with the help of the DC motor to the rewind reel, while passing through the gas gap of the electrode configuration. The height of the reels is thereby chosen, so that the film is held in contact with the dielectric, which is covering the upper electrode. Therefore only the surface of the BOPP film, which is facing the gas gap, is affected by the plasma,

while the other side stays untreated. Figure 21 illustrates how the BOPP film is transported through the electrode configuration, when the DC motor is supplied with power.

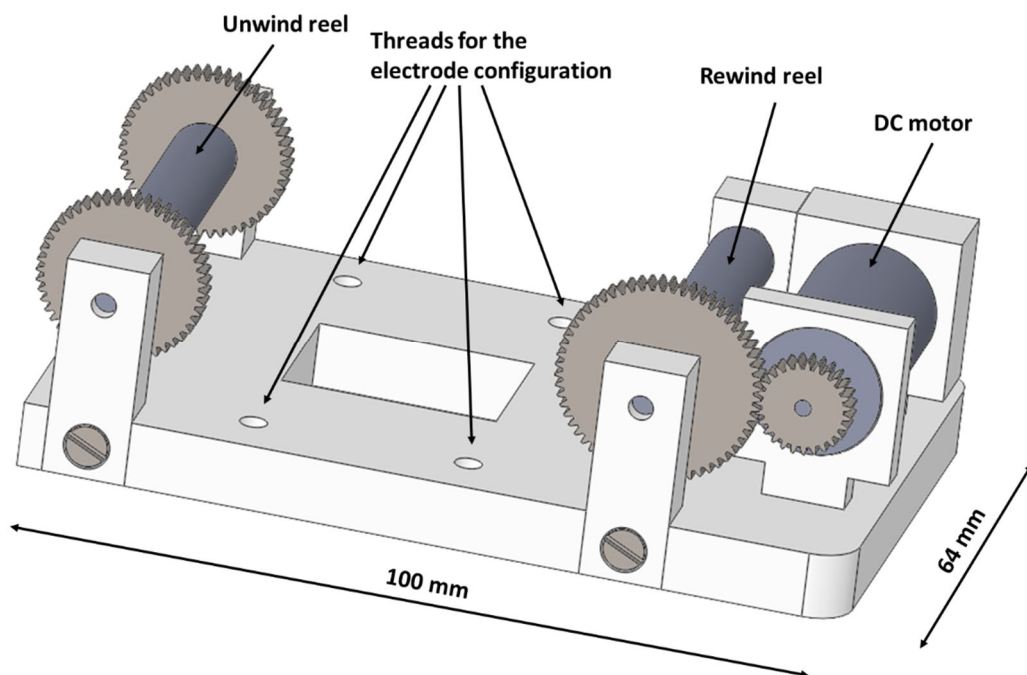


Figure 20: Reel-to-reel system

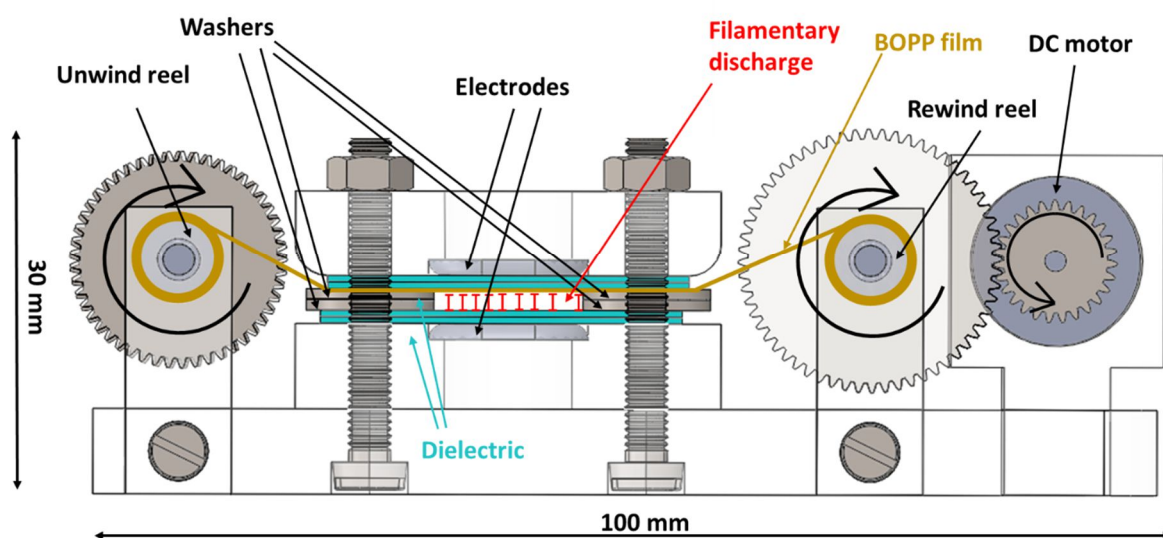


Figure 21: Pathway of the BOPP film during the plasma treatment

The reel-to-reel system was designed with minimum space requirements like the whole surface treatment system. As a result of the simple structure, the speed of the BOPP film during

the treatment is not constant. The rewind reel is driven directly by the DC motor, however the circumference of the rewind reel grows the more the film is rewound. Therefore, the linear velocity of the BOPP film increases as the amount of rewound film increases the diameter of the rewind reel. The increased speed leads to a reduced residence time of the BOPP film in the plasma zone, which could affect the intensity of the surface treatment. This effect must be considered, when samples of the treated BOPP film are examined with for example contact angle measurement.

The first experiments were conducted with static surface treatments (without the reel-to-reel system) of the BOPP film by placing the film on the lower electrode of a flat electrode configuration. However, this kind of treatment did not result in homogeneously treated samples. The memory effect causes that the filaments are ignited always at the same positions. Therefore, the samples treated by the static treatment did show spots, which were affected by the plasma, while other areas of the BOPP surface stayed mainly untreated. Furthermore, the BOPP film around the treated spots became bleared and lost its transparency. This is a clear identification that chemical structure of the BOPP film was damaged by overtreatment. To avoid the overtreatment the reel-to-reel system was added to the electrode configuration. By transporting the BOPP film by the reel-to-reel system through the gas gap the contact time of the polymer film with the plasma is dramatically reduced relative to the static treatment. This ensures that only the surface of the BOPP film is treated and the bulk is not affected.

A second result of these first experiments was, that the electrode area of the flat electrode configuration needs to be reduced, in order that the filaments are ignited close to each other. Only then, it is ensured that the filaments are overlapping, which provides are more homogeneous surface treatment of the BOPP films. This is the case for the flat electrode configuration presented in Figure 21.

### **5.3 Parallel electrode configuration with sawtooth electrode profile**

A second kind of electrode configuration was designed to better represent an industrial DBD systems (shown by Figure 11). The upper electrode is flat with the dimensions 34 mm×26 mm. The edges of the electrode are rounded with a radius of 5 mm. The electrode is located in an electrode holder and connected with a high voltage cable in the same manner as already described in Chapter 5.2. The counter electrode has a sawtooth shape and is manufactured from aluminium. The sawtooth electrode is directly fixed on the reel-to-reel system without

a holder by a double-sided adhesive tape. Three types of the sawtooth electrode with different amounts of teeth (1, 3 and 5) were used in this project. They are illustrated in Figure 22.

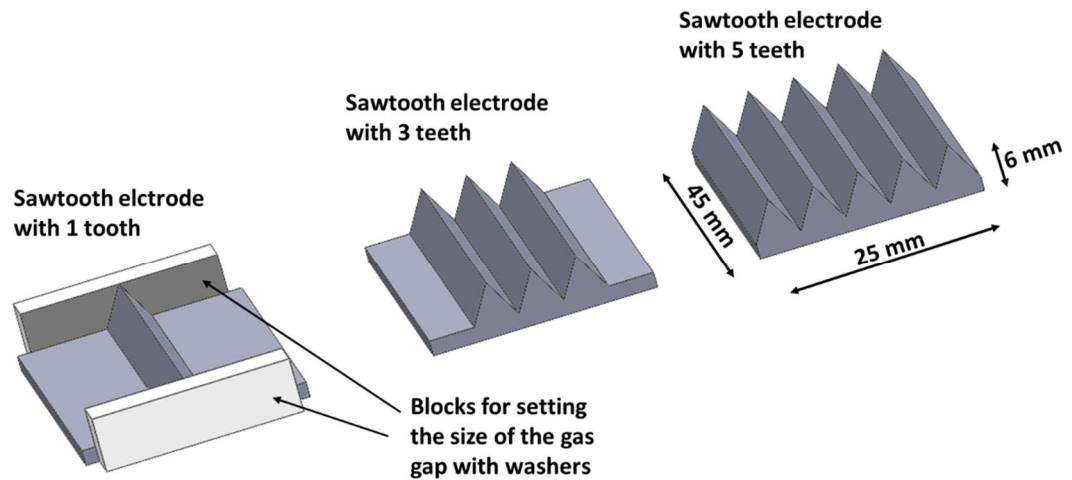


Figure 22: The three different sawtooth electrodes used in this project with 1, 3 and 5 teeth

The corrugated shape of the sawtooth electrodes concentrates the streamers of the filamentary discharge on top of the teeth. Thus it is possible to ignite the streamers very close to each other and align them. In order that the gap distance can be adjusted with washers, two blocks (made of polyamide 6.6) with the same height as the sawtooth electrodes were mounted to sides of each sawtooth electrode. The pathway of the BOPP film during the plasma treatment is not changed by the utilisation of the different electrode configuration. Due to the corrugated shape, the sawtooth electrodes cannot be covered by a dielectric sheet. The reel-to-reel system with the adjusted sawtooth electrode configuration is shown in Figure 23.

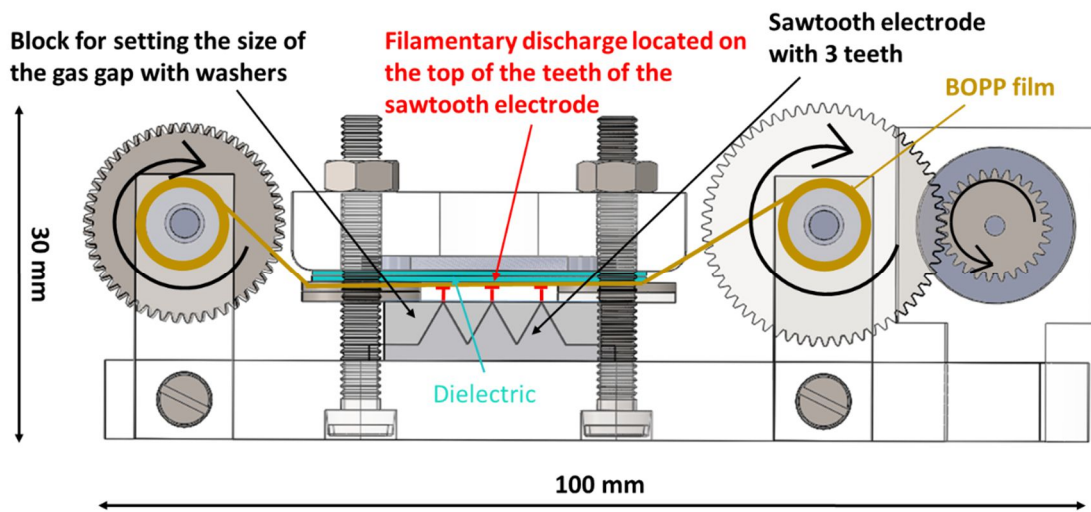


Figure 23: Reel-to-reel system with sawtooth electrode configuration

#### 5.4 Overall view on the gas chamber with reel-to-reel system and electrode configuration

The DBD system designed offers a lot of flexibility. The electrode configuration can be varied in terms of the size of the gas gap between the electrodes and type, as well as thickness of dielectric material. One or both electrodes can be covered by the dielectric, when flat electrodes are utilised. The flat electrode configuration can also be replaced with a sawtooth-flat electrode pair to be able to study, how the plasma treatment changes when the streamers of the filamentary discharge are concentrated on one or several lines. In this configuration, the sawtooth electrode is not covered with a dielectric.

A reel-to-reel system transports the BOPP film through the plasma zone in the gas gap between the two electrodes. A DC motor drives the rewind reel by two gears. Depending on the power, applied to the DC motor, the speed of the film can be varied. The speed of the film is during the treatment not constant and increases as the film is rewound.

The reel-to-reel system with various the electrode configurations is dimensioned to fit on a bracket inside a vacuum chamber. A rotary pump evacuates the air inside the chamber. Afterwards, the chamber can be filled with any required gas or gas mixture, in order that the plasma treatment is performed in the desired atmosphere at atmospheric pressure. The diffusion of impurities from outside is prevented by a small overpressure inside the chamber.

The whole DBD configuration is designed in order that the different settings and samples can be changed with minimum effort. This system is well-suited for the treatment of a large amount of samples in a short time. Figure 24 shows the reel-to-reel system with the flat electrode configuration on the bracket inside the vacuum chamber.

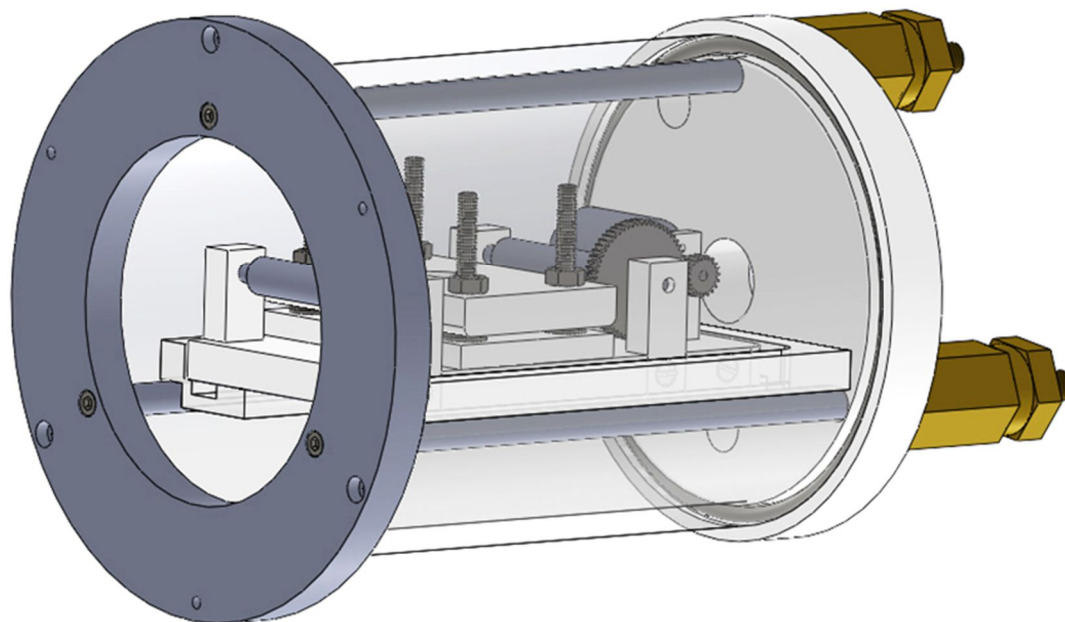


Figure 24: Reel-to-reel system with flat electrode configuration inside the vacuum chamber

## 5.5 High voltage power supply of the laboratory scale system and measurement of the electrical characteristics

The high voltage power supply of the laboratory scale DBD configuration consists of a function generator (TG 2000 20 MHz DDS, Aim-TTi), a DC power supply (GPR-11H30D, GW Instek), an amplifier and a transformer (AD6170, Amethyst-designs). The maximum settings of the DC power supply are 110 V and 3 A. The amplifier was designed by the research group of Prof Bradley, University of Liverpool. The circuit diagram of the amplifier with all electronic parts is given in the Appendix A. The low voltage side of the transformer has seven turns and the high voltage side 1200 turns.

The amplifier processes the signals from the function generator and the DC power supply and gives an AC signal to the transformer, which transforms the low voltage signal to a high

voltage sinusoidal signal, which is then applied to the electrode configuration. A current probe (Pearson current monitor model 4100, Pearson Electronics) and a voltage probe (PVM-6, 1000:1, North Star High Voltage) measure the applied voltage and the discharge current on the high voltage side of the electrical circuit. For this purpose, the probes are connected behind the electrode configuration. To be able to calculate the charge, which is transferred during the discharge, a measurement capacitor (TDK Corporation) with a capacitance of 560 pF is connected in series to the electrode configuration. The voltage drop is measured across the capacitor with a voltage probe (GE-3121, 100:1, Elditest). The DPO 3014 oscilloscope (Tektronix) records all signals. The complete experimental setup is shown in Figure 25.

The important properties of the measurement capacitor are a high breakdown voltage of 50 kV and a low dissipation factor of maximal 0.2%. The dissipation factor is the loss of electric energy in an alternating electrical field, which is changed into heat inside the dielectric. The heat is created by the polarisation of the molecules of the dielectric through the alternating electrical field. The dielectric loss causes a distortion of the measured voltage drop across the measurement capacitor and must therefore kept as small as possible.

The transferred charge,  $q$ , is calculated from the measured voltage drop,  $V_d$ , and the known capacitance of the measurement capacitor,  $c_{meas}$ :

$$q(t) = c_{meas} \cdot V_d(t) \quad (5)$$

The amplitude of the signal from the amplifier to the transformer is dependent on the selected function and frequency of the function generator and on the voltage amplitude of the DC power supply. The voltage settings of the DC power supply are adjusted to the maximum and the set value is the current. This means, that the voltage floats to the adjusted current and is increased with higher current settings. The voltage amplitude of the function generator has no influence on the signal of the amplifier. However, a minimum value of 6 V is necessary in order that the signal is processed by the amplifier. The function generator is able to create sinusoidal, square and triangle waveforms with frequencies from Hz to MHz. Moreover, also positive and negative pulses are possible. The signal given from the amplifier to the transformer is always an AC signal independent on the selected function of the function

generator. The selected function has only influence on the amplitude of this AC signal. The frequency of the applied voltage on the high voltage side is the same as the selected using the function generator.

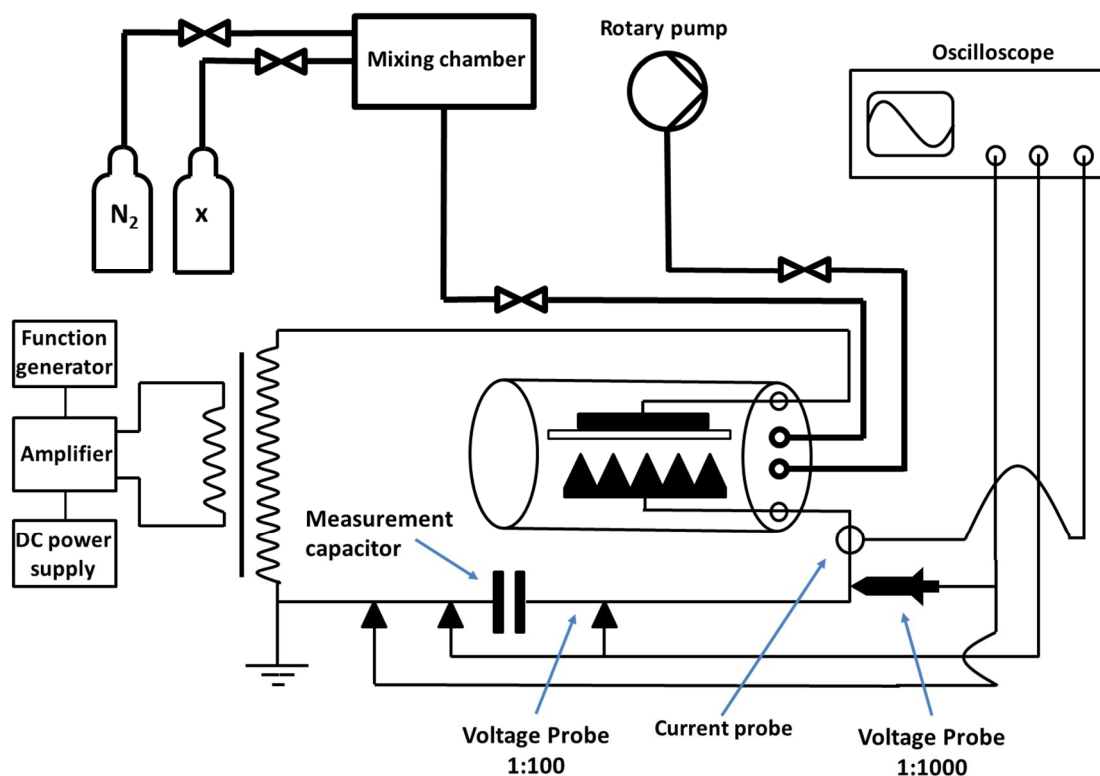


Figure 25: Experimental setup of the laboratorial scale DBD system

## 5.6 Setup of the industrial scale DBD system

The main difference between the industrial scale DBD system and the previously presented laboratory scale system is that the industrial machine does not use a closed chamber. It is thus an open system. The DBD configuration, discussed in this section, has already been schematically illustrated in Figure 11.

The grounded electrode of the industrial DBD configuration is a drum, which also transports the BOPP film through the plasma during the treatment. The drum has a diameter of 1.2 m and a width of 2.5 m. The dielectric covering the drum is a 5 mm thick layer of silicone. The film passes around this dielectric during the treatment. The counter electrode has the dimen-

sions of  $1.2 \text{ m} \times 0.15 \text{ m}$  and is corrugated perpendicular to the machine direction. Four counter electrodes are equally spaced around the lower half of the drum electrode. They are made of aluminium and each counter electrode is powered by its own generator with up to 20 kW. The gas gap between the counter electrode and the drum is continuously variable from  $900 \mu\text{m}$  and  $2000 \mu\text{m}$ .

In order that the surface treatment can be performed in the desired nitrogen atmosphere, gas nozzles are positioned in the front of every electrode along their entire length. The gas flow of these nozzles amounts to 4.7 slm per metre during the treatment. Simultaneously, the air at the circumference electrode configuration is sucked in a slot at both sides. Thereby, the contamination of the process gas with air is prevented. A sensor between the two electrodes measures the concentration of oxygen in the process gas and stops the surface treatment if the oxygen concentration exceeds a value of 16 ppm. The BOPP film is treated at a speed of up to 300 m/min. Figure 26 shows the industrial DBD system with the drum and counter electrode separated in the open position.

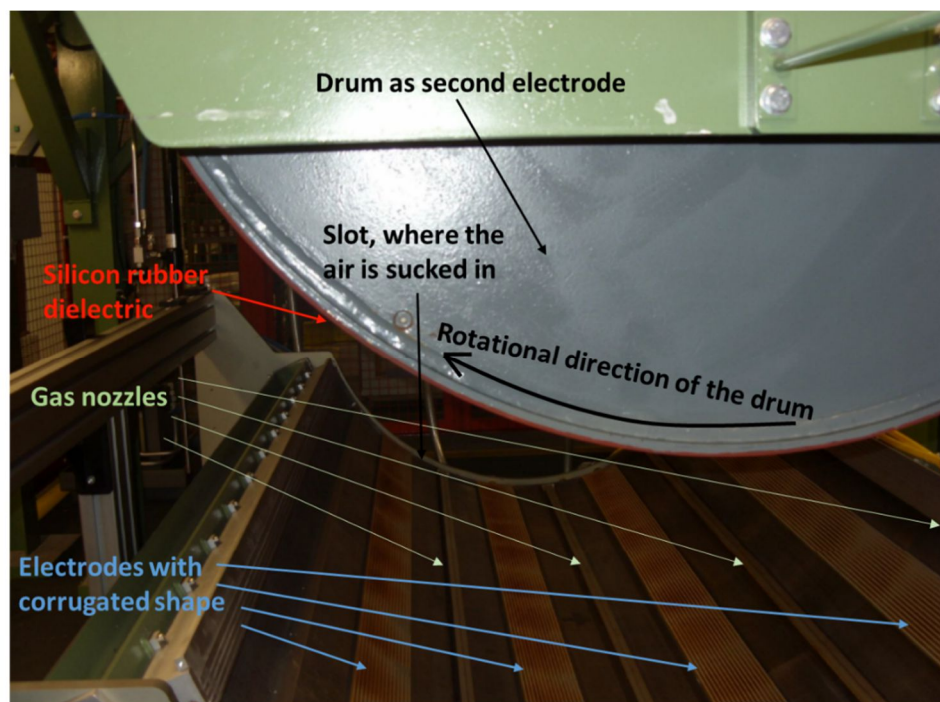


Figure 26: Industrial DBD system in open position

## 6 Analytical techniques

This chapter describes the Lissajous figure; an analytical method, which is used to examine the electrical characteristics of the high voltage cycle of the laboratory DBD system. With this method, the consumed electrical power and the minimum voltage to ignite the discharge can be examined. Furthermore, the measurement techniques for the characterisation of the untreated and of the plasma treated samples are explained. These techniques are the contact angle measurement and the X-ray photoelectron spectroscopy (XPS). It also should be mentioned that the BOPP films were investigated with attenuated total reflection Fourier transform infrared spectroscopy (ATR-FTIR) to get more information about the chemical groups incorporated on the surface of the plasma treated films. However, the measured spectra of treated and untreated samples did not show any differences to each other, which led to the conclusion, that the ATR-FTIR measurement is not surface-sensitive enough (penetration depth in order of microns) to investigate the chemical composition of the BOPP films after the plasma treatment.

### 6.1 Lissajous figures

The Lissajous figures are an important diagnostic tool for the electrical characterisation of DBDs and has become a standard measurement technique for their specification. Lissajous figures are created by plotting the charge, which is transferred during the discharge, against the applied voltage of the high voltage circuit. The result is ideally a parallelogram, which illustrates the discharge behaviour over one cycle duration. Figure 27 shows schematically a Lissajous figure of a DBD driven by a sinusoidal voltage.

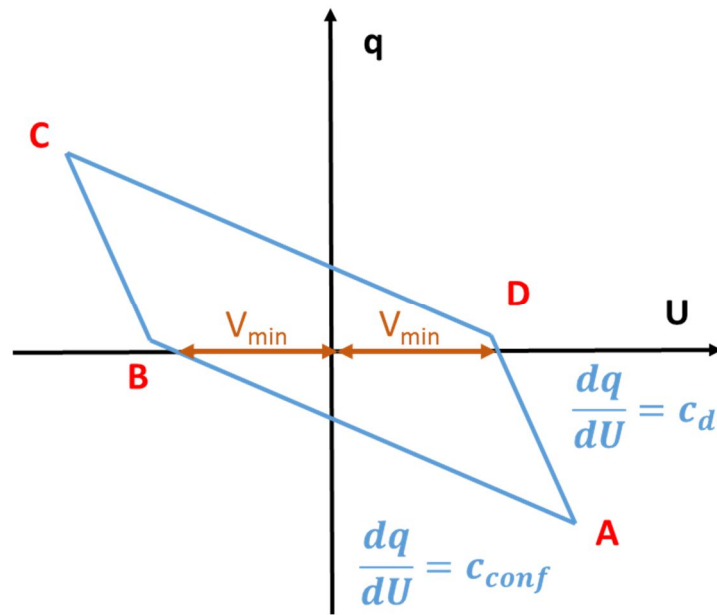


Figure 27: Idealised Lissajous figure of a DBD driven by sinusoidal voltage

The Lissajous figure in Figure 27 shows two different regions of the DBD characteristics. From the points A to B and the points C to D, the discharge is not ignited. The amount of transferred charge is relatively low. The reason for the low charge transfer is the replacement current. From the points B to C and the points D to A, the discharge is ignited. The charge transfer is high, because a high current flows in the gas gap via the establishment of electron avalanches. The slope of the straight lines AB and CD equals the capacitance of the DBD configuration,  $c_{conf}$ . The DBD configuration is a plate capacitor with a series connection of the capacitance of the gas gap,  $c_g$ , and of the dielectric,  $c_d$  (Equation 6):

$$\frac{1}{c_{conf}} = \frac{1}{c_d} + \frac{1}{c_g} \quad (6)$$

Solving Equation 6 for  $c_{conf}$  results in Equation 7:

$$c_{conf} = \frac{c_d \cdot c_g}{c_d + c_g} \quad (7)$$

During the discharge, the gas becomes conductive and thus loses its ability to store electrical charge. Therefore, the slope of the straight line BC and DA equals only the capacitance of the dielectric,  $c_d$ .

The main reason why the Lissajous figures are used for the characterisation of DBDs is that the electrical power of the plasma,  $P_{el}$ , can be relatively easily estimated from them. It is also possible to calculate  $P_{el}$  from the applied voltage and the discharge current. However, it is reported that measurement of discharge current of filamentary discharge is of lower accuracy than measurement of the time-integrated signal of the current, which is the charge [46, 94]. The reason for the lower accuracy of the former approach is the nanosecond duration of the current pulses (shown by Figure 17), which requires a current probe with a frequency bandwidth within the megahertz range.

For calculation of consumed power of the DBD configuration,  $P_{el}$ , using the Lissajous figure, the area bounded by the Lissajous figure has to be calculated. The area is equal to the consumed electrical energy,  $W_{el}$ , during one discharge cycle [9, 92, 95, 96] (Equation 8).

$$W_{el} = \int_{t=0}^T V(t)dq = c_{meas} \int_{t=0}^T V(t)dV_d \quad (8)$$

By multiplying the discharge energy,  $W_{el}$ , by the frequency of the applied voltage,  $f$ , the electrical power,  $P_{el}$ , is calculated (Equation 9):

$$P_{el} = f \cdot W_{el} \quad (9)$$

Another advantage of the Lissajous figures is the possibility of estimating the minimum voltage,  $V_{min}$ , which is necessary to ignite the discharge. This value can be determined from the Lissajous figure at the point where the voltage function intercepts zero charge. The minimum voltage,  $V_{min}$ , is therefore not equal to the breakdown voltage,  $V_b$ , which was discussed in Chapter 2.3. The difference is that the breakdown voltage was defined for an electrode configuration without a dielectric. The minimum voltage required to ignite a DBD is higher, because the dielectric causes loss of electric energy, i.e. the dielectric loss, which must be compensated for by a higher voltage.

## 6.2 Contact angle measurement using the sessile drop method

Contact angle measurement (also called goniometry) using the sessile drop is a method for estimation of the surface energy of a solid substrate. A droplet of a probe liquid with known surface energy is applied to the solid substrate. The solid substrate, the liquid and the surrounding gaseous atmosphere form a three phase system. A tangent is then drawn at the point, where all three aggregate phases meet each other, along the profile of the drop. The contact angle,  $\Theta$ , is measured between this tangent and the baseline of the droplet (Figure 28).

The estimation of the solid surface energy,  $\gamma_s$ , utilises on the Young-equation [97], which relates the contact angle,  $\Theta$ , with the three interfacial tensions of solid-vapour, solid-liquid and vapour-liquid, while the mechanical equilibrium between the three phases is fulfilled.

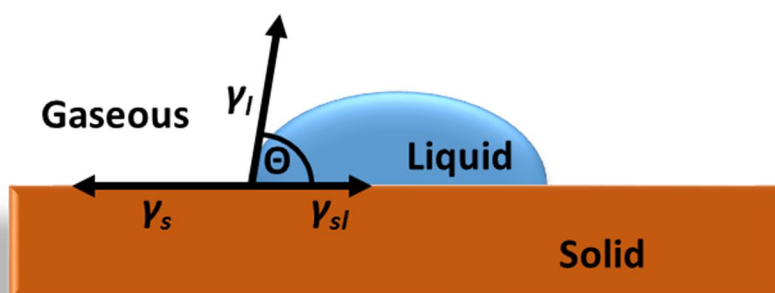


Figure 28: Contact angle between the liquid and solid phase

Equation 10 is a simplified version of the Young-equation, which is more commonly used for the determination of the solid substrate surface energy [98]. In this equation the solid-vapour tension is replaced by the surface energy of the solid,  $\gamma_s$ , and the surface energy of the liquid,  $\gamma_l$ , substitutes the vapour-liquid tension. The solid-liquid tensions,  $\gamma_{sl}$ , remains.

$$\gamma_l \cdot \cos \theta = \gamma_s - \gamma_{sl} \quad (10)$$

Equation 10 contains the two unknown variables, the solid-liquid tension,  $\gamma_{sl}$ , and the solid surface energy,  $\gamma_s$ , and hence is not solvable. The contact angle,  $\Theta$ , is the measured physical

quantity and the surface energy of the liquid,  $\gamma_l$ , is known. To be able to solve the equation, different concepts were developed. The most important are originated by Fowkes [99-101], Owens and Wendt [102], van Oss, Chaudhury and Good [103], Wu [104, 105], as well as Fox and Zisman [106, 107].

In this project, the Owens-Wendt-Rabel-Kaelble [108, 109] method is utilized, which is one of the most commonly applied procedures to estimate the surface energy of solid substrates [110, 111]. This theory divides the surface energy into two components: the polar and the dispersive part. This two component model describes good wettability between a solid substrate and a liquid not only by a similar surface energy, it is also necessary, that the polar part and the dispersive part of the surface energy are as close as possible. The polar part describes the sum of the polar interactions, such as hydrogen bonds, as well as dipole-dipole and acid-base interactions. The dispersive interactions are based on temporary variations in the electron density of the molecules. These weak interactions are also known as London forces or van der Waals forces. The surface energy within one phase is the sum of the dispersive part and the polar part:

$$\gamma_l = \gamma_l^p + \gamma_l^d \quad (11)$$

$$\gamma_s = \gamma_s^p + \gamma_s^d \quad (12)$$

The solid-liquid tension,  $\gamma_{sl}$ , is calculated based on the two surface energies of the solid,  $\gamma_s$ , and the liquid phase,  $\gamma_l$ , as well as the interactions of the two phases. These interactions are the geometric mean of the polar and the dispersive part of both phases:

$$\gamma_{sl} = \gamma_s + \gamma_l - 2 \left( \sqrt{\gamma_s^d \cdot \gamma_l^d} + \sqrt{\gamma_s^p \cdot \gamma_l^p} \right) \quad (13)$$

Combining Equation 13 with the Young-equation (Equation 10) results in:

$$\gamma_l \cdot (\cos \theta + 1) = 2 \left( \sqrt{\gamma_s^d \cdot \gamma_l^d} + \sqrt{\gamma_s^p \cdot \gamma_l^p} \right) \quad (14)$$

Rearranging Equation 14 yields in a linear equation of the kind:

$$\underbrace{\frac{\gamma_l \cdot (\cos \theta + 1)}{2 \cdot \sqrt{\gamma_l^d}}}_y = \underbrace{\sqrt{\gamma_s^p}}_m \cdot \underbrace{\frac{\sqrt{\gamma_l^p}}{\sqrt{\gamma_l^d}}}_x + \underbrace{\sqrt{\gamma_s^d}}_t \quad (15)$$

The only two unknown variables in Equation 15 are the polar and the dispersive part of the solid,  $\gamma_s^p$  and  $\gamma_s^d$ . These variables can be determined by measuring the contact angle,  $\theta$ , of the solid substrate with at least two different testing liquids. The polar and the dispersive part,  $\gamma_l^p$  and  $\gamma_l^d$  of the surface energy of the liquid must be known and the polar part of at least one has to be a non-zero number. With the measured contact angles, the terms  $y$  and  $x$  of Equation 15 can be calculated for every test liquid used. The obtained values are then plotted and the slope,  $m$ , and the  $y$ -intercept,  $t$ , are determined via linear regression. The slope,  $m$ , equals the polar part of the surface energy of the solid substrate,  $\gamma_s^p$ , and the  $y$ -intercept is the dispersive part,  $\gamma_s^d$ .

It is important that the test liquids do not dissolve or penetrate into the BOPP substrate in order to avoid the value of the contact angle being affected. Three test liquids have been chosen for this project: distilled water, diiodomethane and ethylene glycol. They have been already been utilised by other researchers to investigate the surface energy of PP [112, 113]. The values for the total surface energy, the polar part and the dispersive part of the three testing liquids are presented in Table 6.

Table 6: Total surface energy, the polar and dispersive part of the testing liquids [114]

	<b>Total surface energy, <math>\gamma_l</math></b> <b>[mN/m]</b>	<b>Dispersive part, <math>\gamma_l^d</math></b> <b>[mN/m]</b>	<b>Polar part, <math>\gamma_l^p</math></b> <b>[mN/m]</b>
Water	72.8	21.8	51.0
Diiodomethane	50.8	50.8	0.0
Ethylene glycol	47.7	30.9	16.8

The drops positioned on the BOPP substrate were monitored using the MobileDrop GH11 (Krüss GmbH) measuring system. The “drop shape analysis” analysis software was utilised to measure the contact angle using the Young-Laplace fit. According to the manufacturer, this method offers the best correspondence between the theoretical and real drop shape in the case of a symmetric, undistorted drop on a smooth surface [115].

In addition to the contact angle measurement, the surface energy of the plasma treated films was investigated using Dyne Inks and Pens. This method uses pens, which are filled with a coloured ink and different solvents. The combination of the solvents determines the surface energy of the ink-solvent-mixture. The surface energy value is written on the side of the pen. This method utilising Dyne Inks and Pens forms the basis of the ASTM D2578 Standard [116].

A continuous line is drawn with the pen on the treated BOPP film to be investigated and afterwards the wetting ability of the ink-solvent-mixture is evaluated visually. If the ink-solvent-mixture wets the BOPP film properly, the value of surface energy of the film is equal to or greater than the value written on the used pen used. If the wetting is poor, the ink-solvent-mixture starts to form droplets on the sample and the drawn line is thus not consistent, i.e. the ink does not wet the film. In this case, the surface energy of the film is lower than the value on the pen. Two different pens with surface energy of 38 mN/m (Softal electronics GmbH) and of 50 mN/m (Corona Supplies Ltd) were used in this project. Figure 29 illustrates the difference between good and poor wettability between a BOPP film with untreated and plasma treated regions and an ink-solvent-mixture with a surface energy of 38 mN/m.

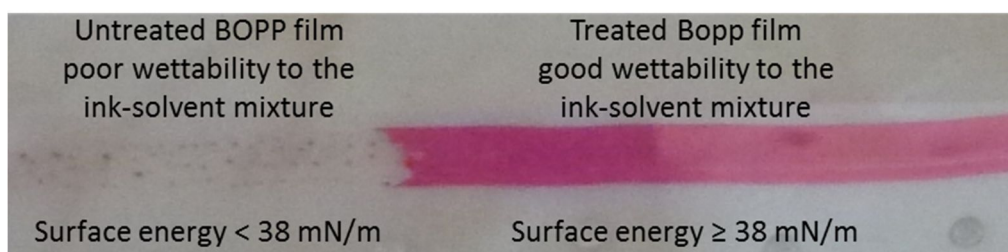


Figure 29: Good and poor wettability indicated by use of a Dyne pen with a surface energy of 38 mN/m to a BOPP film with untreated and plasma treated regions

### 6.3 X-ray photoelectron spectroscopy

X-ray photoelectron spectroscopy, which is also known as electron spectroscopy for chemical analysis, is a highly sensitive surface analysis technique used under ultra-high vacuum conditions (lower than  $10^{-7}$  Pascal). The XPS characterises solid materials at a depth of approximately ten nm [116]. The information gained by this analysing method is the elemental composition of the investigated surface, which includes the qualitative and quantitative analysis.

The principle is that the sample is irradiated with monochromatic X-rays of known energy. The X-rays cause the emission of electrons by the photoelectric effect from the surface atoms of the sample. The kinetic energy of the released electrons is measured by an electron energy analyser, which allows the calculation of the binding energy of the electrons. The binding energy of the electrons from the inner shells is characteristic for every element. Thereby, all elements of the sample's surface can be identified and the composition of the surface in atomic percent is determined from the amount of detected electrons for each element. Only helium and hydrogen cannot be detected with XPS, because the cross section of their 1s atomic orbital is very small for the photoelectric effect. Furthermore, hydrogen and helium only have one orbital, which is the valence orbital. A core orbital is missing. This makes their detection impossible, because there is no way to distinguish the electrons of the 1s valence orbital from the electrons of other valence orbitals, which would belong to elements other than hydrogen or helium [117].

In order that a photoelectron reaches the electron energy analyser, it is necessary, that it travels through the sample and escapes into the vacuum. Free electrons can cause inelastic and elastic collisions or recombination reactions. These effects reduce the amount of released electrons, which reach the electron energy analyser. The probability of these effects grows exponentially with the sample depth. As a result, mainly photoelectrons from the layers closer to the surface of the sample, are detected, which makes this method to a highly surface sensitive analysis tool. However, this ability also necessitates that the measurement is performed under ultra-high vacuum. Only under these conditions, it is ensured, that no contaminations on the surface of the sample distorts the measurement.

The analysis of a measured XPS spectrum starts with the identification of the individual peaks, which are characteristic for every chemical element by the individual binding energy of the detected electrons. Variations in the elemental binding energies arise from differences

in the chemical neighbourhood and binding state. These chemical shifts can be used to identify the chemical state of the materials being analysed.

## 7 Design of Experiments: The D-optimal approach

In this project the D-optimal design of the Design of Experiments (DoE) is utilised to optimise and investigate the surface treatment of commercially available BOPP films with the laboratory scale DBD system. For this, a set of systematically selected experiments are performed to study the behaviour of the DBD system and to develop a cubic regression model.

### 7.1 Principles of the design of experiment

To be able to understand the principles of DoE, two different variables have to be discussed: factors and responses. The factors are set values, which influence the experiment. The response is a measured information, gained from the experiment. The information depends on the set values of the factors.

Simple experimental design according to the type “change only one separate factor at a time till no further improvement is accomplished” is unfortunately inappropriate, if more than one value has influence on the response, because this method does not necessarily lead to the optimum conditions. This fact is illustrated in Figure 30. The first set of experiments leads to the optimisation of factor  $x_1$ . The second sets of experiments is implemented to improve the factor  $x_2$  on the basis of the estimated optimal value of  $x_1$ . However, this experimental design does not hit the optimal response area.

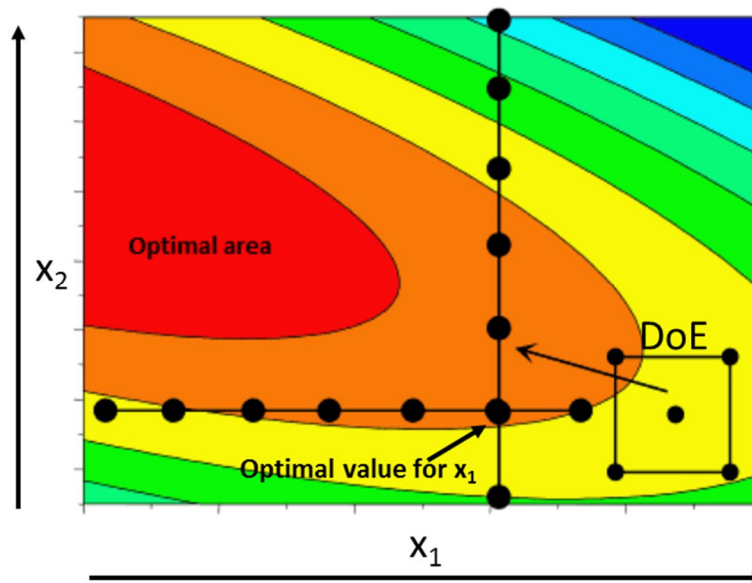


Figure 30: Experimental design by changing only one separate value at a time without reaching the optimal response area according to [118]

The better approach to finding the optimum values is to change of all factors simultaneously, which is done using the concept of DoE. Additionally, also possible interactions of factors, which influence the response can be investigated with DoE.

The factors can be classified into quantitative and qualitative factors. Quantitative factors have a given range and also a continuous scale, whereas qualitative factors own only one value. An example for a quantitative factor for this project is the size of the gas gap between the electrodes, which can be changed in certain steps. The treated film can be seen as a qualitative factor. The qualitative value of this factor could be the manufacturer. This makes sense, if films from different manufactures are treated and examined. Experimental arrays with qualitative factors are able to investigate, whether the factors have a significant influence on the response with the variance analyses. Regression analyses are performed with experimental arrays with quantitative factors. The aim is to find the functional correlation between the factors and the response.

The basic concept of DoE is to define a standard reference experiment and then change the values of the factors of the standard experiment such that new experiments are evolved symmetrically around the standard reference, which thus becomes the centre-point of the experimental array. This basic concept is also illustrated in Figure 31 for an experimental array with three factors.

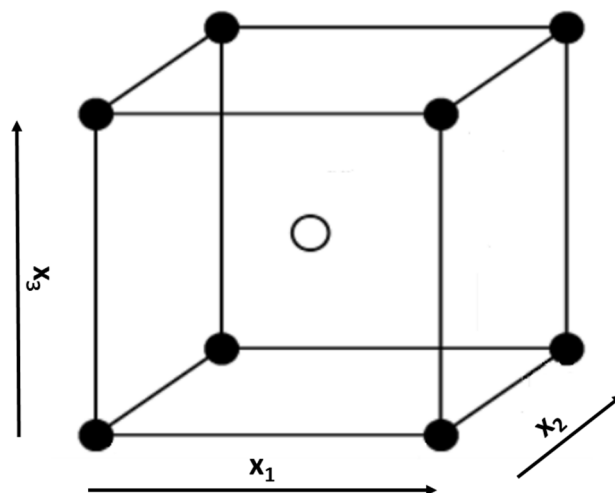


Figure 31: Symmetrical distribution of experiments around the standard reference experiment as centre point of an experimental array with three factors on two levels

At the beginning of a new DoE project, the problem formulation is from fundamental importance. There are five objectives of the problem definition: the classification of the experimental objectives, the definition of the factors, the definition of the responses, the specification of the regression model and the design of the experiments.

The experimental objective defines the reason, why an investigation is undertaken. Possible experimental objectives are the optimisation of an industrial process or the scientific investigation of a specific system. The factors are the different variables, which are changed during the experiments and the responses are the measured values. The regression model is specified as a polynomial model, which has to correspond to the chosen experimental objective. For example, the optimisation of an industrial process often requires only a simple linear model, because merely the information “does the change of the factor lead to a better response” is sufficient. In contrast, a scientific investigation needs more complex models of quadratic and cubic forms, which also consider interactions between the factors. These kind of models are able to describe the investigated process more precisely and offer more information about how the factors influence the process. The next step is the experimental design, which mainly depends on the chosen regression model and the range of the factors.

## 7.2 The different regression models and the estimation of the regression coefficients

Three main types of regression models exist: linear, quadratic and cubic. The aim of the regression is to model the response,  $y$ , as a function of the factors,  $x_n$ . For this, the independent regression coefficients,  $a_n$ , need to be estimated, in order that the data points of the factors and the response provide the best fit to the regression model. The best fit is found with the least-squares approach, which estimates the regression coefficients, so that the sum of the squared residuals of the measured points and the regression function are minimised. The quality of the regression is stated by the coefficient of determination,  $R^2$ , which has a value between 0 and 1, whereby 1 is a perfect fit and 0 means there is absolutely no correlation. The three different regression models are expressed by the following equations (Equation 16-18), whereby  $k$  is the amount of factors.

$$\text{Linear} \quad y = a_0 + \sum_{n=1}^k a_n x_n + \sum_{n=1}^{k-1} \sum_{m=n+1}^k a_{nm} x_n x_m \quad (16)$$

$$\text{Quadratic} \quad y = a_0 + \sum_{n=1}^k a_n x_n + \sum_{n=1}^k a_{nn} x_n^2 + \sum_{n=1}^{k-1} \sum_{m=n+1}^k a_{nm} x_n x_m \quad (17)$$

$$\begin{aligned} \text{Cubic} \quad y = & a_0 + \sum_{n=1}^k a_n x_n + \sum_{n=1}^k a_{nn} x_n^2 + \sum_{n=1}^k a_{nnn} x_n^3 \\ & + \sum_{n=1}^{k-2} \sum_{m=n+1}^{k-1} \sum_{l=n+2}^k a_{nmo} x_n x_m x_l \\ & + \sum_{n=1}^{k-1} \sum_{m=n+1}^k a_{nnm} x_n^2 x_m + \sum_{n=1}^{k-1} \sum_{m=n+1}^k a_{nmm} x_n x_m^2 \\ & + \sum_{n=1}^{k-1} \sum_{m=n+1}^k a_{nm} x_n x_m \end{aligned} \quad (18)$$

The complexity of the models is increased from the linear to the cubic model. This can be easily seen with the growing amount of mathematical terms, which are necessary to describe the respective model. These models also exist without the consideration of the interaction terms of the factors,  $x_n x_m$ ,  $x_n x_m x_o$ ,  $x_n^2 x_m$  and  $x_n x_m^2$ . A more complex model is generally able to describe the response as a function of the factors with a higher accuracy. However, the quantity of experiments, which have to be performed to estimate the different regression coefficients, is obviously increased with a more complex model, because the type of the regression model determines, how often one factor needs to be changed in the experimental design. For the linear model, the factors are changed on two levels; the square model needs already three levels and the cubic four. The quantity of necessary experiments also depend on the amount of the factors and the statistical design.

The regression coefficients are calculated with a matrix operation. Therefore, the regression models of Equations 16, 17 and 18 are expressed by matrices and vectors:

$$Y = X \cdot A \quad (19)$$

$$\text{with } Y = \begin{bmatrix} y_1 \\ y_2 \\ \dots \\ y_i \end{bmatrix} \quad X = \begin{bmatrix} 1 & x_{11} & \dots & x_{1j} \\ 1 & x_{21} & \dots & x_{2j} \\ \dots & \dots & \dots & \dots \\ 1 & x_{i1} & \dots & x_{ij} \end{bmatrix} \quad A = \begin{bmatrix} a_1 \\ \vdots \\ a_i \end{bmatrix}$$

The matrix  $X$  contains the different settings of the factors and the index  $j$  equals the quantity of regression coefficients to be determined. These can be calculated with the following matrix operation:

$$A = (X^T X)^{-1} X^T Y \quad (20)$$

The mathematical effort to solve Equation 20 is high and is thus often operated with a statistical computer program. With the modulus of the regression coefficients, the influence of the factors on the process can be appreciated.

### 7.3 The basic experimental designs

To solve the different regression models, various statistical designs were developed. There are three basic designs: the full factorial design, the fractional factorial design and the central composite design. The Plackett-Burman design, the Taguchi design and the optimal designs can be deduced from these basic designs. All designs have different features and application areas.

The full factorial design is made by combining all values of the factor levels with each other. The factors need to be orthogonal to each other, which means there is no correlation between them and the levels of the factors can be set individually. The number of required experiments is maximal, which makes this design to the best evaluable, but also unsuitable for experimental arrays with many factors and a complex regression model.

The fractional design is also based on orthogonal factors. The quantity of experiments is strongly reduced in comparison to the full factorial design, because the value of one or more factors is set dependent on the values of the other factors and not individually. Depending on the quantity of unperformed experiments (i.e. possible combinations of factors not tested), the evaluation of certain interactions are not possible anymore or are confounded with each other. A good evaluation of complex quadratic and cubic models is only possible, if the amount of reduced experiments is not too high. Therefore, the fractional design is mainly suited for the investigation of linear regression models.

The central composite design is based on a full factorial, but the number of experiments is increased by a centre point experiment, which is also often repeated at least twice. There are also several axial star point experiments, which define a spherical experimental space. The levels of the star point experiments are higher than the levels of the other experiments and allow the estimation of quadratic effects. However, the experimental effort is significantly enhanced. Figure 32 illustrates graphically the full factorial, fractional and the central composite design.

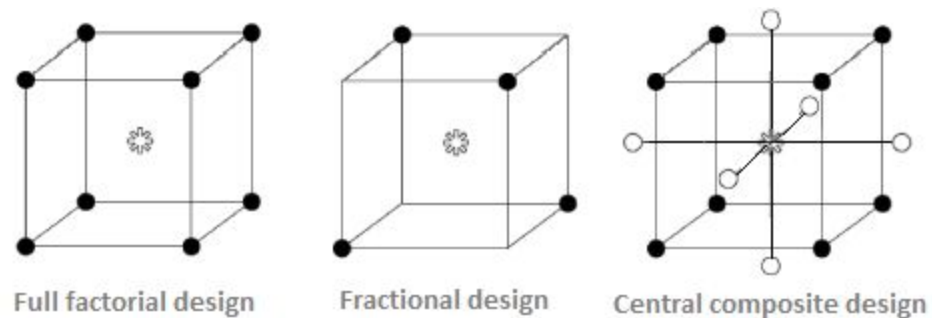


Figure 32: The full factorial, the fractional and the central composite design for an experimental array with three factors on two levels

The Plackett-Burman design is a two-level fractional design for screening factors that have a strong influence on the process and require further investigation. A linear regression model is utilised to find the main effects with impact on the response. The amount of factors is equal to the quantity of experiments minus one [119].

The Taguchi designs are two, three and mixed level full factorial or fractional designs, which were developed for product development and industrial engineering. The aim of the Taguchi design is to identify and reduce the influence of confounding factors on the investigated process. For this purpose, an inner experimental array and outer experimental arrays are developed. The inner array is created with controllable factors and the outer array with possible confounding factors, which can be simulated and controlled on the laboratory scale. The outer arrays are placed around the experiments of the inner array, as shown by Figure 33 [120].

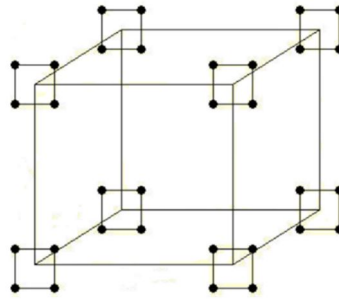


Figure 33: Two level full factorial Taguchi design with three-factor inner array and two-factor outer arrays

## 7.4 The D-optimal design

The optimal designs are experimental designs, which are optimal regarding a statistical criterion. There are many different optimal designs, such as the A-optimal, C-optimal, E-optimal and T-optimal designs. In this project, the D-optimal design is utilised. Information about the other optimal designs can be found in [121].

The D-optimal design is a computer generated design, which selects a group of the best suited experiments of all theoretical possible experiments in order that the experimental effort is reduced and the prediction accuracy is relatively high. The criterion therefore is the maximisation of the determinate of the matrix  $X^T X$  for a given regression model. This is also the reason, why this design is called D-optimal. If the experiments are chosen by this criterion, the volume of the experimental region is maximised, which means, that mainly the levels of the factors with the highest values are combined with each other.

The D-optimal design offers a few advantages in relation to the other designs. Qualitative and quantitative factors can be mixed in a D-optimal experimental array. The quantitative factors do not need to be orthogonal, which allows an irregular design. As a consequence, settings, which are difficult to adjust, can be avoided. Already performed experiments can easily be included in a new experimental array and the required quantity of experiments is lower in comparison to a full factorial or fractional design.

The aim of the D-optimal design is to minimize the experimental effort, but still offer the information about the main effects and simple interactions of the factors on the response. Complex interactions with quadratic terms or more than two factors are in general not considered in the regression model of a D-optimal design. The levels of the factors can freely

be selected, which makes the analysis of complex quadratic and cubic regression models possible. Therefore, the D-optimal design is highly suitable for scientific investigations.

The cubic model for a D-optimal design, which is used in this project, has the following regression model:

$$y = a_0 + \sum_{n=1}^k a_n x_n + \sum_{n=1}^k a_{nn} x_n^2 + \sum_{n=1}^k a_{nnn} x_n^3 + \sum_{n=1}^{k-1} \sum_{m=n+1}^k a_{nm} x_n x_m \quad (21)$$

If three factors are used, Equation 19 yields in:

$$y = a_0 + a_1 x_1 + a_2 x_2 + a_3 x_3 + a_{11} x_1^2 + a_{22} x_2^2 + a_{33} x_3^2 + a_{111} x_1^3 + a_{222} x_2^3 + a_{333} x_3^3 + a_{12} x_1 x_2 + a_{13} x_1 x_3 + a_{23} x_2 x_3 \quad (22)$$

For the estimation of the 13 regression coefficients of the regression model of Equation 22, a full factorial design would need 64 experiments. The D-optimal design reduces the quantity of the required experiments to 16. These two numbers show, why the D-optimal design is favoured for many projects. The experimental effort is minimised while the gained information is mainly maintained. For this project, the statistical software Visual-XSel version 13.0 (CRGRAPH) was used for the generation and the analysis of the D-optimal experimental design.

## 8 Factor analysis for the design of experiment

In this chapter, the different experiments, which were implemented to examine the influence of the possible factors regarding the plasma treatment on each other, are explained. Based on the results of these experiments, it was decided which factors are suitable for the experimental array and which factors must be kept constant, because their variation is inappropriate for the experimental array.

### 8.1 Theoretical reflection of possible factors

In principle, the factors, that influence the surface treatment of the BOPP film with the laboratory scale DBD system, can be divided in two groups. One group of factors concern the settings of the high voltage power supply, the setup and mode of operation was previously discussed in Chapter 5.5. The other group of factors is related to the different electrode configurations and the reel-to-reel system, as explained in Chapters 5.2 and 5.3.

The factors, which can be changed on the reel-to-reel system or the electrode configurations, are the size of the gas gap between the electrodes, the nature of dielectric and its thickness (which covers one or both electrodes), the kind of electrode configuration (flat electrodes or flat and sawtooth electrode) and the rewind speed of the film during the treatment. If a sawtooth electrode is utilised, an additional factor is the number of its teeth.

The factors associated with the power supply are the frequency and the selected voltage function i.e. sinusoidal wave, positive pulse, triangle wave or square wave) and the current setting on the DC power supply. The voltage on the DC power supply is set to the maximum and floats to the specified current. With an increased current setting on the DC power supply, the high voltage power supply feeds more power to the electrode configuration. Adjusting the voltage and setting the current to the maximum is less effective regarding the amplitude of the supplied voltage to the electrodes than the other way around, therefore the current and not the voltage of the DC power supply is chosen as a factor.

All these possible factors have to be investigated to determine whether they are suitable for the experimental array. Therefore, the factors are verified against the following criteria:

The main aim of the experimental array is to examine the different settings, which can also be adjusted on the industrial DBD system. These are the power applied to the electrodes and the gas gap between the electrodes. Thus the most important criterion is that the factors should correspond to one of these two values. That criterion is fulfilled for the current setting

on the DC power supply, and the gas gap, which can be adjusted with washers in steps of 0.5 mm.

The second important criterion is the scientific applicability of the factor investigated. Thus, quantitative factors are preferred in contrast to qualitative factors, because the investigation, of how a qualitative factor influences a process, leads in the best case only to the statement that a certain adjustment leads to better results than the others. The pivotal physical quantity (or quantities) and how these quantities influence the process cannot be identified. If a quantitative factor is utilised, this information can be gained.

Additional to these criteria, the chosen factors must be orthogonal to each other and adjustable over the selected range. The situation where one factor has too much influence on the process should also be avoided, since this could lead to the superposition of the other factors. For the better case, the influence of a factor on the process can no longer be estimated. If a factor is unsuitable for the experimental array, it must be kept constant at a certain value. This value needs to be carefully selected. The following sections will discuss the experiments, which have been undertaken to estimate the suitable factors.

## **8.2 The influence of the set function of the function generator on the voltage applied**

The selected function provided by the function generator is an unsuitable factor for the experimental array, because it has only a qualitative nature. However, the selected function could have an influence on the amplitude of the voltage applied to the electrode configuration. This amplitude should have a preferably high value, since the amplitude of the applied voltage determines the strength of the electrical field between the electrodes. The amplitude of the applied voltage can also be increased by increasing the current setting of the DC power supply. Nevertheless, the power delivered by the DC power supply should not exceed 50 W, because if more power is applied certain components of the amplifier are damaged by overheating.

The influence of the different voltage functions (sinusoidal wave, positive pulse, triangle wave and square wave) on the amplitude of the applied voltage were investigated with the flat electrode configuration with a gas gap of 2 mm filled with air and a frequency of 36 kHz.

A 0.63 mm thick aluminium oxide dielectric covered one electrode and the current on the DC power supply was set to 0.1 A. The results are shown by Figure 34.

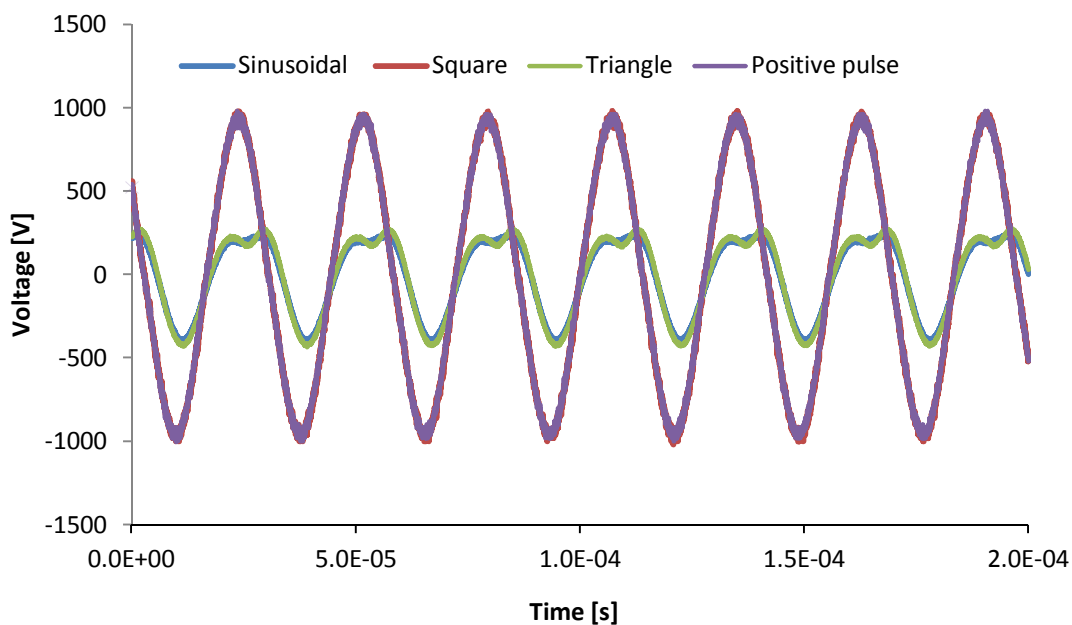


Figure 34: Influence of the set function of the function generator on the voltage applied to the electrode configuration

The results of Figure 34 indicate that the positive pulse and the square wave function (which overlay each other in Figure 34) of the function generator are more suitable than the triangle wave and the sinusoidal wave function (which also overlay each other), because the amplitude of the applied voltage is considerably higher with these settings. The positive pulse and the square wave, as well as the triangle wave and the sinusoidal wave led to the same sinusoidal waveform of the applied voltage. As a consequence of these measurements, the positive pulse was selected as the function for all further experiments.

### 8.3 The influence of the frequency on the electrode voltage

The measurements for the investigation of the influence of the frequency, set on the function generator, on the applied voltage were performed with otherwise identical settings of the experiment of the previous Section 8.2. The frequency was altered over the range of 31 kHz to 45 kHz and the applied voltage was measured every kHz for the functions sinusoidal

wave, square wave, triangle wave and positive pulse. The results of the measurements are shown in Figure 35.

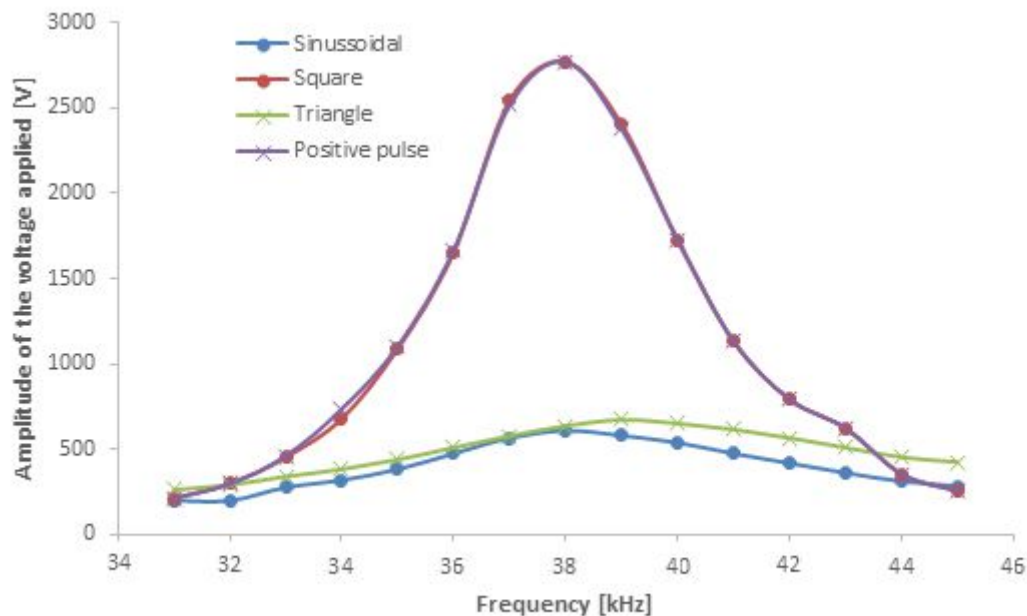


Figure 35: Influence of the frequency on the amplitude of the applied voltage

The results of Figure 35 confirm the findings already made regarding the different waveforms selected on the function generator. The positive pulse and the square wave forms, as well as the triangle and the sinusoidal wave forms led to almost identical amplification of the voltage, whereas the square and positive pulse wave forms offer the better results. The frequency has a strong influence on the amplitude of the voltage. There is an optimum for every wave form between 37 and 39 kHz, where the amplitude of the voltage reaches a maximum. If frequencies lower than 31 kHz are selected, the applied voltage does not have a sinusoidal function, but a pulsed form, which is unsuitable for the ignition of the plasma. Frequencies higher than 45 kHz do not lead to the required amplification of the voltage.

These results show clearly, that the frequency is not suitable as factor in the experimental array. The frequency would be a quantitative factor, however the massive influence on the amplitude of the voltage contains two problems. First of all, the range over which the frequency could be changed, is very small and must be kept close to the optimum, because otherwise the voltage would not be amplified sufficiently to provide the minimum voltage for the breakdown of the gas. Furthermore, the frequency would not be orthogonal to the current setting of the DC power supply. The current is chosen as the factor, which influence

the applied power. Since the frequency has a strong influence on the voltage, it also influences the applied power and is thus not orthogonal to the current setting on the DC power supply.

As a result, since the frequency is unsuitable as a factor, it must be kept constant at a certain value. The most appropriate frequency for this is the optimal frequency, at which the voltage reaches the maximum. However, it must also be investigated whether the optimal frequency, in turn, depends on the electrode configuration settings, such as the size of the gas gap and the type of the dielectric.

#### 8.4 Dependence of the optimal frequency on the capacitance of the electrode configuration and selection of the dielectric

To investigate the change of the optimal frequency by varying the size of the gas gap and the kind of dielectric, three different dielectrics were applied to cover one of the electrodes of the flat electrodes configuration. The optimal frequency was measured for each dielectric at air gaps of 1.0 mm, 1.5 mm, 2.0 mm, 2.5 mm and 3.0 mm. The dielectrics were aluminium oxide with a thickness of 1.26 mm, mica with a thickness of 1.06 mm and polyethylene terephthalate (PET) with a thickness of 1.50 mm. The results are illustrated in Figure 36.

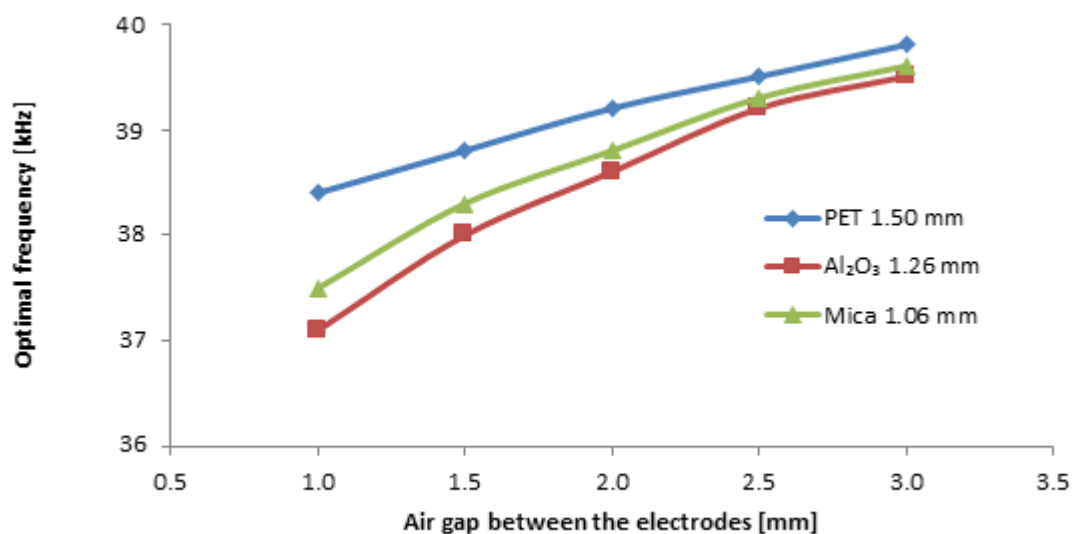


Figure 36: Dependence of the optimal frequency on the air gap distance and the kind of dielectric covering one electrode

The results of Figure 36 show that the kind of dielectric, as well as the size of the air gap have an influence on the optimal frequency. The optimal frequency is increased by enlarging the gas gap. Moreover, the difference in the optimal frequency between the various dielectrics, compared at the same gas gaps, is reduced the larger the gas gap is. This behaviour leads to the assumption that the optimal frequency could be dependent on the capacitance of the electrode configuration, which is the series connection of the capacitance of the gas gap and of the dielectric, as shown by Equation 7. The capacitance of an insulator between two electrodes (the solid dielectric or the gas in the gas gap) depends on the thickness of the insulator,  $d_i$ , the vacuum permittivity,  $\varepsilon$ , the relative permittivity of the insulator,  $\varepsilon_i$ , and the electrode area,  $A_E$ , as expressed by Equation 23.

$$c_i = \varepsilon \cdot \varepsilon_i \cdot \frac{A_E}{d_i} \quad (23)$$

It is evident from Equation 23, that the capacitance of the gas gap is reduced by increasing the size of the gas gap. The capacitance of the dielectric is constant during the experiment, since the thickness of the dielectric is not changed. Thus, the influence of the capacitance of the dielectric on the capacitance of the electrode configuration is reduced with increasing the gas gap, which results in the lowered differences of the measured optimal frequencies of the different dielectrics.

To verify this theory, it was necessary to find the connection between the optimal frequency and the capacitance of the electrode configuration. This connection is given by the resonant circuit, which is formed by the capacitance of the electrode configuration and the inductor (i.e. secondary coil of the transformer). Stryczewska et al. [122] report that the high voltage power supply and the electrode configuration interacts in that way. The optimal frequency is the resonant frequency,  $f_0$ , and is expressed by Equation 24 with the capacitance of the electrode configuration,  $c_{conf}$ , and the inductivity of the inductor,  $L$ :

$$f_0 = \frac{1}{2 \cdot \pi \cdot \sqrt{L \cdot c_{conf}}} \quad (24)$$

It is not possible to directly validate this equation with the measured optimal frequencies, because the varied capacitances of the electrode configuration,  $c_{conf}$ , are unknown and cannot be measured. However, rearranging Equation 24 into the form of Equation 25 allows the product of the inductance and the capacitance of the electrode configuration,  $L \cdot c_{conf}$ , to be expressed as a function of the optimal frequency:

$$f(f_0) = \frac{1}{(2 \cdot \pi \cdot f_0)^2} = L \cdot c_{conf} \quad (25)$$

If the assumption, that the electrode configuration forms an resonant circuit with the secondary coil of the transformer, is true, then the measured optimal frequencies plotted as a function of the calculated product of the inductance and the capacitance of the electrode configuration,  $L \cdot c_{conf}$ , should form a straight line, because the product  $L \cdot c_{conf}$  corresponds to a linear equation with the slope  $L$  and the y-intercept of zero. Figure 37 shows the plot of the optimal frequency against the product of the inductivity and the capacitance of the electrode configuration.

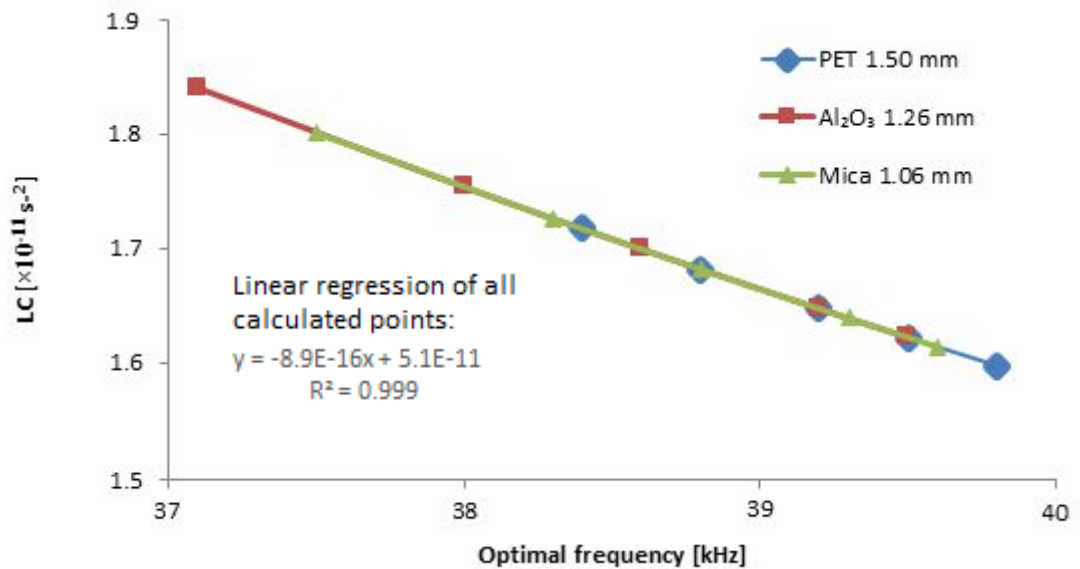


Figure 37: Optimal frequency plotted against the product of inductivity,  $L$ , and the capacitance of the electrode configuration,  $c_{conf}$

Figure 37 indicates that the all points lie, independent on the utilised dielectric or the different sizes of the air gap, on one straight line. The y-intercept of the equation, obtained by

linear regression of all calculated points, has a value of  $5.1 \times 10^{-11}$ , which is almost zero. With this result, it is clear, that the electrode configuration forms a resonant circuit with the inductor of the transformer. Consequently, the optimal frequency depends on the size of the gas gap and the thickness of the used dielectric.

The frequency cannot be used as factor in the experimental array, however the frequency must be set to the optimal frequency for every possible electrode configuration of the experimental array. Only then, is it ensured, that the amplification of the applied voltage is equal and independent of the width of the gas gap and the dielectric material and its thickness.

There are in principle two possible capacitances, i.e. in the case of discharge ignition and in the case that the discharge is not ignited. The optimum frequency will be different in each case. During the discharge, the gas loses its capacitance, because the conductivity of the gas prevents the storage of electrical energy. Therefore, the capacitance of the electrode configuration during discharge depends on the capacitance of the dielectric, the capacitance of the gas gap is not considered. If the discharge is not ignited, the capacitance of the electrode configuration depends on both the capacitance of the dielectric, and on the capacitance of the gas gap.

Experiments to determine of the optimal frequency during the discharge and without the discharge were performed with the result, that the optimal frequency can be more easily estimated, when the discharge is not ignited. The optimal frequency is found by increasing the frequency from 34 kHz to 42 kHz in steps of 0.1 kHz. The desired frequency is the point, where the applied voltage reaches the maximum. The measurement of the applied voltage is disturbed during the discharge by variations of the measured voltage, which do not occur, when the discharge is not ignited. Therefore, the optimal frequency is estimated for the different electrode configurations at a current setting on the DC power supply, which is sufficiently low to avoid discharge.

In addition to the frequency, the three different dielectrics; PET, aluminium oxide and mica, were also investigated in the experiments carried out to examine their serviceability as a dielectric for the electrode configuration. Whereas aluminium oxide and mica appeared as suitable, PET was not able to withstand the high electrical field during the discharge, which led to local arc discharges in the gas gap. Since the different dielectrics were not available in the same thickness, it was decided that the kind of dielectric should not be a factor in the

experimental array, because it would not be possible to correlate the results with the thickness of the dielectric or the material properties. However, it makes sense to choose one kind of dielectric and vary then the thickness of this dielectric.

Meiners et al. [123] investigated the four dielectrics magnesium oxide, aluminium oxide, titanium dioxide and strontium titanate in a DBD with the aim of improving the intensity of the discharge. They concluded that a dielectric with a high ratio of its relative permittivity to its thickness lead to a significant enhancement of the discharge intensity, which was determined by electrical measurements. Another finding of their experiments was that a higher permittivity of the dielectric resulted in an increase of the plasma temperature. Table 7 summarises the relative permittivity and the breakdown strength of magnesium oxide, aluminium oxide, titanium dioxide and strontium titanate.

Table 7: Relative permittivity and breakdown strength of different ceramics [123]

	<b>Relative permittivity</b>	<b>Breakdown strength</b>
	<b>[-]</b>	<b>[kV/mm]</b>
Magnesium oxide	8.1	39
Aluminium oxide	11.5	17
Titanium dioxide	88.0	8
Strontium titanate	300.0	25

Strontium titanate has the highest relative permittivity of all dielectrics in Table 7 and would thus be the best suitable dielectric for the experimental array. Titanium dioxide also has an appropriate relative permittivity, but the low breakdown strength does not fit the criterion of the high electrical fields applied for the DBD. However, aluminium oxide is one of the most widely used dielectrics in the literature [34, 57, 58, 124-128], whereas strontium titanate is rarely used. Thus, it was decided to use an aluminium oxide dielectric in order to provide better comparison of the data obtained in this study with those of other researchers.

Five sheets of aluminium oxide with the dimensions  $54 \text{ mm} \times 34 \text{ mm} \times 0.63 \text{ mm}$  were bought from the company Crystal GmbH. The thickness of the dielectric can be changed by clamping various numbers of aluminium oxide sheets on the electrodes. The thickness can be thus modified in steps of 0.63 mm.

### 8.4.1 The rewind speed of the film during the treatment

The last possible factor is the rewind speed of the BOPP film during the plasma treatment. The speed depends on the voltage applied to the DC motor, which drives the rewind reel of the reel-to-reel system. Moreover, it must be investigated, whether the size of the gas gap has an influence on the rewind speed. The change of the size of the gas gap leads to a slightly different pathway of the BOPP film, which could alter the rewind speed at constant voltage applied to the DC motor.

The following experiments were carried out with the two gas gaps of 0.5 mm and 2.5 mm. The voltage applied to the DC-motor was varied from 10.5 V to 13.0 V in 0.5 V steps. A 30 cm long BOPP sample was attached to the reel-to-reel system. One sheet of aluminium oxide dielectric covered the upper electrode. The time taken to rewind the film was measured by a stop watch. The measurement were performed ten times for every voltage step. The results (Figure 38) are the average value of ten measurements. The error indicated is the standard deviation.

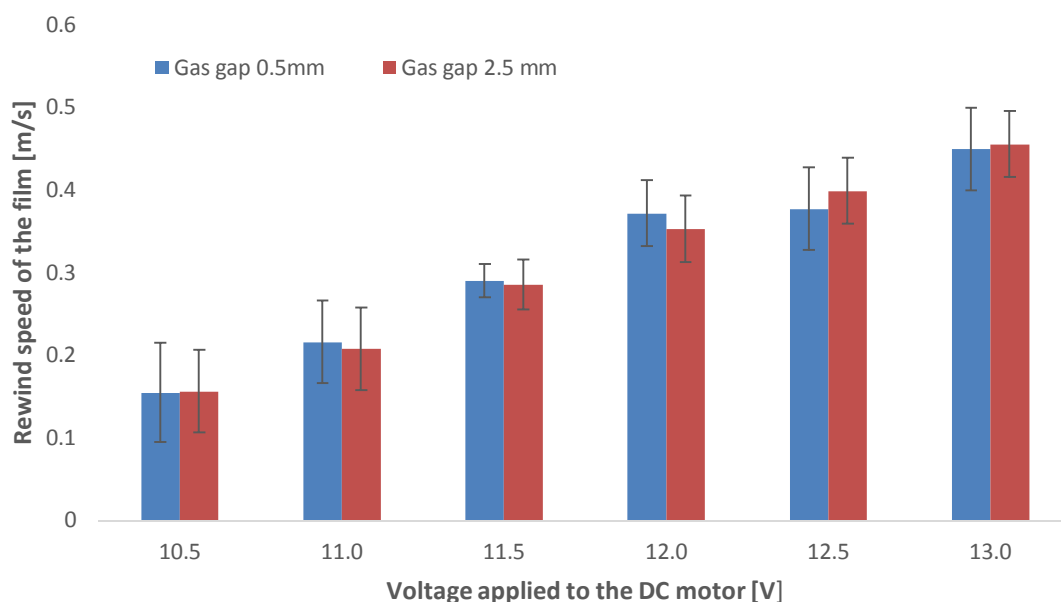


Figure 38: Measurement of the rewind speed of the film with different sizes of the gas gap and varies voltages applied to the DC motor

The results clearly indicate that the rewind speed is increased with higher voltages applied to the DC motor. There is no significant difference of the rewind speed between the two gas gaps. Therefore, it is assumed, that the size of the gas gap has no influence on the rewind

speed. The indicated error turns out to be relatively high. This has two main reasons. At lower voltages of 10.5 V and 11.0 V, the film is only erratically transported through the gas gap, because the torque of the DC motor is too weak to effectively overcome the friction between the film and the dielectric. As consequence, the necessary time of the film to be rewound strongly varies.

At higher voltages of 11.5 V, 12.0 V, 12.5 V and 13.0 V, the BOPP film is transported at a constant speed without interruptions. However, the necessary time to rewind the film becomes lower than 0.7 s for the voltages of 12.5 V and 13.0 V. These short times intervals are difficult to measure accurately with a stop watch ( $\pm 0.2$  s), thus the quality of the measurements is rather low. Increasing rewind time using a longer BOPP sample is not possible, because the limited space between the DC motor and the rewind reel does not allow a longer film to be rewound.

Based on these results, it was decided to not use the rewind speed of the BOPP film as factor in the experimental array. Reliable measurement of the rewind speed is only possible between applied voltages of 11 V and 12 V. This range is too low to provide a sufficiently large variation of the rewind speed, therefore the voltage applied to the DC motor was kept constant at 12 V, which translates to a rewind speed of  $0.37 \pm 0.03$  m/s.

In conclusion, the following three factors were chosen for the experimental array:

- the thickness of the dielectric
- the size of the gas gap
- the current setting of the DC power supply

The other factors, which are the frequency of the applied voltage, the function of the function generator, the type of dielectric and the rewind speed of the BOPP film will be kept constant at suitable values. A separate experimental array will be developed for the two different electrode configurations.

## **8.5 The response of the experimental array and the principle surface treatment analysis process**

The aim of the experimental array is to investigate the influence of the three chosen factors on the surface energy of the BOPP film after the plasma treatment. The surface energy can

be calculated, if the contact angles of three different test liquids with the treated BOPP film are determined. But, it is reported, that the plasma treatment only increases the polar part of the surface energy, while the dispersive part stays mainly unaffected [129, 130]. Thus, it is sufficient to measure only the contact angle of one polar liquid, in order that the change of the polar part of the surface energy can be comprehended. Therefore, distilled water was chosen as the test liquid and the contact angle between the water drop and the surface of the treated BOPP film is the response of the experimental array.

The experimental procedure is as follows. A 30 cm long and 3 cm wide BOPP sample is fixed to the reel-to-reel system with Sellotape. The untreated side of the BOPP film faces the gas gap and the whole film is coiled on the unwind reel. The reel-to-reel system is then placed on its bracket inside of the plasma chamber, which is sealed afterwards with the end cap. The rotary pump is used to reduce the pressure inside the chamber to a minimum of 1300 Pa. When this pressure is reached, the nitrogen gas valve is opened. The rotary pump continues to run on for 2 minutes more to flush the chamber, in order that the remaining air is removed. The pressure inside the chamber is set to a slight overpressure of 1.05 bar, which prevents the surrounding air entering the chamber.

The frequency set on the function generator is adjusted to 20 kHz. At this low frequency, the amplification of the voltage applied to the electrode configuration is very low. Therefore, the adjustment to the desired setting of the current at the DC power supply for the high voltage power supply can be made without igniting the plasma. The shifting to the optimal frequency and thus the ignition of the plasma is performed simultaneously with the activation of the DC power supply, which is connected to the DC motor of the electrode configuration. The commencement of the rewinding of the BOPP film is thus coincident with plasma ignition.

After the plasma treatment, the vacuum chamber is opened and the BOPP film is removed from the reel-to-reel system. Ten drops of distilled water are placed in the middle on the treated surface of the BOPP film at a distance of approximately 1 cm from each other and the contact angles of these drops are measured. The average of the ten contact angles is the response of the experimental array. The first distilled water drop is placed 7 cm away from the end, which was fixed at the rewind reel. This is necessary, because this part did not pass the plasma and is therefore not surface treated. The remaining space above and below the contact angles can be used for the analysis with Dyne Inks and Pens. Figure 39 illustrates a typical sample investigated with contact angles and Dyne Inks and Pens.

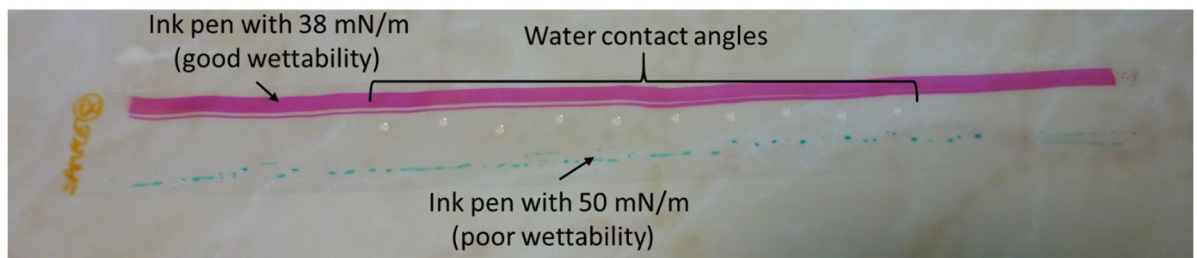


Figure 39: Investigation of a treated sample with contact angle and Dyne Inks and Pens

The relatively high amount of contact angle measurements were made, because the rewind speed of the BOPP film is not constant. The reason for this is, that the circumference of the rewind reel grows the more the film is rewound as already discussed in Chapter 5.2. Additionally, the plasma has more effect on amorphous regions than on crystalline regions of the BOPP film through a stronger etching (discussed in Chapter 1.1). It cannot be assumed that the amorphous and crystalline parts are regularly distributed. Variations in the measurements, which results from these two effects, can be reduced by measuring several contact angles and summarising them in one average value. This average value represents the surface abilities of the sample better than a single contact angle measurement.

## **9 The experiment of the laboratory scale DBD system**

The experimental arrays and their results are discussed in this chapter for the flat electrode and the three different sawtooth electrode configurations. The influence of the thickness of the dielectric, the size of the gas gap and the current settings are represented, whereby the differences between the effects on the substrate of the plasma treatments with the varying electrode configurations is worked out.

### **9.1 The design of experiments for the flat electrode configuration**

Flat electrodes are often used in scientific laboratories, because it is possible to ignite homogeneous discharges with them at atmospheric pressure. The reason is that the electrical field between flat electrodes is homogeneous. In contrast, electrical fields between a flat and a sawtooth electrode is not uniform. A homogenous field is a basic requirement for the ignition of a homogeneous plasma at atmospheric pressure. However, a Townsend discharge was not successfully ignited in nitrogen during this project. The main problem seems to be the high voltage power supply, which is only able to effectively amplify the voltage close to the optimal frequency. This optimal frequency was always higher than the maximum allowed frequency of 10 kHz (see Table 4). Therefore, the ignited plasma was always filamentary.

The flat electrode system, presented in this thesis, is the third version developed in this PhD-project. The main problem was to find a suitable size of the electrode area. If the electrode area is selected too large, the filaments of the filamentary discharge are ignited too far away from each other, which results in a non-uniform treatment of the BOPP film. The resulting contact angles made with these films are not reproducible. Therefore, the electrode size was reduced to the utilised and discussed here.

When two flat electrodes are utilised in the electrode configuration, both electrodes can be covered by the aluminium oxide dielectric. It is also possible to leave one electrode bare and only cover the other electrode. However, the contact angles of samples, treated with an electrode configuration, where only one electrode was covered by the dielectric, could not be reproduced.

One possible explanation is, that the edge effect, which is responsible for a higher electrical field at edges and tips, causes the ignition of more filaments at the border of the electrodes than in the middle of the plasma zone, when only one electrode is covered by the dielectric.

This effect could lead to an inhomogeneous treatment of the BOPP films, because the filaments of the plasma are not uniformly distributed over the electrode area. These edge effects are reduced, when both electrodes are covered with the dielectric. The reduction of the edge effect is greater with the thicker of the dielectrics [54]. Furthermore, a memory effect is established, when both electrodes are covered. This memory effect ensures that ignition of the filaments always occurs at the same position (as discussed in Chapter 4.2.1) resulting in further stabilisation of a more uniform distribution of the filaments.

As a result, since the contact angles of the samples treated by the electrode configuration with one bare electrode were not reproducible, both electrodes were covered with the aluminium oxide dielectric. The variation of the thickness of the dielectric was implemented by changing the number of aluminium oxide sheets on the upper electrode between one and three sheets, which corresponds to thicknesses between 0.63 mm, 1.26 mm and 1.89 mm. The lower electrode was always covered with one sheet of aluminium oxide for all experiments of this experimental array.

The settings of the second factor, the size of the gas gap, were selected as 1.5 mm, 2.0 mm and 2.5 mm. These settings are realised by placing the required amount of 0.5 mm thick washers on the threaded bars of the electrode configuration (see Figure 19). Smaller gas gaps than 1.5 mm were unsuitable, because it was found that the samples were mainly treated on the backside, while the side which was facing the gas gap was almost not affected by the plasma.

The current delivered by the DC power supply was varied between 0.5A and 0.9A in 0.2 A steps. The upper current limit is chosen so that the output the power applied from the DC power supply does not damage the amplifier. The lower limit was selected in order that enough filaments are ignited and the resulting plasma looks uniform with the consequence that the measured contact angles are well reproducible.

Thus, the factors are varied on three levels (-1, 0, +1) for the experimental design, which allows the regression coefficients of a quadratic model by the D-optimal design to be estimated. The main problem, which limited the range of the levels, was the relatively high minimum value of the gas gap. The gas gap, as well as the thickness of the dielectric have an influence on the power delivered from the DC power supply to the amplifier. This power is increased with increased gas gap and increased thickness of the dielectric, and the maximum applicable power of 50 W was reached at the maximum settings of the gas gap of 2.5

mm and 1.89 mm, respectively for the dielectric thickness. The D-optimal experimental design for the flat electrode configuration was created with the computer program Visual-XSel. All array settings and the estimated optimal frequency for the different electrode configurations are listed in Table 8. Every experiment was repeated twice to provide a good estimation of the statistical error.

Table 8: Experimental design for the flat electrode configuration with the optimal frequency at which the experiments were performed

<b>Number of experiment</b>	<b>Current [A]</b>	<b>Thickness of the dielectric [mm]</b>	<b>Size of the gas gap [mm]</b>	<b>Optimal frequency [kHz]</b>
1	0.7	0.63	2.0	30.7
2	0.5	1.26	1.5	30.7
3	0.7	1.89	2.5	30.8
4	0.5	1.89	2.5	30.8
5	0.5	1.89	2.0	30.7
6	0.9	1.26	2.0	30.7
7	0.9	0.63	1.5	30.7
8	0.9	1.89	2.5	30.8
9	0.7	1.89	1.5	30.6
10	0.9	1.89	1.5	30.6
11	0.5	1.89	1.5	30.6
12	0.5	0.63	1.5	30.5
13	0.9	0.63	2.5	30.8
14	0.5	0.63	2.5	30.8
15	0.7	1.26	2.0	30.7

The water contact angle results from the experimental array for the flat electrode configuration are illustrated in Figure 40 as a function of the current set on the DC power supply, in

Figure 41 as a function of the thickness of the dielectric and in Figure 42 as a function of the size of the gas gap. These figures show the influence of the three different factors on the measured water contact angle with the calculated confidence interval, which has a confidence level of 95%. The coefficient of determination,  $R^2$ , amounts to 0.856. Thus, the calculated regression coefficients describe the measured water contact angles with reasonable accuracy, because the coefficient of determination is relatively close to 1.

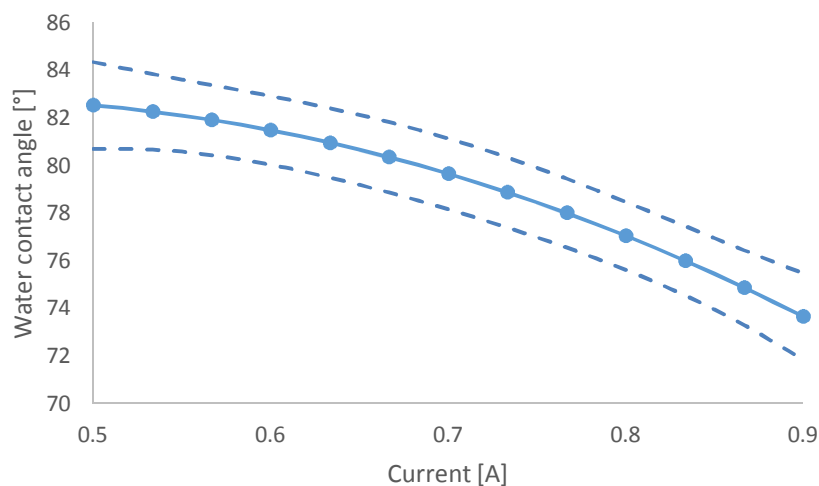


Figure 40: Influence of the current on the water contact angle for the flat electrode configuration

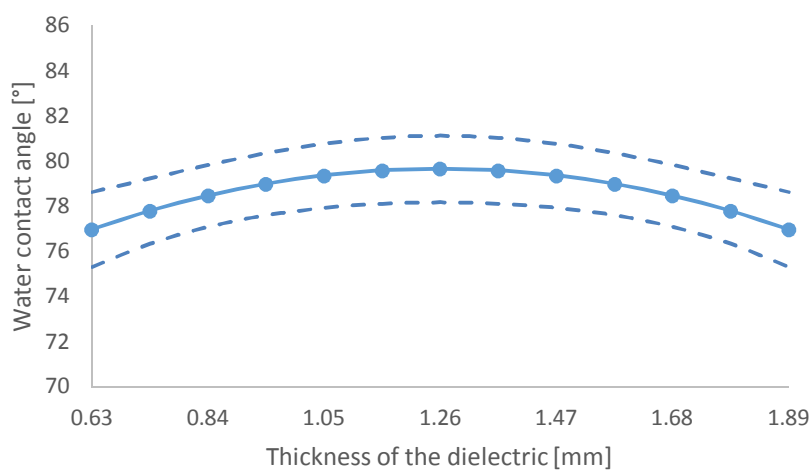


Figure 41: Influence of the dielectric thickness on the water contact angle for the flat electrode configuration

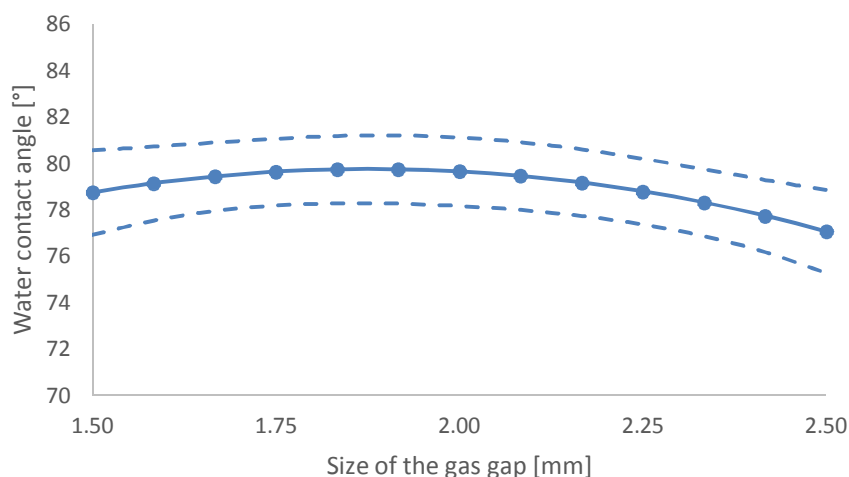


Figure 42: Influence of the gas gap size on the water contact angel for the flat electrode configuration

The results (Figure 40) identify, that the water contact angle is lowered with an increased current setting, which means simultaneously, that the wettability of the treated film to polar substances is increased. The influence of the dielectric thickness in Figure 41 cannot clearly be identified. The function has a weakly marked maximum at a thickness of 1.26 mm, but the relatively large confidence interval shows, that this maximum is not significant. Thus, it is not possible to identify the optimal settings, which would be the lowest or the highest adjusted value of the dielectric thickness, 0.63 mm and 1.89 mm. The same is true for the influence of the gas gap size in Figure 42. Also this function shows a weakly marked maximum, which is not significant. It is not possible to find an optimal value in the results of Figure 42.

The water contact angle of the untreated BOPP film was to  $103^\circ (\pm 1^\circ)$ . After the plasma treatment, the contact angle is reduced to values between  $70^\circ$  and  $82^\circ$  depending on the different settings of the experimental array. The main influence thereby was the current setting on the DC power supply. The higher the current is adjusted on the DC power supply, the lower is the water contact angle of the treated BOPP sample. The influences of the dielectric thickness and of the gas gap size on the water contact angle is much lower and it is not possible to clearly identify, which settings are optimal for the surface treatment, by considering only the main influences of the factors. Figure 43 and Figure 44 compare the simultaneous influence of the dielectric thickness and of the gas gap size with the current setting and show thereby also correlations between the two depicted factors.

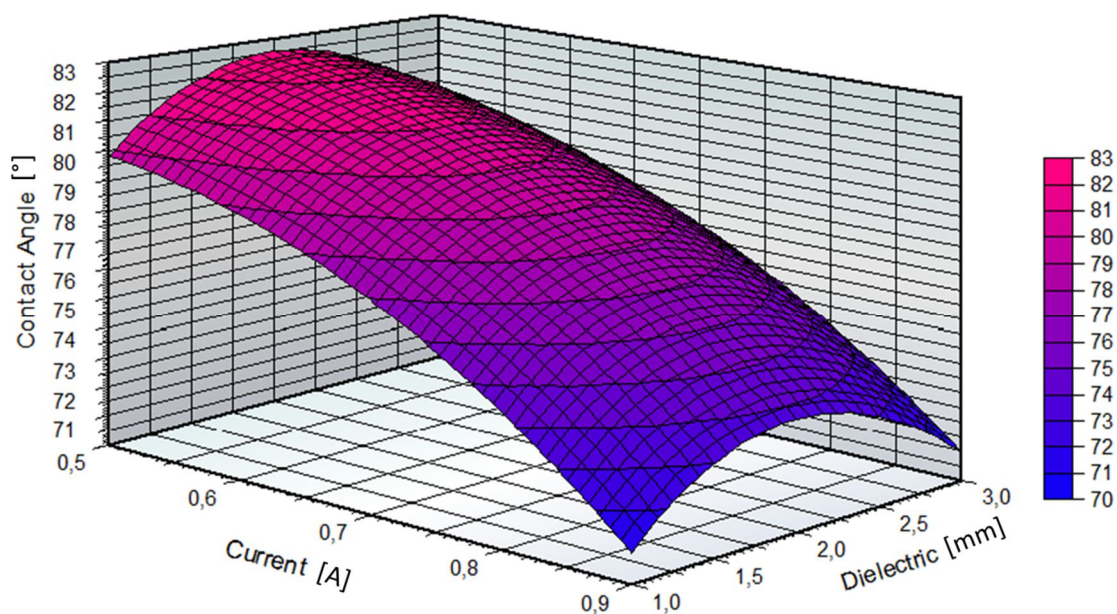


Figure 43: Influence of the current set on the DC power supply and the thickness of the dielectric on the water contact angle of the treated BOPP samples calculated for a constant gas gap of 2.0 mm.

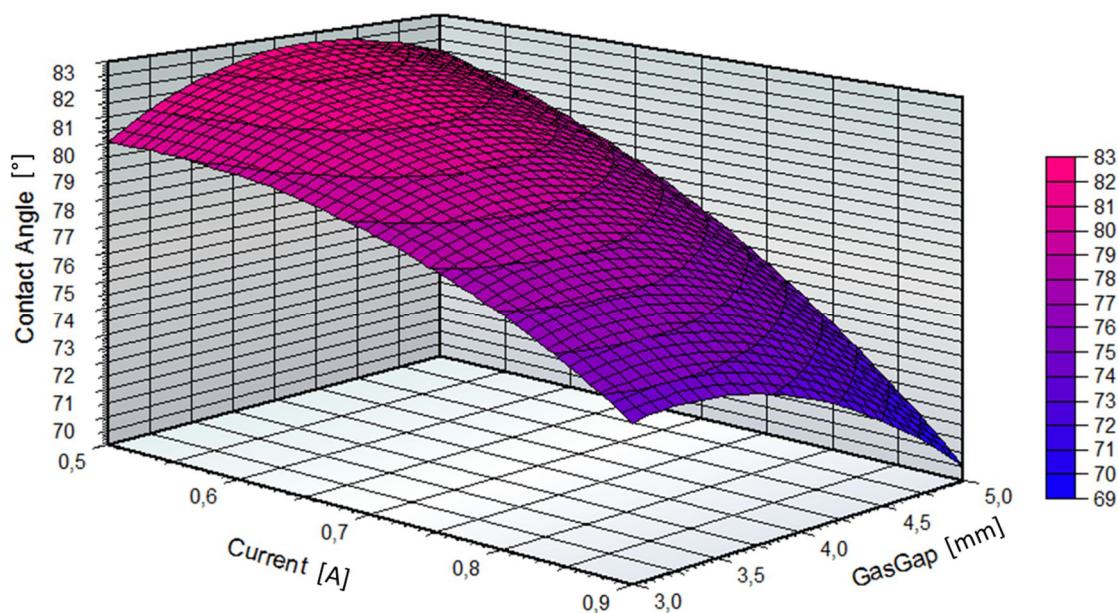


Figure 44: Influence of the current set on the DC power supply and the size of the gas gap on the water contact angle of the treated BOPP samples calculated for a constant dielectric thickness of 1.26 mm.

The influence of the dielectric thickness in Figure 43 does not show significant correlations with the current and is obviously has a much lower effect than the current. In Figure 44, the influence of the gas gap size and the current is illustrated. It is recognisable, that there are

correlations between the gas gap size and the current setting, which lead to a further reduction of the water contact angle at high current settings and increased gas gaps. However, it is not possible to estimate whether the correlation is significantly larger than the statistical error.

## **9.2 The design of experiments for the sawtooth electrode configurations**

The sawtooth electrode configurations are utilised in industrial DBD systems and are not often studied on the laboratory scale. Three different sawtooth configurations were examined in this PhD-project. They differ themselves in the amount of teeth (1, 3 and 5) as shown in Figure 22. The aim of this investigation was to study, how the distribution of the filaments on top of the sawtooth electrodes influences the surface treatment of the BOPP film, when the discharges are concentrated on one, three or five discharge lines.

In contrast to the flat electrode configuration, the treatment of the BOPP films with the sawtooth electrodes was already successful, in contrast to the flat electrode configuration, at the lowest possible size of the gas gap of 0.5 mm. Therefore, the settings of the factors were varied at four levels (-2, -1, +1, +2), which allows the regression factors of a cubic model to be determined. The settings of the gas gap were 0.5 mm, 1.0 mm, 1.5 mm and 2.0 mm. The current of the DC power supply was varied between 0.8 A and 1.4 A in 0.2 A steps. Only the upper flat electrode was covered by the aluminium oxide dielectric; the sawtooth electrode stayed bare for all experiments. The thickness of the dielectric was varied between 0.63 mm, 1.26 mm, 1.89 mm and 2.52 mm. The confidence interval was also calculated for a confidence level of 95%. The complete design of experiments, which was applied for the three different sawtooth electrode configurations, is shown in Table 9. The utilised optimal frequencies are listed in Table 10.

Table 9: Design of experiment for the sawtooth electrode configurations

<b>Number of experiment</b>	<b>Current [A]</b>	<b>Thickness of the dielectric [mm]</b>	<b>Size of the gas gap [mm]</b>
1	0.8	0.63	2.0
2	1.4	0.63	0.5
3	1.2	1.26	0.5
4	1.2	0.63	2.0
5	0.8	0.63	0.5
6	1.0	1.89	2.0
7	0.8	2.52	2.0
8	0.8	1.89	1.5
9	1.0	0.63	1.5
10	0.8	1.26	0.5
11	0.8	1.89	1.0
12	0.8	0.63	1.0
13	0.8	1.26	2.0
14	1.2	1.26	2.0
15	1.2	0.63	0.5
16	0.8	2.52	0.5

Table 10: The optimal frequencies used for the different sawtooth electrode configurations

<b>Number of experiment</b>	<b>Optimal frequency (1 tooth) [kHz]</b>	<b>Optimal frequency (3 teeth) [kHz]</b>	<b>Optimal frequency (5 teeth) [kHz]</b>
1	30.4	29.8	29.6
2	30.3	29.6	29.0
3	30.3	29.6	29.0
4	30.4	29.8	29.6
5	30.3	29.6	29.0
6	30.4	29.9	29.7
7	30.4	29.9	29.7
8	30.3	29.9	29.5
9	30.3	29.8	29.5
10	30.3	29.6	29.0
11	30.3	29.7	29.4
12	30.3	29.6	29.4
13	30.4	29.9	29.7
14	30.4	29.9	29.7
15	30.3	29.6	29.0
16	30.3	29.7	29.1

The optimal frequencies in Table 10 differ for each different sawtooth electrode configurations. This is due to the diverse electrode areas, which increased with the amount of teeth in the sawtooth electrodes. The increase of the electrode area leads to an increase of the capacitance of the electrode configuration (shown by Equation 23) and thus to the reduction of the optimal frequency (shown by Equation 24). As a result, the electrode configuration with five teeth has the lowest optimal frequency and the electrode configuration with one tooth has the highest, for all the different settings of the experimental array.

The results of the multiple regression for the experimental array of the sawtooth electrode configurations are illustrated in Figure 45 as a function of the current and in Figure 46 for the size of the gas gap. The results for the thickness of the dielectric are not included, because there was no influence of this parameter on the measured water contact angles.

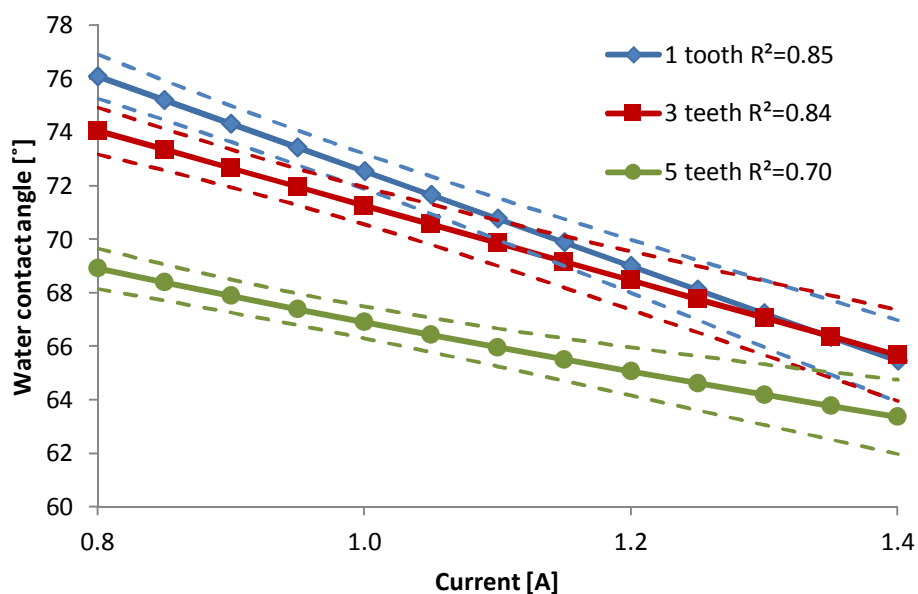


Figure 45: Influence of the current on the water contact angle for the sawtooth electrode configurations

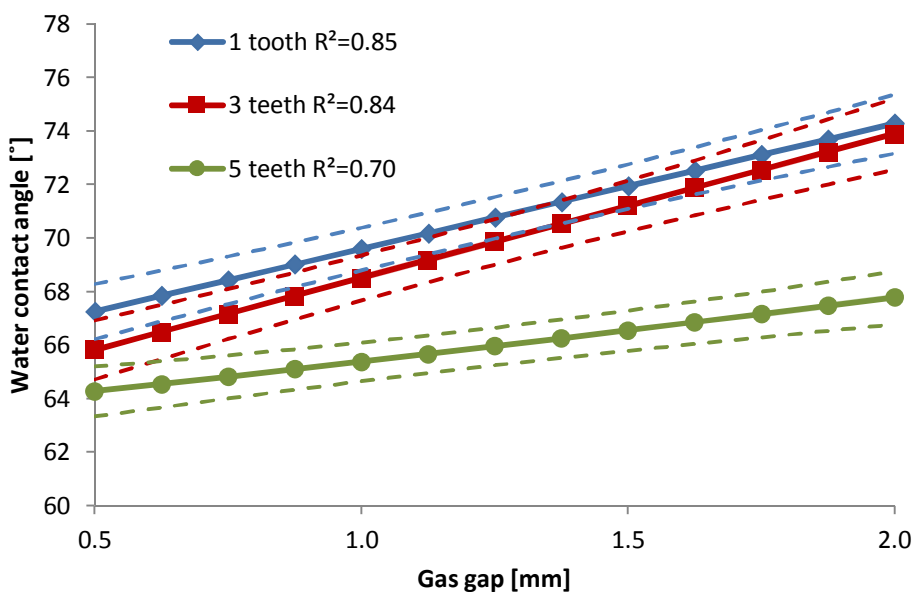


Figure 46: Influence of the gas gap size on the water contact angle for the sawtooth electrode configurations

Figure 45 and Figure 46 clearly indicate that the relationship between the contact angles on the BOPP films and the gas gap and the current set on the DC power supply, are linear. Increased current setting leads to a reduction of the measured water contact angles, whereas an increase of the gas gap size results in the measurement of higher contact angles. The thickness of the dielectric has no influence and there are no correlations between the factors. The linear relationships are exceptional, because the utilised cubic model contains also quadratic and cubic terms. However, the regression coefficients of these quadratic and cubic terms have been classified as not significant for all three sawtooth electrode configurations. The confidence interval of the sawtooth electrode configuration with one tooth and three teeth overlap completely in Figure 46 and mainly in Figure 45, which means that the results of these two experimental arrays are identical or very similar. The experimental array with the sawtooth electrode with five teeth shows much lower measured contact angles, which leads at the first glance to the statement, that the sawtooth electrode configuration with five teeth is more suitable than the other investigated sawtooth electrodes. However, the coefficient of determination,  $R^2$ , for the experimental array of the sawtooth electrode with five teeth has at 0.70 a much lower value than the other experimental arrays, which reach 0.84 for the electrode configuration with three teeth and 0.85 for the electrode configuration with one tooth.

In addition to the lower coefficient of determination, it was also observed, that some samples from the experimental array with the five tooth sawtooth electrode had in parts a low wettability to the test ink with the surface energy of 38 mN/m. This is very unusual, since all other samples treated with the plasma showed a very good wettability to this ink. A typical sample with a partly low wettability to the test ink with the surface energy of 38 mN/m is shown in Figure 47.

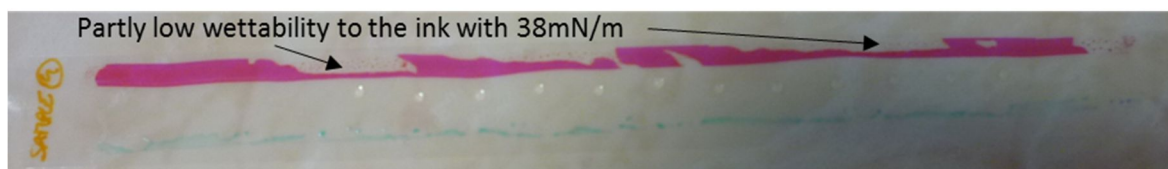


Figure 47: Sample of experiment 4 treated with the 5 tooth sawtooth electrode configuration

The samples revealing this problem were treated with the settings of the experiments 1, 4 and 13. These experiments share the maximum setting for the gas gap size of 2.0 mm and a

relatively low dielectric thickness of 0.63 mm or 1.26 mm. The treated films of the repeats showed similar problems with the wettability to the test ink.

The problem is to explain, why the water contact angles at the middle of these samples have relatively low values, but on the other side the borders of the same BOPP films show a weak wettability to the used test ink. Especially, since all other samples, including those with higher measured water contact angles, do not have any wettability problems to the identical test ink.

One possible explanation for this phenomena is, that the distribution of the filaments for the sawtooth electrode configuration with five teeth is not uniform under special conditions, which leads to a more intensive treatment in the middle of the sample, while the borders are less affected by the plasma.

This theory is supported by the fact that the wettability problems occurred in the experiments with a low dielectric thickness and a large gas gap. With increasing the gas gap, the amount of ignited filaments is reduced. In order that a lower amount of filaments lead to the uniform treatment of the BOPP film, their distribution and reignition must be equal over the electrode surface. This requires a relatively homogeneous electrical field, which does not seem to be provided, when the flat electrode is only covered by one or two sheet of the aluminium oxide dielectric. That an increased dielectric thickness homogenises the electrical field and entails a more uniform treatment is implied by the samples of experiment 6 and 7. These experiments were carried out also at a gas gap of 2.0mm, but with an increased dielectric thicknesses of 1.89 mm and 2.52mm. The treated BOPP films of these experiments show a good wettability to the test ink, as shown by Figure 48 and Figure 49.



Figure 48: Sample of experiment 6 treated with the 5 tooth sawtooth electrode configuration



Figure 49: Sample of experiment 7 treated with the 5 tooth sawtooth electrode configuration

In addition to the size of the gas gap and the thickness of the dielectric, the current also had an influence on the wettability of the surface following the treatment. As already discussed, the sample treated with the settings of experiment 13 showed in part a poor wettability to the test ink over certain regions. The sample of experiment 14 had no wettability problems. The settings of these two experiments differ themselves only in the current setting, which was at 1.2 A much higher for experiment 14 than for the experiment 13 at 0.8 A. However, it is not possible to conclude from this alone, that the surface treatment is more homogeneous with increased current settings.

The amount of ignited filaments is increased with a higher current setting, however the statement, that the distribution of the filaments is more uniform, because the treated films have a good wettability to test ink, is not correct. The reason is, that the surface energy is in general more increased at higher current settings, because more power is applied to the electrode configuration. This could lead to the result, that the treated BOPP films still have an inhomogeneous treatment, however the less well-treated areas cannot be identified with the test ink, because these areas have already a surface energy above 38mN/m. Thereby, all samples of the experiments with a gas gap of 2.0 mm and a dielectric thickness of 0.63 mm or 1.26 mm, treated by the sawtooth electrode configuration with five teeth, must be considered as not uniformly treated. The other samples within this experimental array probably received a uniform treatment.

The measured water contact angles do not represent the surface properties of the unequally treated samples, because they were measured only in the middle, where the plasma was more intense than at the borders of the sample. Therefore, the measured contact angles are lower than they would be, if the filaments had been distributed more uniformly. This could be the explanation, why the factors of the experimental array of the sawtooth electrode with five teeth showed so much lower water contact angles than the experimental array with one or three teeth. Furthermore, the fact, that some measured contact angles do not entirely represent the surface properties of the investigated sample, could be the reason, why the coefficient of determination is reduced for the experimental array of the sawtooth electrode with five teeth in comparison to the other experimental arrays.

To be able to explain the measured water contact angles of the unequally treated samples of the sawtooth electrode with five teeth at higher gas gaps of 2.0 mm, photos of the plasmas were taken at the different settings of experiment 1 and 4 with and without the inclusion of BOPP film.

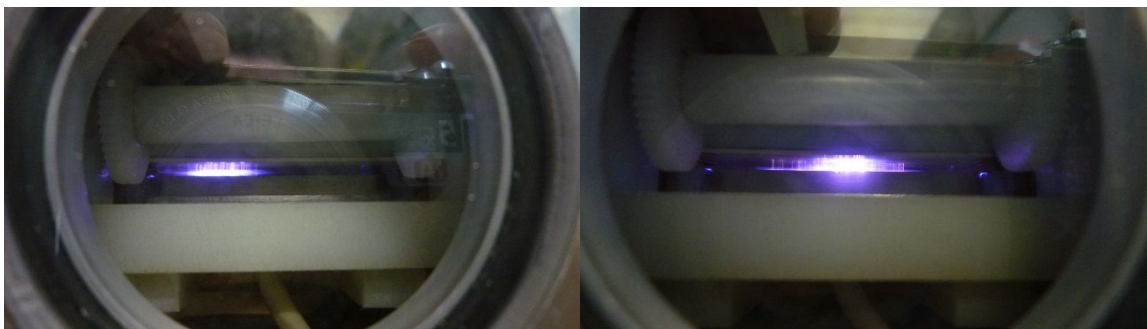


Figure 50: Plasmas of experiment 1 (left) and 4 (right) without applied BOPP film (five teeth electrode)

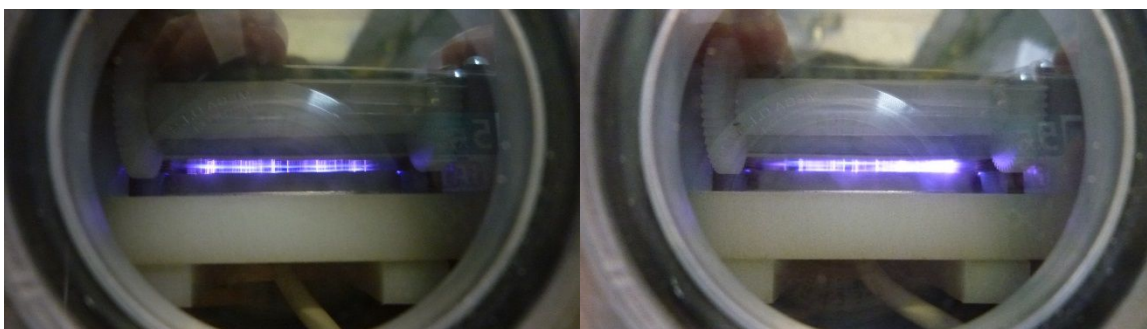


Figure 51: Plasmas of experiment 1 (left) and 4 (right) with applied BOPP film (five teeth electrode)

The plasmas without applied BOPP in Figure 50 are not well distributed over the electrode surface and are reignited mainly in the same limited areas. With the BOPP film present, the plasma is better distributed and evenly spread over the BOPP film. Therefore, it can be deduced, that the BOPP film stabilises the electrical field with its dielectric properties. It is well conceivable, that the stabilisation is greater in the middle of the BOPP sample than at the borders, which could lead to the more frequent ignition of filaments in the middle. This would increase the intensity of the plasma in this region and thereby also the surface treatment of the BOPP film. This would explain the relatively low measured water contact angles in the middle and the less treated areas at the borders of the non-uniformly treated BOPP samples.

If the gas gap is reduced to lower values, there are no problems with the distribution of the filaments, independent on the thickness of the dielectric, as shown by the photo of the plasma with the settings of experiment 9 in Figure 52. Additionally, also the amount of ignited filaments is increased, when the size of the gas gap is reduced. At the minimum gap of 0.5 mm the filaments overlap, so that the plasma looks like one bright light. The individual filaments cannot be identified anymore, as presented in the photo of the plasma with the settings of experiment 5 in Figure 52.

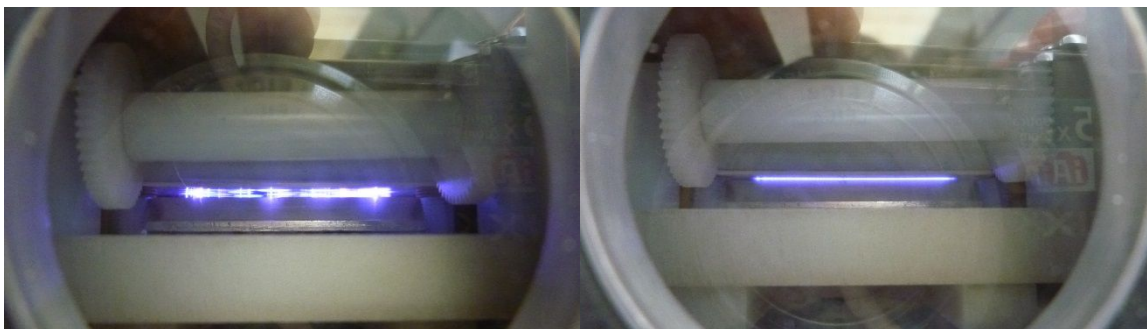


Figure 52: Plasmas of experiment 9 (left) and 5 (right) without applied BOPP film (five teeth electrode)

These investigations lead to the conclusion, that the optimal settings for the sawtooth configurations are relatively narrow gas gap and a high current. A high current setting ensures, that the high voltage power supply applies more power to the electrode configuration, which increases the intensity of the plasma and thus the surface treatment. With the reduction of the gas gap size, the strength of the electrical field between the electrodes is increased, provided, that the applied voltage is constant (compare Equation 4). A higher electrical field strength also increases the intensity of the plasma. The thickness of the dielectric has no influence on the wettability of the treated BOPP films. However, a certain thickness of dielectric is necessary to provide a homogeneous distribution of the filaments, especially at higher gas gaps.

It is difficult to make a distinct statement about the results of the surface treatment with the different sawtooth electrodes. The experimental array with the one and the three tooth sawtooth electrode led to the almost identical results. The measured water contact angles of the experimental array with the five tooth electrode were significantly lower than with other two sawtooth electrodes. However, it could be determined, that not all samples of the experimental array with the five teeth electrode were uniformly treated and the contact angles were measured at a position, where plasma was more intense. Therefore, the results of the experimental array with the five tooth electrode are distorted and cannot be directly compared with the results of the other two sawtooth electrodes.

Based on these results, the influence of the amount of teeth on the wettability on the treated BOPP samples is assessed as minor. It is estimated, that the amount of teeth and thus the area, where the discharge is ignited, must be adapted to the amount of ignited filaments, which depends on the size of the gas gap and the applied power to the electrodes. If the area is too large for the amount of filaments, the surface treatment can be inhomogeneous, especially if the thickness of the dielectric is not sufficient to provide a uniform distribution of

filaments. If the area selected is too low, discharges can occur outside of the electrode area. An example for this is shown by Figure 53, where an arc discharge is ignited at both ends of the electrode bypassing the dielectric. The sawtooth electrode with one tooth was utilised for this experiment. The other settings are the thickness of the dielectric at 2.52 mm, the size of the gas gap at 0.5 mm and the current at 1.4 A.

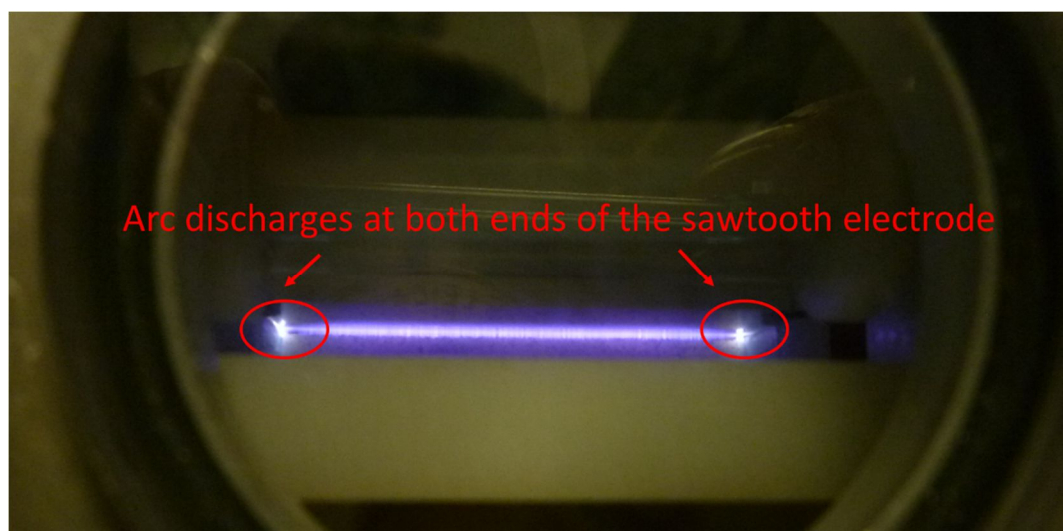


Figure 53: Arc discharges ignited at both ends of the sawtooth electrode with one tooth, bypassing the dielectric

### 9.3 Comparison of the two electrode configurations

The surface treatment in a nitrogen atmosphere with the flat electrode configuration, as well as with the sawtooth electrode configurations, considerably enhances the wettability of the treated BOPP films to polar substances. However, the increase of the wettability and the influence of the studied factors varies depending on the electrode configuration utilised.

The treatment with the sawtooth electrode configurations is superior in terms of the increase of the wettability in comparison to the treatment with the flat electrodes. The treatment with the flat electrode configuration is only appropriate, if the size of the gas gap is larger or equal to 1.5 mm, because narrower gas gaps lead to the treatment of the backside of the BOPP film. This problem does not exist, if a sawtooth electrode is utilised and much lower gas gaps can be adjusted for this type of electrode configuration.

A further difference between the two types of electrode pairs is the influence of the investigated factors in the experimental array. An increase of the current setting leads, for both electrode configurations, to lower measured water contact angles and, hence increased wettability. Also the thickness of the dielectric seems to have no influence (or is of minor relevance) in both cases. However, the size of the gas gap has a different impact on the water contact angles that is dependent on the electrode configuration utilised. If a sawtooth electrode is used, the wettability increases as the gas gap is decreased. In contrast, the size of the gas gap has little to no effect on wettability for the flat electrode configuration.

This may be explained by the fact that in the case of the flat electrode configuration the voltage on the electrodes has to be increased to compensate for a larger gas gap, the electrical field strength is therefore maintained. But, this performance must be limited to the flat electrode configuration, because the experimental arrays with the sawtooth electrodes show a strong dependence of the measured contact angles to the size of the gas gap. However, this theory must be proved by the evaluation of the electrical measurements during the plasma treatment.

The low influence of the dielectric thickness does also not correspond to expectations. It was assumed, that the increase of the dielectric thickness would reduce the wettability, because the dielectric loss should be increased with thickness. The dielectric loss should reduce the amount of applied energy to the gas between the electrodes and lower thus the intensity of the plasma [123]. However, it was observed, that the dielectric thickness has little or no effect on the wettability of the treated BOPP films for the flat and the sawtooth electrode configurations. One possible explanation for this phenomena is again, that the high voltage power supply applies higher voltages to the electrodes, if the thickness of the dielectric is increased and compensates for the dielectric loss.

The findings of the experimental arrays with the sawtooth electrodes showed, that the results for the electrode with one tooth and with three teeth are almost identical. The contact angles of the experimental array with the five teeth electrode were much lower than the contact angles of the other two sawtooth electrodes. Especially, the maximum setting of the gas gap at 2.0 mm in combination with a relatively low thickness of the dielectric seems to cause an unequal treatment with an increased plasma intensity in the middle of the samples, whereas the borders receive an insufficient treatment. The reason therefore is a lower amount of ignited filaments, whose reignition occur mainly in the middle of the sample.

This behaviour can only be observed for the experimental array with the five toothed electrode. The reason that this effect does not with the one and three teeth electrodes, is probably the reduced area on top of the teeth, which reduces the space, where the filaments can be ignited. This limitation could lead to a more homogeneous distribution of the plasma, because the filaments are more concentrated over the reduced area.

The assumption, that the electrode area is important for the homogeneous distribution of the filaments for the sawtooth electrode, leads to the question: Why did the samples treated with the flat electrode configuration not show any irregularities in the surface treatment? The electrode area is significantly increased in comparison to the five tooth electrode and also the maximum setting for the gas gap (2.5 mm) much larger than the highest setting used in the experimental array for the sawtooth electrodes. Therefore, the settings, which caused the inhomogeneous treatment for the five teeth electrode, are increased for the flat electrodes.

Nevertheless, all samples processed with the flat electrode configuration were equally treated. Of course, covering both electrodes with the dielectric helps to stabilise a more homogeneous filament distribution, but does not explain the large amount of ignited filaments observed at these high gas gap settings. Therefore, it is assumed, that the high voltage power supply is able to apply more power to the flat electrodes than to the sawtooth electrode configuration and cause thus the ignition of additional filaments.

Comparison of these results with the work of other researchers is difficult, because it was not possible to find any publication concerning the utilisation of a sawtooth electrode configuration. The only research group, who studied the influence of different electrode structures is Wang, T. et al. [96, 131]. They studied the electrical characteristics of plane aluminium, plane water, mesh wire and coaxial electrodes. It is not possible to compare their work with the work presented here. The research groups involved with all other publications mentioned in the following utilised flat electrodes, both electrodes covered by a dielectric.

Wang, C. et al. [128, 132] studied the change in the wettability of PP films treated using an air plasma and varying the size of the gas gap and the applied power. They report an increase of the wettability by increasing the applied power to the electrodes. This corresponds well with our findings, because the increase in the current of the DC power supply results in an increase of the power applied to the electrode configuration. They characterise the influence of the size of the gas gap with an optimal setting, which leads to the lowest measured water contact angles. This gas gap is 1.5 mm. Our findings cannot confirm this result, but one important difference between their surface treatments and ours is, that Wang, C. et al. utilised

a static treatment while our method used a roll-to-roll system. Thereby, the samples of Wang, C. et al. were in contact with the plasma for a much longer time period, which could lead to different results. Additionally, also the work of Wang, K. et al. [91], who treated PP films in a nitrogen plasma confirmed the increased wettability of the treated films with increased power applied to the electrodes.

The voltage and current signals recorded during plasma treatment will be examined in order to investigate the different results observed for the experimental arrays with the flat and sawtooth electrode configurations. The unexpectedly minimal influence of the dielectric will also be investigated. These aspects will be discussed in the following chapter.

## 10 Investigation of electrical measurements during the discharge

The electrical characteristics measured during the plasma treatment and the Lissajous figures drawn from these measured values are investigated in this chapter in order to explain the different behaviour of the flat and the sawtooth electrode configurations. In addition, the influence of the three factors; current set on the DC power supply, the size of the gas gap and the dielectric thickness on the electrical power consumed is also investigated.

### 10.1 Observation of the voltage applied to the electrode configurations and discharge current

The voltage applied to the electrodes and the discharge current were measured using voltage and current probe (see Section 5.5). Ten thousand measurements were recorded over a  $2.0 \times 10^{-4}$  s time period. This corresponds to five recorded cycles of the sinusoidal voltage and discharge current, which are illustrated as example for experiment 1 of the five toothed electrode experimental array (Figure 54) and for the experimental array using flat electrodes (also with the settings of experiment 1) in Figure 55.

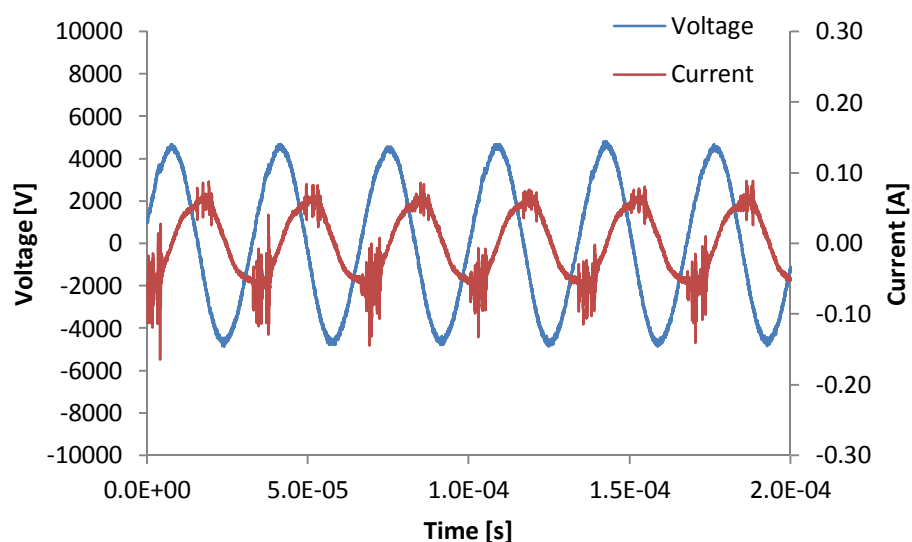


Figure 54: Measured voltage applied to the five tooth electrode configuration and the resulting discharge current for experiment 1 of the corresponding experimental array

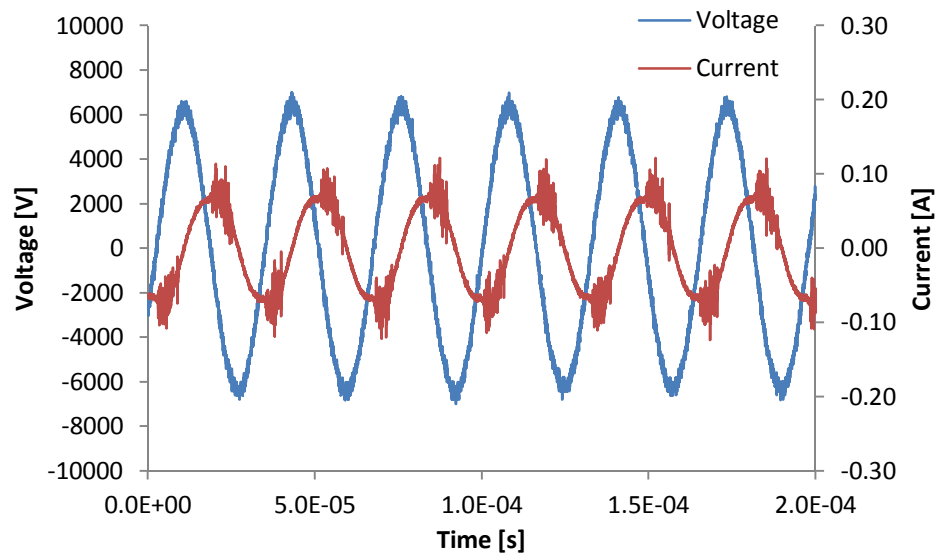


Figure 55: Measured voltage applied to the flat electrode configuration and the resulting discharge current for experiment 1 of the corresponding experimental array

The applied voltages and the discharge currents in Figure 54 and Figure 55 are phase-shifted by approximately 90 degrees. The voltage follows the current. The reason for these two effects are the capacitive properties of the electrode configurations. The signal of the discharge current has also a sinusoidal shape, but in addition several high frequency peaks are superimposed at the maximum amplitude. The sinusoidal part of the discharge current is the displacement current, which is created by the changing polarisation of the applied electrical field, which causes the displacement of electric particles in the nitrogen gas and the dielectric. The displacement current flows independent of whether the plasma is ignited or not.

The high frequency peaks superimposed on the current signal originate from the ignited plasma. They mark the increased current flow while the gas loses its dielectric properties and becomes conductive due to the high amount of free charge carriers in the plasma. The individual peaks are very narrow, which corresponds to a short burning time of the individual filaments in the nanosecond range. This clearly indicates, that the discharge regime is filamentary.

A direct comparison of the discharge currents of the experiments with the flat electrode and the sawtooth electrode configurations is not possible, because varied settings were used for the two experimental arrays. However, a significant difference could be spotted between the two electrode configurations. Whereas the current peaks of the plasma ignited between the

flat electrode configuration are of approximately the same size during the positive and negative polarisation (shown in Figure 55), in contrast the current peaks from the filamentary discharge of the sawtooth electrode configurations are significantly increased in size during the negative polarisation relative to those observed during the positive polarisation (shown in Figure 54).

This difference of the current peak size is a result of the asymmetric electrode configuration, which combines a flat electrode with a sawtooth electrode. It is assumed, that the sawtooth electrode is the cathode during the negative polarisation of the current. The seed electrons, which are accelerated from the cathode to the anode, would then receive more kinetic energy during the negative polarisation at the beginning of their acceleration, because the electrical field is strongly increased nearby the sawtooth electrode due to the edge effect. As a result of the increased kinetic energy, these seed electrons can cause more ionisation, which increases the current because more free electrons travel from the cathode to the anode. In the reverse case, when the seed electrons start near the flat electrode, which is then the cathode during the positive polarisation, their kinetic energy is not additionally increased by an edge effect. Thus, the current peaks are lower during the positive polarisation.

Besides the applied voltage and the discharge current, also the voltage drop across a measurement capacitor, which was connected in series to the electrode configuration, was monitored. The measured voltage drop enables the calculation of the transferred charge during the discharge, which is utilised to draw the Lissajous figures. These figures allow the minimum voltage necessary for the ignition of the plasma and the consumed power during the discharge to be estimated. The analyses of these electrical characteristics is presented in the following section.

## 10.2 Analysis of the Lissajous figures: the applied power

Lissajous figures are drawn by plotting the charge transferred during the discharge as a function of the applied voltage, as described in Chapter 6.1. The result ideally is a parallelogram, whose area equals the electrical energy during one discharge cycle. By multiplying the electrical energy with the frequency of the applied voltage, the consumed power during the discharge is calculated. Two examples of the Lissajous figures recorded are given in Figure 56

for the configuration with the five tooth electrode and in Figure 57 for the flat electrode configuration.

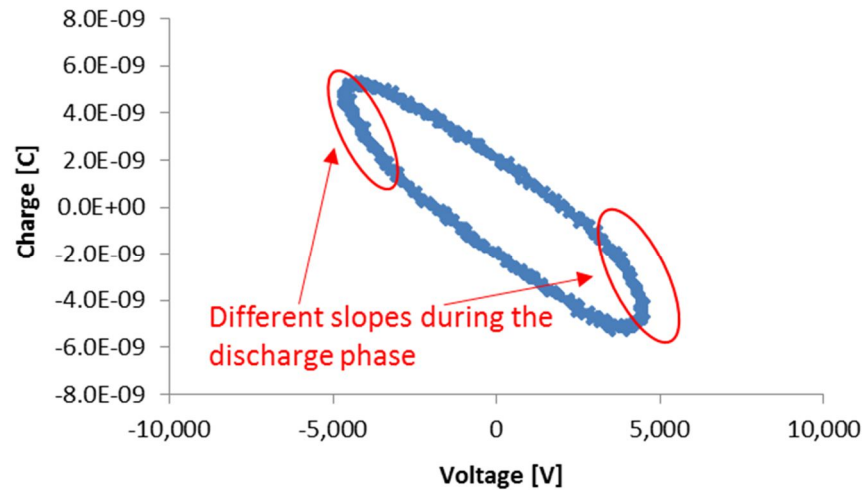


Figure 56: Lissajous figure of the experimental array of the five tooth electrode with the settings of experiment 1

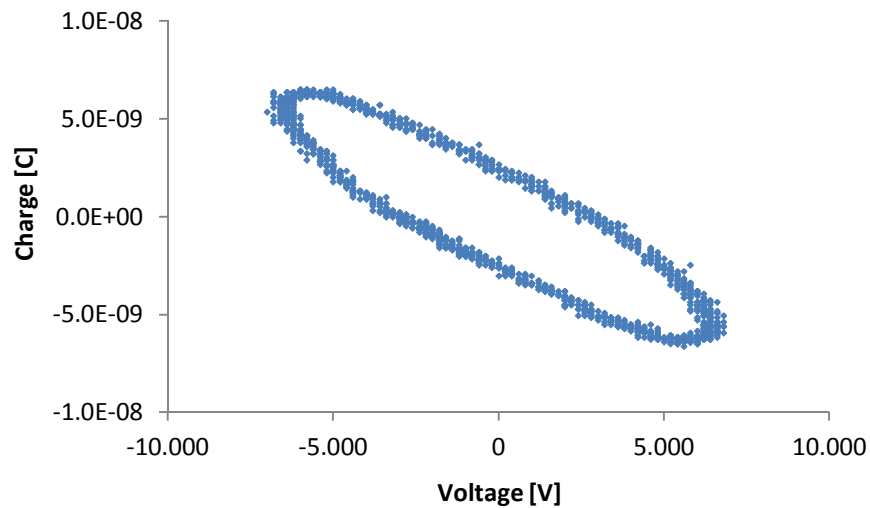


Figure 57: Lissajous figure of the experimental array of the flat electrode configuration with the settings of experiment 1

The Lissajous figure shown in Figure 57 is symmetrical, whereas the Lissajous figure shown in Figure 56 appears to have different gradients during the ignition of the discharge, whereby the transferred charge is lower for the positive polarisation. The reason is again the asymmetrical structure of the sawtooth electrode configuration, as already discussed in the previous section.

To study the influence of the three factors, thickness of the dielectric, size of the gas gap and the current setting, on the electrical power consumed by the electrode configurations during the discharge, the areas of the Lissajous figures of four different cycles were calculated by integration for every experiment making up the experimental arrays. The obtained electrical energy values obtained were multiplied by the frequency of the applied voltage for the corresponding experiment and the average of the four resulting electrical powers was estimated for every experiment of the experimental arrays. This average is then utilised as a response. The results of the multiple regression are shown in Figure 58 for the current set on the DC power supply, in Figure 59 for the thickness of the dielectric and in Figure 60 for the size of the gas gap of the experimental array with the flat electrode configuration.

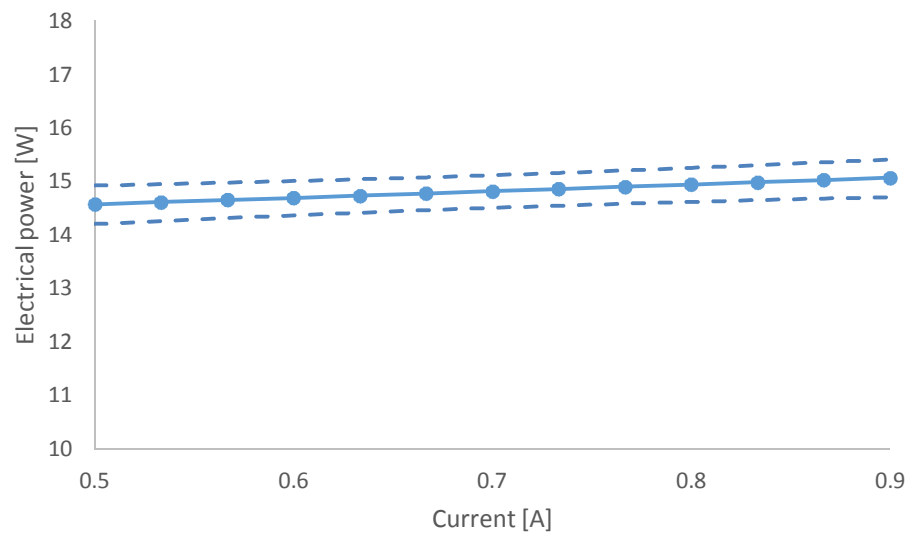


Figure 58: Influence of the current on the consumed electrical power for the flat electrode configuration

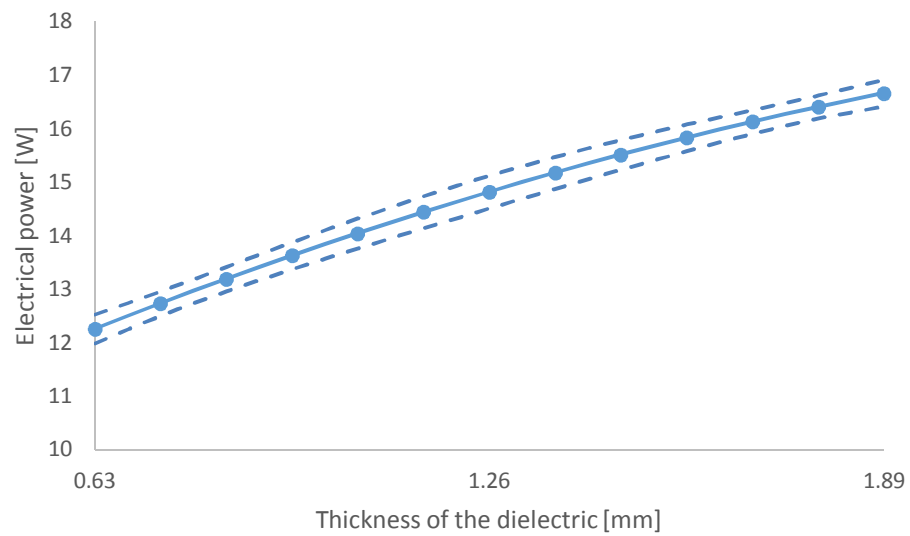


Figure 59: Influence of the dielectric thickness on the consumed electrical power for the flat electrode configuration

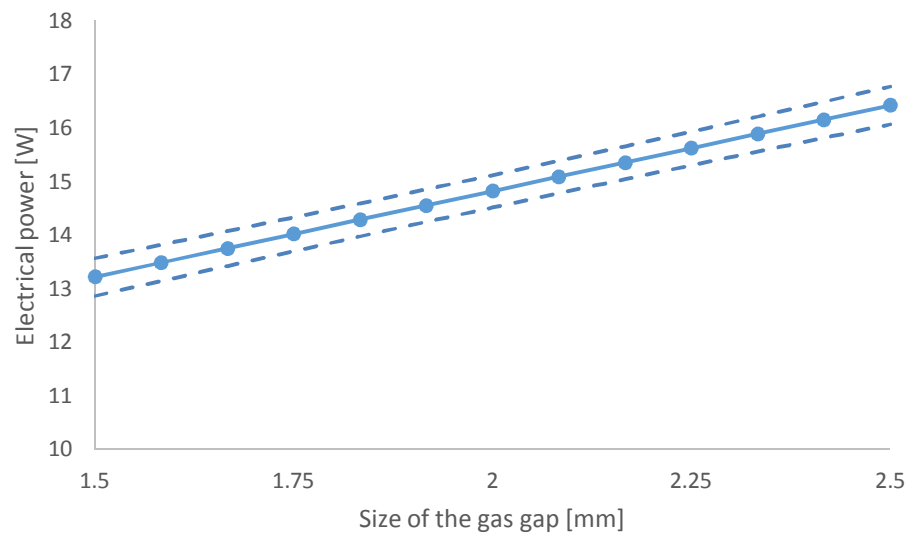


Figure 60: Influence of the gas gap size on the consumed electrical power for the flat electrode configuration

The trends showing Figure 58, Figure 59 and Figure 60 clearly indicate that the thickness of the dielectric and the size of the gas gap have the most influence on the electrical power consumed during the discharge. This power is increased by increasing the dielectric thickness or the size of the gas gap. The current setting on the DC power supply has almost no influence on the electrical power consumed during discharge. This is unexpected, because the current setting was chosen as the factor, which should influence the power applied to the electrodes. The coefficient of determination for the multiple regression,  $R^2$ , had a value of 0.96. Thus, the values of the calculated regression coefficients can be considered reliable.

The results of the multiple regression for the sawtooth electrode configurations are illustrated in Figure 61 for the current set on the DC power supply and in Figure 62 for the dielectric thickness. The size of the gas gap had no influence on the applied electrical power for all the sawtooth electrode configurations investigated. Therefore, these trends are not presented.

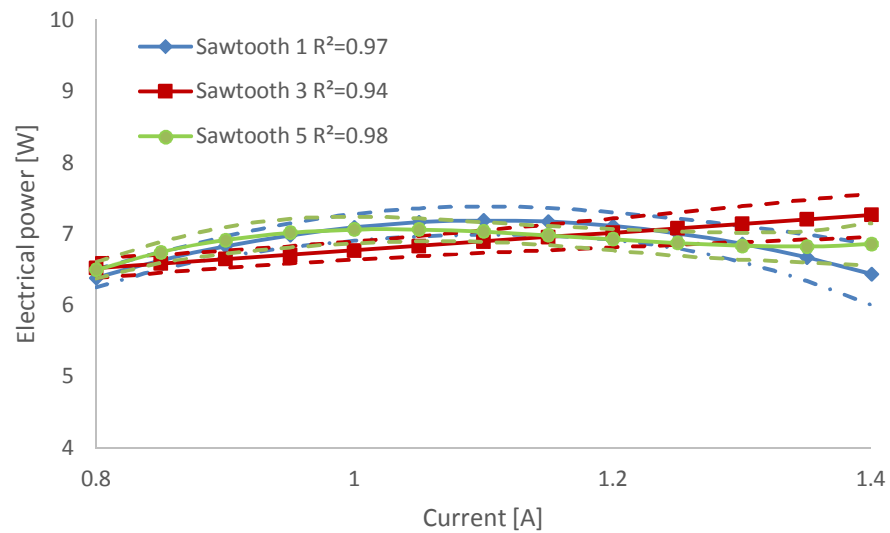


Figure 61: Influence of the current on the consumed electrical power for the sawtooth electrode configurations

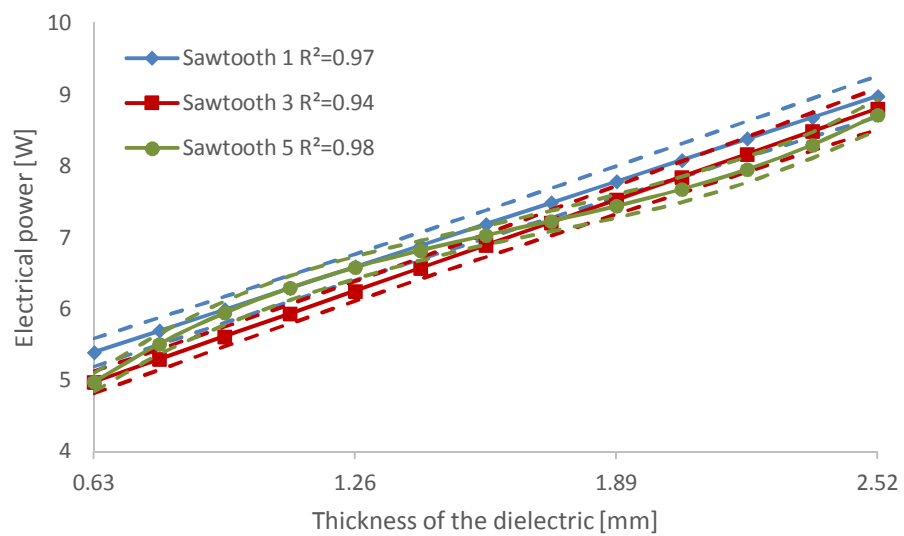


Figure 62: Influence of the dielectric thickness on the consumed electrical power for the sawtooth electrode configurations

The influence of the current set on the DC power supply on the electrical power consumed for the sawtooth electrode configurations is low in comparison to the influence of the dielectric thickness. An increase of the dielectric thickness leads to a significant increase in the electrical power consumed. These results were also observed for the flat electrode configuration. However, the two electrode configurations performed differently in terms of the effect of variation of the gas gap.

The power consumed increased with increasing gas gap size for the flat electrode configuration. In contrast to this, the size of the gas gap has no influence on the electrical power consumed for the sawtooth electrode configurations. These results correlate well with the water contact angles responses for the experiment arrays, because the gas gap also had a different impact there. The size of the gas gap did not influence the contact angles for the flat electrode configuration. However, lower water contact angles could be measured at reduced settings for the size of the gas gap in the experimental arrays with the sawtooth electrode configuration.

It was assumed that the electrical field is not reduced for the flat electrode configuration, when the size of the gas gap is increased. This would lead to the same intensity of the surface treatment independent on the size of the gas gap. An indication, that this theory is true, is the increase of the consumed electrical power with higher gas gap settings in Figure 60. This increase could compensate for the reduction of the electrical field at higher gas gap settings, which is synonymous to an increased distance between the electrodes, by an increase of the applied voltage.

Furthermore, this theory would explain, the higher water contact angles of the experimental array with the sawtooth electrode at increased gas gap settings. If a sawtooth electrode configuration is utilised, the applied electrical power is not increased at higher gas gap settings. Thus, the strength of the electrical field and the intensity of the plasma is reduced, when the gas gap is increased for this type of electrode configuration. This leads to a lower impact of the surface treatment and a lower wettability of the treated BOPP films to polar substances.

These results reveal, that the shape of the electrodes and the structure of the electrode configuration have a strong influence on the manner of the voltage application from the high voltage power supply to the electrode configuration. Additionally, the electrical power consumed of the two types of electrode configuration show in comparison, that the sawtooth electrode configurations are not only superior regarding the increase of the wettability, but also need less electrical power to achieve this better result.

There is no significant difference for the three investigated sawtooth electrode configurations regarding the amount of consumed electrical power in Figure 61 and Figure 62. This fact gives evidence to the theory, that the lower measured contact angles in the experimental array with the five tooth electrode in comparison to the one and three tooth electrode in Figure 45 and Figure 46 are not caused by a more intense surface treatment, because more power was applied to the electrode configuration, but rather by an unfavourable distribution of the filaments, as previously described in Chapter 9.2.

The increase of the electrical power with increasing dielectric thickness, which was estimated for the flat electrode configuration in Figure 59, as well as for the sawtooth electrode configurations in Figure 62, does not lead to an increase of the wettability of the treated BOPP films. An influence of the dielectric thickness on the water contact angles could not be estimated from the conducted experimental arrays investigated for both types of electrode configurations. However, it was already assumed that the high voltage power supply applies higher voltages to the electrode configuration to compensate for the dielectric loss, which is increased with an increased thickness of the dielectric. In the following section, the minimum voltage for the ignition of the plasma and the effective voltage applied to the electrode configuration is investigated to provide more evidence to these estimations.

### **10.3 Analysis of the Lissajous figures: Investigation of the minimum voltage for the ignition of the plasma**

The following analysis was only conducted for the five toothed sawtooth electrode configuration, because it could be demonstrated, that the high voltage power supply applies the same amount of electrical energy, independent of the number of teeth of the sawtooth electrode utilised. The flat electrode configuration is also no longer considered, as the surface treatment with this type of electrode configuration was less effective than with the sawtooth electrode configurations.

The Lissajous figures allow the electrical power applied to the electrode configuration to be estimated. In addition, it is also possible to calculate the minimum voltage, which is necessary to ignite the plasma in the gas gap between the two electrodes. This value is determined by calculating the y-intercept of the Lissajous figure during the positive and the negative polarisation of the applied voltage during one cycle.

The minimum voltage for the ignition of the plasma was first separately estimated for the negative and the positive polarisation for four electrical cycles of every conducted experiment to investigate a possible difference between the two values, which could be caused by the varied shapes of the two electrodes, as already discussed in Chapter 10.1. However, the minimum voltage for the negative and the positive polarisation did not differ significantly. As a consequence, these values of the minimum voltage for every experimental setting of the experimental array were averaged and the resulting value was utilised as a response in the experimental array.

In addition, the effective voltage applied to the electrodes was calculated from the measured voltage waveforms for every setting of the experimental array with the following equation:

$$V_{eff} = \sqrt{\frac{1}{T} \int_0^T V^2(t) dt} \quad (25)$$

The effective voltage was also utilised as a response in the experimental array for the saw-tooth electrode configuration with the five tooth electrode. The results of the multiple regression of the minimum voltage for the plasma ignition and of the effective voltage are presented in Figure 63 for the thickness of the dielectric. The size of the gas gap and the current setting did not have a measurable influence on the minimum voltage and their effect on the effective voltage is minor in comparison to the thickness of the dielectric. Therefore, the results of the multiple regression for the size of the gas gap and the current setting are not shown.

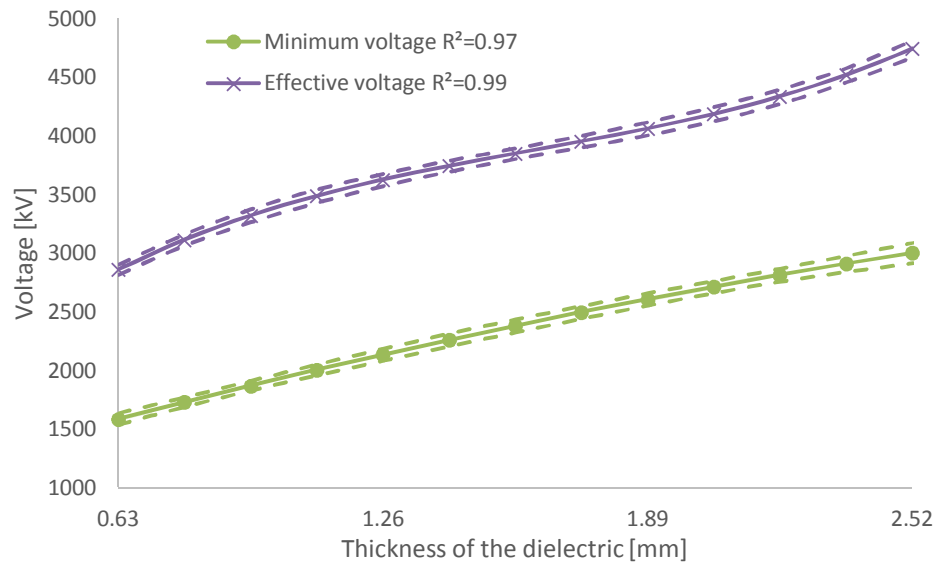


Figure 63: Minimum voltage for the ignition of the plasma and the effective voltage applied to the electrode configuration with the five tooth sawtooth electrode depending on the thickness of the dielectric

The thickness of the dielectric is the main influence on both the minimum voltage for the plasma ignition and of the effective voltage applied to the electrode configuration of the three investigated factors of the experimental array. The effective voltage and the minimum voltage for the discharge ignition are both increased with the increased dielectric thickness, as shown in Figure 63. The increased minimum voltage is probably caused by an increased dielectric loss, which should be the greater, the more the thickness of the dielectric is increased.

On the one hand, these results show clearly, that an increase of the dielectric thickness leads to a higher consumption of the electrical power, because higher voltages must be applied to the electrodes in order that the minimum voltage is exceeded and the discharge is ignited. On the other hand, the results of the effective voltage reveal, that the high voltage power supply automatically applies higher voltages to the electrode configuration, if the thickness of the dielectric is increased.

The slope of the minimum voltage function and the effective voltage function in Figure 63 are very similar, so that the distance between the two functions is always equal independent on the thickness of the dielectric. This means, that the high voltage power supply compensates the increased minimum voltage for the plasma ignition by increasing the applied voltage, in order that the same amount of voltage is applied to the gas in the gas gap of the electrode configuration independent of the dielectric loss. This results in the same plasma

intensity if the size of the gas gap and the current setting is constant. Therefore, the thickness of the dielectric had no influence on the measured water contact angles in the investigated experimental array with the sawtooth electrode configuration in Chapter 9.2. The same is probably valid for the flat electrode configuration, because the results of the corresponding experimental array showed also only a low influence of the dielectric thickness on the water contact angles of the treated BOPP films (shown in Figure 41).

It can be concluded, that the thickness of the dielectric has no influence on the wettability of the plasma treated BOPP films, but it is the main factor, determining the amount of consumed electrical power. Therefore, the thickness of the dielectric should be kept as small as possible, whereby the lower border is the breakdown voltage of the utilised dielectric, which must be higher than the applied voltage.

In the last section of this chapter the question of why the current setting on the DC power supply has only a minor influence on the power applied to the sawtooth electrode configuration (shown in Figure 61), is discussed, although this factor was chosen for the investigation of the influence of the amount of power applied to the electrode configuration on the changed wettability of the treated BOPP films.

#### **10.4 Calculation of the power applied to the gas in the gas gap of the sawtooth electrode configuration**

The current setting on the DC power supply was chosen to be the factor, which mainly influenced the applied power from the high voltage power supply to the electrode configuration. However, it was observed, that the thickness of the dielectric had much more influence on the applied power than the current setting. The current setting had, in contrast to the thickness of the dielectric, a strong influence on the wettability of the treated BOPP films. Therefore, it was assumed, that the majority of the electrical power, which is additionally applied to the electrode configuration as a result of an increase of the dielectric thickness, was used to compensate for the increased dielectric loss.

Otherwise, the supplementary electrical power applied to the electrode configuration, caused by higher current settings on the DC power supply, is directly applied to the gas in the gas gap between the two electrodes. This leads to an increase of the plasma intensity and thus to an increase of the wettability of the treated BOPP films. However, the increase of the power

by higher settings of the current is superimposed by the much higher increase of the electrical power by an increased dielectric thickness (shown in Figure 61 and Figure 62).

To give evidence to this theory, it is necessary to determine the electrical power, which is applied to the gas in the gas gap for the ignition and the maintaining of the plasma. This power is called the discharge power,  $P_d$ , and is calculated by the following equation from the voltage applied to the gas gap,  $V_{gap}$ , and the plasma current,  $I_{plasma}$ , according to [133]:

$$P_d = \frac{1}{T} \int_0^T V_{gap}(t) \cdot I_{plasma}(t) dt \quad (26)$$

The voltage applied to the gas gap,  $V_{gap}$ , derives from the subtraction of the voltage drop over the dielectric layer,  $V_{die}$ , and of the voltage drop over the measurement capacitor,  $V_d$ , from the voltage applied to the electrode configuration,  $V_a$ , as shown by Equation 27.

$$V_{gap}(t) = V_a(t) - V_{die}(t) - V_d(t) \quad (27)$$

The voltage drop across the measurement capacitor,  $V_d$ , and the voltage applied to the electrode configuration,  $V_a$ , are directly measured. This is not possible for the voltage drop over the dielectric layer, which needs to be calculated. Mangolini et al. [134] states that the voltage drop over the dielectric layer is proportional to the voltage drop across the measurement capacitor and can be thus calculated by the following equation:

$$V_{die}(t) = \frac{c_{meas}}{c_d} \cdot V_d(t) \quad (28)$$

The capacitance of the measurement capacitance,  $c_{meas}$ , is known. The capacitance of the dielectric layer,  $c_d$ , must be estimated manually from the slope of the Lissajous figure during the discharge phase, as described in Chapter 6.1. For the calculation of the discharge power four electrical cycles of the voltage applied to the electrode configuration and of the voltage

drop across the measurement capacitance were considered. The capacitance of the dielectric layer was calculated for the positive and the negative polarisation of the cycle and the resulting eight values of the four considered cycles were averaged for the calculation of the voltage drop over the dielectric layer.

The current measured on the high voltage side of the high voltage power supply is composed of the sinusoidal displacement current and the plasma current, which is characterised by short peaks in the nanosecond range (shown in Figure 55 and Figure 56). To separate the plasma current from the displacement current, a low-pass filter is utilised on the measured signal, which removes the plasma current, so that the displacement current is obtained. The subtraction of the displacement current from the measured discharge current yields in the wanted plasma current. For this mathematical operation, the computer program Matlab, version R2014a, was used. The program code for the low-pass filter was compiled with the signal processing toolbox (version 6.21) of the Matlab program and is presented in Appendix B.

The utilisation of the low-pass filter on the measured current signal does not only remove the plasma current, but also causes a phase difference to the original signal, as shown in Figure 64. To be able to negate the phase difference, the phase angle is calculated with another Matlab program created by Shashank S. [135]. The program code of this Matlab program can be found in Appendix C. By estimating the phase angle,  $\varphi$ , between the discharge current and the displacement current, the time offset,  $\Delta t$ , between the two functions was calculated by Equation 29 and the displacement current shifted by this time offset, so that the phase difference is negated. The subtraction of the displacement current from the discharge current then provides the plasma current. An example of this calculation is given in Figure 65.

$$\Delta t = \frac{\varphi \cdot T}{2\pi} \quad (29)$$

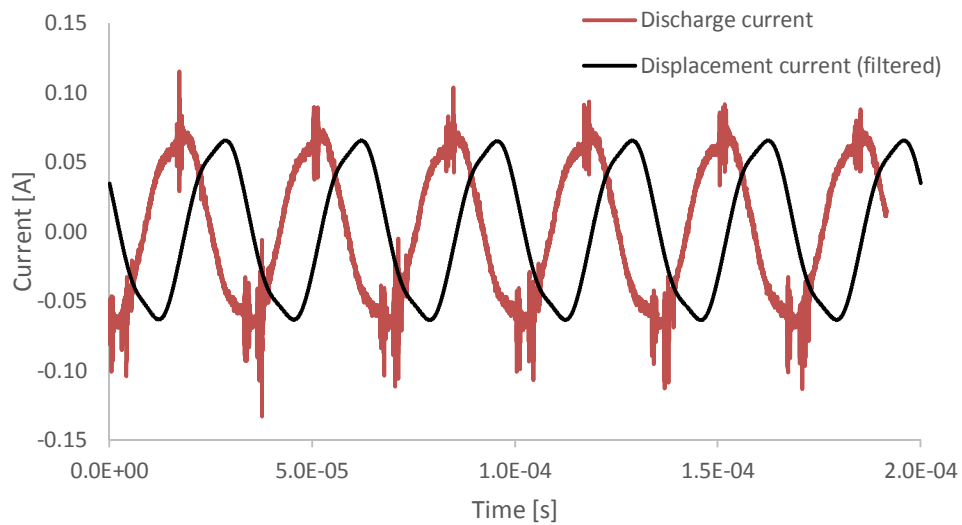


Figure 64: Discharge and displacement current of experiment 1 of the experimental array with the five tooth sawtooth electrode configuration

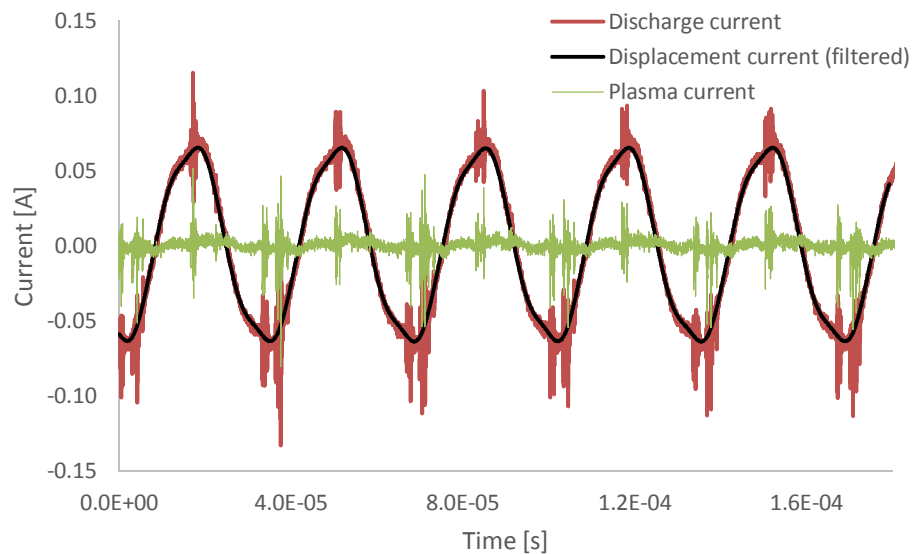


Figure 65: Calculation of the plasma current by the subtraction of the displacement current from the discharge current of experiment 1 of the experimental array with the five tooth sawtooth electrode configuration

The discharge power was calculated with the estimated plasma current and the voltage applied to the gas gap for all the experiments of the experimental array of the sawtooth electrode with five teeth. The discharge power was then utilised as the response in this experimental array. The results of the multiple regression are presented in Figure 66 for the current set on the DC power supply and in Figure 67 for the thickness of the dielectric. The size of the gas gap has no influence on the discharge power and is therefore not illustrated.

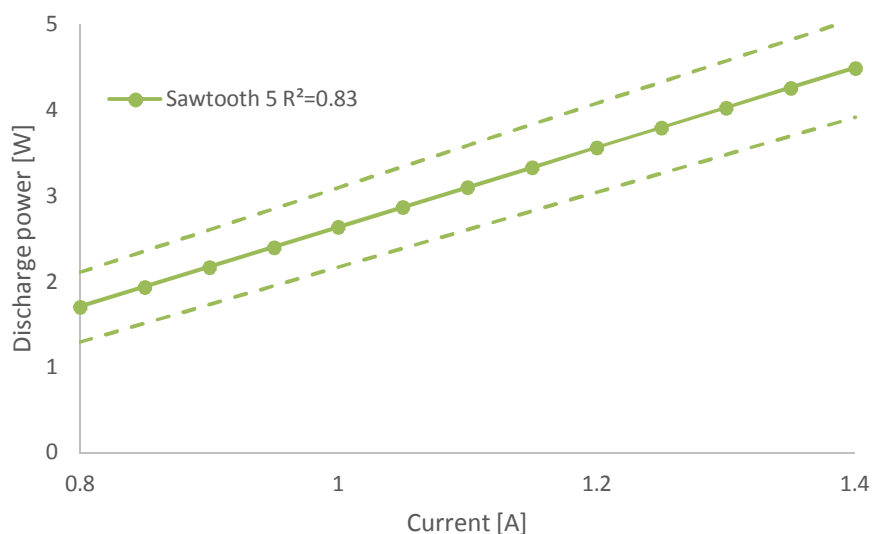


Figure 66: Influence of the current setting on the discharge power for the sawtooth electrode configuration with five teeth

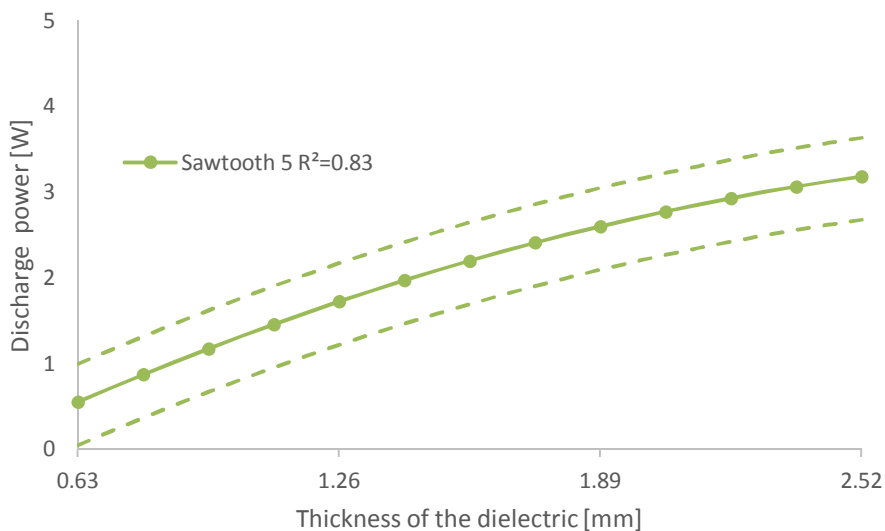


Figure 67: Influence of the dielectric thickness on the discharge power for the sawtooth electrode configuration with five teeth

The results of Figure 66 reveal that the discharge power is significantly increased if higher values for the current are set on the DC power supply. This correlation is important, because the increased discharge power probably leads to a more intense plasma treatment. More energy is applied to the gas in the gas gap resulting in higher creation rates of the metastable species, which react with the surface of the BOPP films. If the concentration of the reactive

particles is increased, because more energy is applied to the gas, more surface reactions take place on the surface of the treated films. This increases the wettability of the substrate, because more polar chemical groups are formed on the surface, which also receives a stronger etching. This consideration is supported by the measurement of the reduced water contact angles, which is equivalent to an increased wettability, of the BOPP samples treated at higher current settings (shown in Figure 45).

The influence of the dielectric thickness on the discharge power is illustrated in Figure 67. An increase of the dielectric thickness led to an increase of the discharge power. This is unexpected, because the experimental array with the water contact angles did not show an influence of the dielectric thickness on the wettability of the BOPP films. Therefore, it is assumed that this increase is a result of the extension of the electrical field caused by the dielectric. An increase of the dielectric thickness does not only lead to a homogenisation of the electrical field, but also extends the electrical field above the area of the covered electrode. This extension is greater the more the thickness of the dielectric is increased and leads to the ignition of additional filaments at the borders of the sawtooth electrode, as shown by Figure 68, where two discharges with the same current and gas gap setting, but different dielectric thicknesses, are compared to each other. The additional ignited filaments do not have an influence on the wettability of the treated BOPP films, because these filaments are not in contact with the BOPP film, which is positioned in the centre of the electrode configuration. The increased discharge power with increasing the thickness of the dielectric has therefore no influence on the wettability of the treated BOPP films.

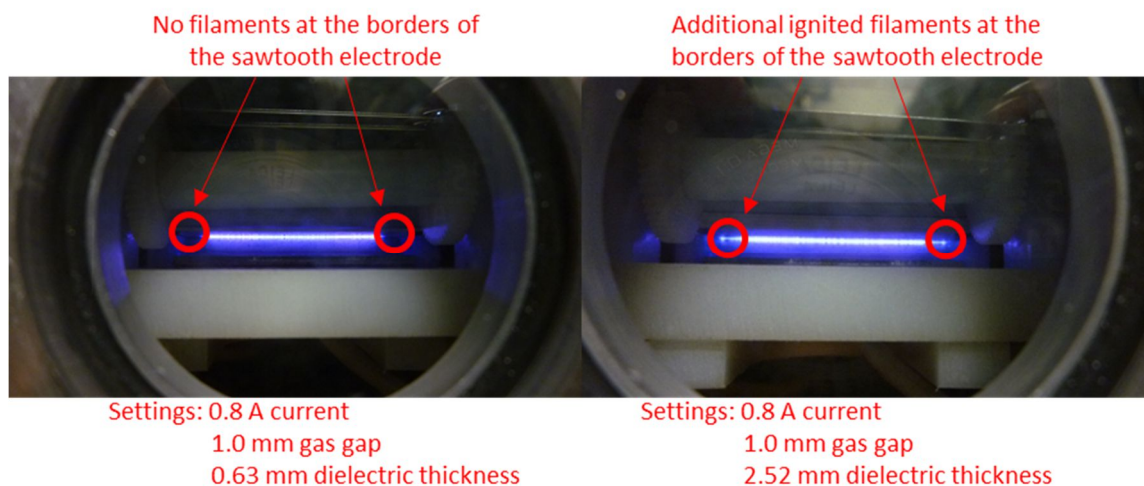


Figure 68: Extension of the electrical field by increasing the dielectric thickness for the sawtooth configuration with one tooth visible through the ignition of additional filaments

In the last two chapters, the three factors, current set on the DC power supply, size of the gas gap and thickness of the dielectric were investigated to study their influence on the wettability of the plasma treated BOPP films. Furthermore, two different types of electrode configurations were utilised in the conducted experiments. The results revealed that the sawtooth electrode configurations are superior, in comparison to the flat electrode configuration, regarding the wettability and the amount of consumed power.

The optimal settings for the plasma treatment with the sawtooth electrode configuration regarding the wettability of the treated BOPP films are a narrow gas gap and a high current setting on the DC power supply, which is equal to a high discharge power applied to the gas gap. The thickness of the dielectric has no influence on the wettability of the treated BOPP film, but is the main factor, which determines the amount of consumed power by the electrode configuration. Therefore, the thickness of the dielectric should be kept as small as possible to reduce the consumption of electrical power. These results were transferred to the industrial DBD system. The findings of these experiments are presented in the next chapter.

## **11 Investigation of the BOPP films treated in nitrogen with admixtures**

The optimal settings for surface treatment of BOPP using the sawtooth electrode configuration, determined using laboratory scale treatment rig. These conditions were then applied the industrial DBD system. The power applied to the electrode configuration, the dielectric thickness and the gas gap were kept constant at the optimal settings, but the composition of the atmosphere in the gas gap was varied. The treatments were performed in nitrogen gas with admixtures of nitrous oxide or acetylene (ethyne) in the ppm range. The surface energy and the elemental composition of the treated BOPP films were investigated by contact angle, XPS and ToF-SIMS measurements. Furthermore, the BOPP films were also treated in nitrogen with admixtures of nitrous oxide, acetylene and carbon oxide on the laboratory DBD system.

### **11.1 The surface energy of the treated BOPP films treated on the industrial DBD system**

The results reviewed in Chapter 9 and 10 showed, that a high power applied to the gas between the electrodes and a small size of the gas gap led to BOPP films, which are optimally treated in terms of their wettability by polar substances. Therefore, the settings for the surface treatment with the industrial DBD system (presented in Section 5.6) were chosen to be minimum with 900  $\mu\text{m}$  for the gas gap and maximum with 20 kW for each of the four generators for the power applied to the electrodes. The speed of the BOPP film during the treatment was 275 m/min. The thickness of the silicone rubber dielectric is not alterable and is thus kept constant at 5 mm.

The BOPP films were treated in pure nitrogen and in nitrogen admixed with the following reactive gases; nitrous oxide and acetylene at concentrations each of 25 ppm, 50 ppm, 75 ppm and 100 ppm. The reactive gases are intended to influence the surface treatment, so that different functional groups are created on the polymer surface. Increasing the reactive gas concentration above 100 ppm is not applicable for industrial process, because a white powder deposits from the gaseous phase on the lower electrodes as the concentration of the admixture is increased. This deposition necessitates the cleansing of the lower electrode, which

interrupts the continuous production. The white powder is probably a product of a plasma polymerisation reaction of the reactive gas as monomers.

The treated BOPP films were investigated approximately six hours after the treatment by making contact angle measurements with the testing liquids water, diiodomethane and ethylene glycol. Ten replicate contact angles were measured for every testing liquid for each sample. The averages of these ten replicate measurements were utilised to calculate the dispersive component and the polar component of the surface energy, as well as the total surface energy of the treated films, as described in Section 6.2. The error of the estimated variables were calculated from the linear regression by the propagation of uncertainty. The equations utilised are presented in Appendix D. Values determined for the polar and the dispersive components of the surface energy and the total surface energy for the acetylene and nitrous oxide doped atmospheres as shown in Figure 69 and Figure 70, respectively.

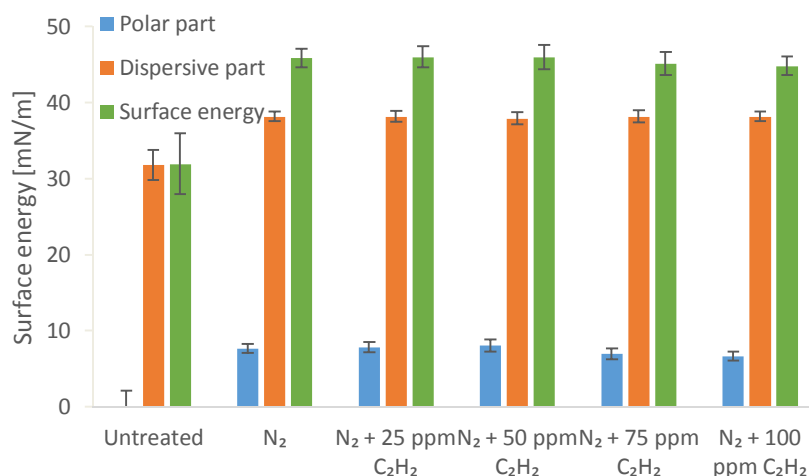


Figure 69: The polar part, the dispersive part and the surface energy of the BOPP films treated by the industrial DBD system with admixtures of acetylene

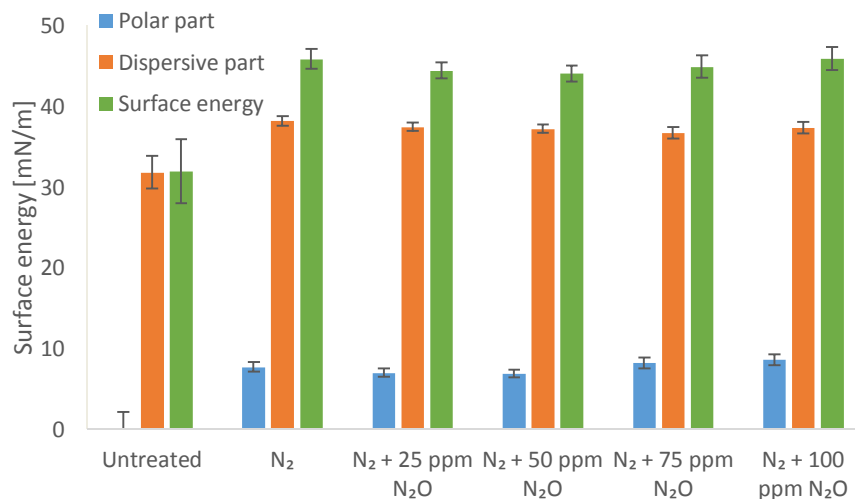


Figure 70: The polar part, the dispersive part and the surface energy of the BOPP films treated by the industrial DBD system with admixtures of nitrous oxide

The results in Figure 69 and Figure 70 show, that the plasma treatment increases both the polar and the dispersive part of the surface energy of the BOPP film each by about a value of 7 mN/m on average. The surface energy is thus increased in total from 32 mN/mm to approximately 46 mN/mm. The increase of the polar part of the surface energy is a result of the incorporation of electronegative chemical groups on the surface of the treated BOPP [136]. The increase of the dispersive part is an indication that the plasma treatment led to an enhanced crosslinking of the polymer chains [137]. A significant difference between the surface energies for the treatments with nitrogen and the different concentrations of admixtures could not be observed for either acetylene or nitrous oxide. All surface treatments seem to lead to the same result independent on the type or the concentration of the reactive gas.

To investigate the stability of the surface energy of the treated BOPP films, also called hydrophobic recovery or aging behaviour, the contact angle measurements were repeated every 24 hours over 30 days for the samples treated in pure nitrogen and in nitrogen with 100 ppm nitrous oxide or acetylene. The samples treated with reactive gas concentration less than 100 ppm were not considered, as the surface energies of these samples, estimated after six hours of the treatment, did not show any significant difference to each other. The calculated surface energies are presented as function of the time after the plasma treatment in Figure 71.

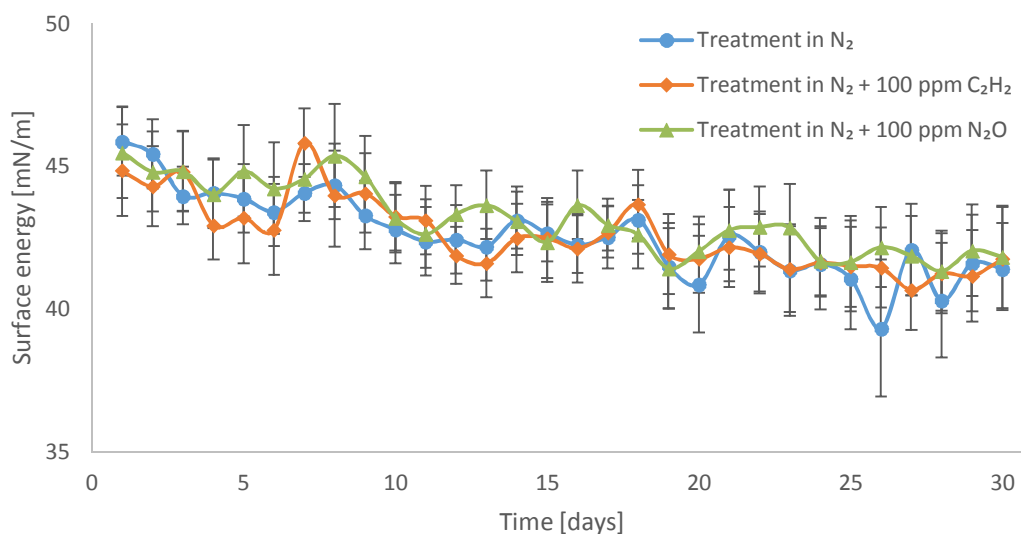


Figure 71: Surface energy versus time data for the BOPP samples treated by the industrial DBD system

The results of Figure 71 reveal that there is also no significant variation between the surface energies of the samples treated in nitrogen or in nitrogen with an admixture over the time after the plasma treatment. The hydrophobic recovery of all investigated samples is slow, but certainly measurable, on average the surface energy was reduced by 4 mN/m over 30 days. However, it is not possible to determine, whether this reduction is ascribed to the decrease of the polar part, the dispersive part or both.

The hydrophobic recovery of PP films treated in an air plasma at atmospheric pressure occurs faster in comparison to the investigated surface treatment in nitrogen. Novak I. et al. [138] treated polypropylene films in air and investigated the stability of the surface energy. For their films, the original surface energy of 47 mN/m, measured directly after the plasma treatment, fell by 13 mN/m within 30 days. The reduction proceeded exponentially, whereby a stable surface energy of 33 mN/m was reached after 50 days. Additional studies about the hydrophobic recovery of PP films treated in air plasma can be found in [139] and [140]. However, these references only measured the increase in water contact angle with time, which also indicated a fast hydrophobic recovery of the treated films, but do not allow direct comparison with the findings presented here.

These examples of air treated PP films show the advantage of the nitrogen plasma utilised. The hydrophobic recovery is strongly reduced, if nitrogen is used instead of air. As a result of the reduced hydrophobic recovery, BOPP films treated with a nitrogen plasma can be stored longer without the need of refreshing the surface treatment, when the BOPP films are proceeded further by lamination or printing.

The reason for the hydrophobic recovery is, that the plasma treatment puts the surface of the treated polymer into a state that is not at thermodynamic equilibrium. The system tries to reduce the high energetic level by decreasing the increased surface energy. This decrease was studied by XPS measurements, which indicated, that the amount of electronegative elements is reduced over the time on the surface of the treated PP films [112, 141, 142]. Morra M. et al. [143] ascribe the reduction of the electronegative groups to a rearrangement of the polymer chains, which are close to the surface of the treated polymer. This leads to the replacement of the functional groups from the surface towards the bulk of the polymer and thus to the reduction of the surface energy. Pascual et al. [144] take also consider, that LMWOM could migrate from the surface into the bulk of the polymer and additives from the bulk close to the surface.

## 11.2 Results of the XPS measurements

The XPS measurements for this project were performed by Dr Steve Hinder from the University of Surrey. A theta probe angle-resolved X-ray photoelectron spectrometer (Thermo Fisher Scientific Inc.) with an aluminium K-alpha X-ray source (1486.6 eV) was used to measure a spot of  $700 \mu\text{m}^2$  on every sample. The penetration depth of the XPS measurement is in order of nanometres. Wide scans from 0 to 1400 eV have been completed to identify the elements on the sample (Figure 72) and narrow scans of the 1s peaks of carbon (282-290 eV, Figure 73), nitrogen (395-404 eV, Figure 74) and oxygen (528-537 eV, Figure 74) have been measured for the determination of the elemental composition.

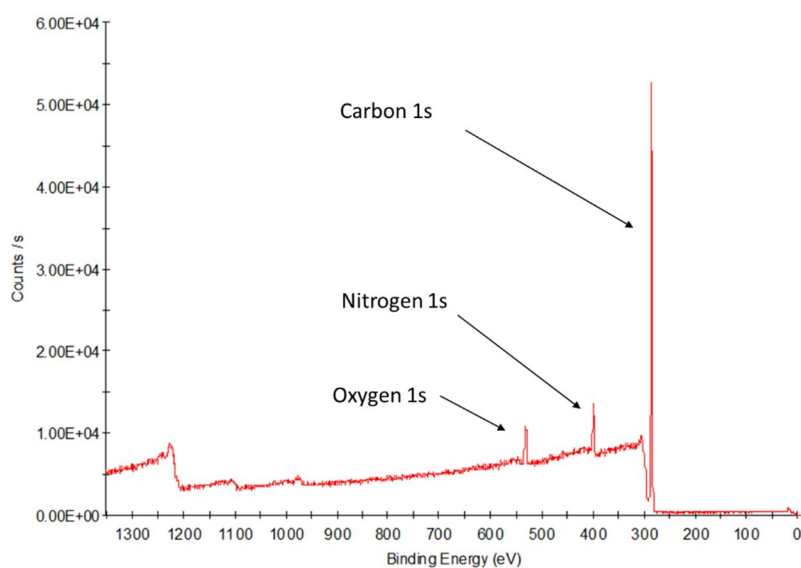


Figure 72: XPS wide scan of BOPP sample treated in pure nitrogen

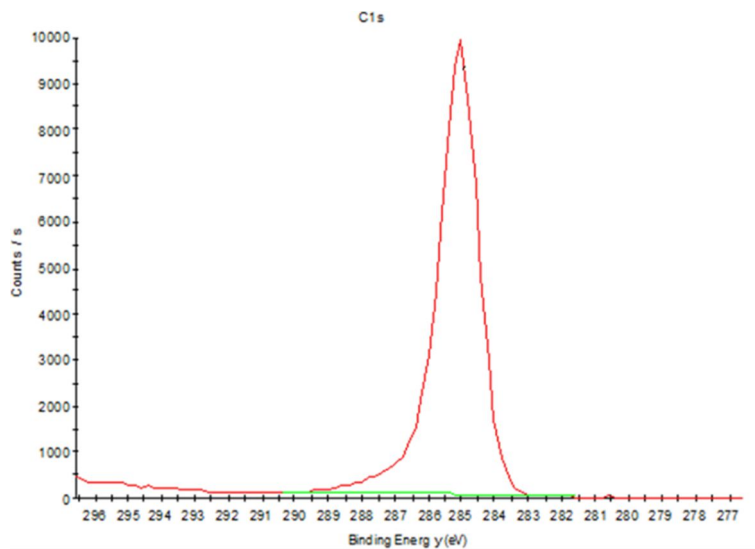


Figure 73: XPS narrow scan (Carbon 1s) of the BOPP sample treated in pure nitrogen

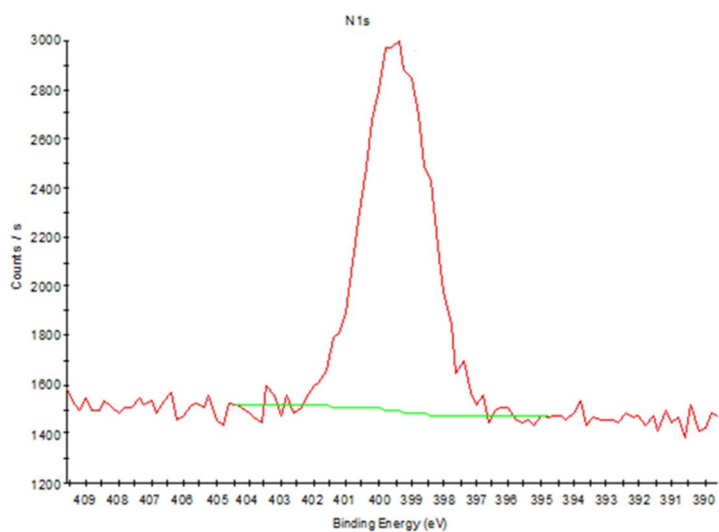


Figure 74: XPS narrow scan (Nitrogen 1s) of the BOPP sample treated in pure nitrogen

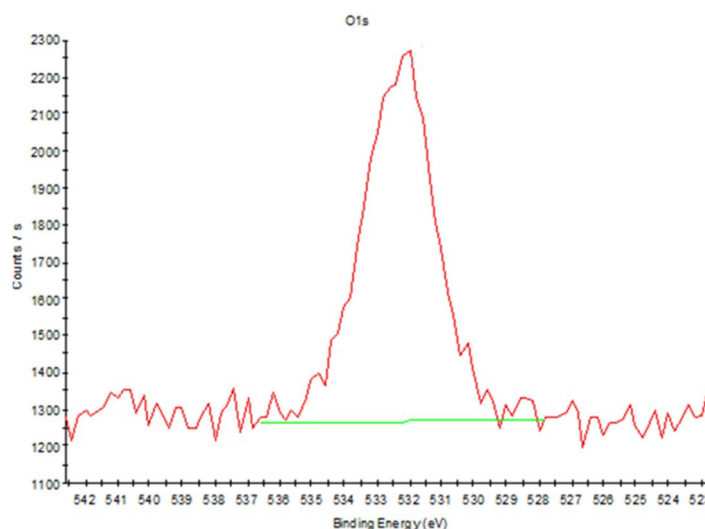


Figure 75: XPS narrow scan (Oxygen 1s) of the BOPP sample treated in pure nitrogen

Due to the high costs of the XPS measurements, every sample treated by the industrial DBD system was only measured once. Therefore, it is not possible to indicate the error of the individual measurements. The results of these measurements are illustrated in Figure 76 for the acetylene doped nitrogen and in Figure 77 for the nitrous oxide doped nitrogen. Only the percentage of nitrogen and oxygen are presented. The amount of carbon is not shown, but can be calculated by subtraction of the percentage of nitrogen and oxygen from 100 %, because no other elements than carbon, oxygen and nitrogen were detected.

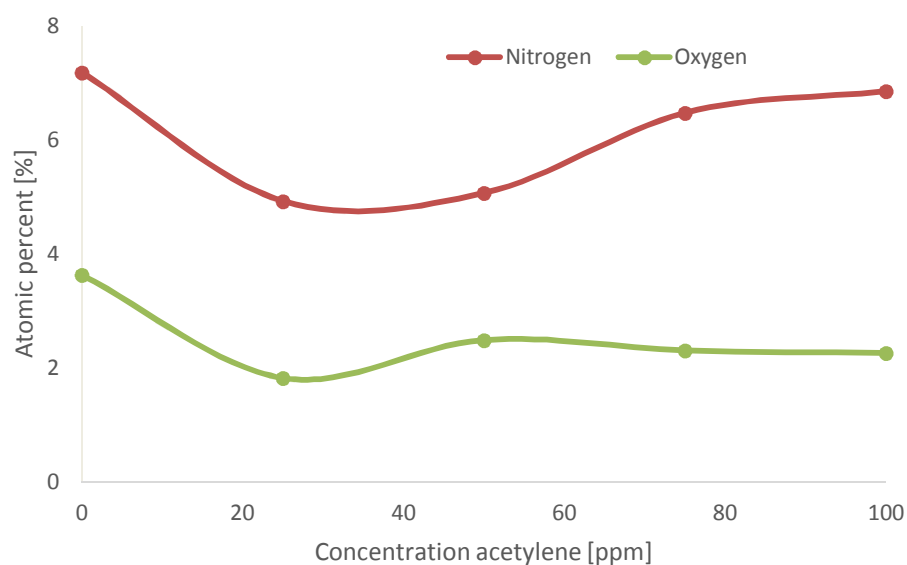


Figure 76: Nitrogen and oxygen content of the samples treated by the industrial DBD system with the reactive gas acetylene

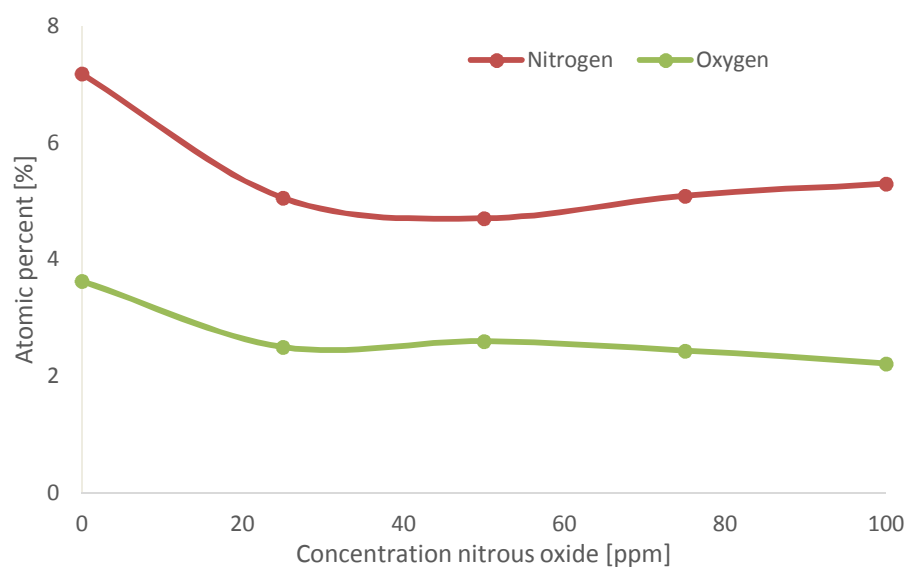


Figure 77: Nitrogen and oxygen content of the samples treated by the industrial DBD system with the reactive gas nitrous oxide

The XPS measurements indicate that both nitrogen and oxygen atoms were incorporated in the surface of the treated BOPP films. The XPS measurement of an untreated sample yielded in an atomic percent of 100 % carbon. The results in Figure 76 show, that there is an indication of a trend for the nitrogen content, which increases with the increased concentration of the admixture acetylene. Such a trend cannot be observed for the oxygen content and for the

samples treated with the admixture nitrous oxide. However, all samples treated with an admixture showed lower amounts of incorporated oxygen and nitrogen than the sample treated in pure nitrogen gas. It is not clear whether the differences of the measured amounts of oxygen and nitrogen are significant, because the identification of the measurement error is not possible. It is assumed, that the differences are not significant, since no variations of the surface energies between the individual samples could be observed.

The detected oxygen on the treated samples is unexpected, because the gases utilised in the gas gap between the electrodes should only have contained oxygen in traces. However, the comparison with the findings of other research groups indicates, that also their treated PP films also treated in pure nitrogen contain oxygen [90, 112, 113, 145]. None of these publications discuss the source of the incorporated oxygen. It is assumed, that the oxygen atoms originate from water or oxygen adsorbed on the surface of the BOPP film. The high amount of incorporated oxygen on the surface of the BOPP films in comparison to the amount of incorporated nitrogen leads to the assumption, that mainly the excited particles, which are close to the surface of the BOPP film, react with the polymer surface. Excited particles created further away from the surface have a lower probability to react with the polymer surface, because they have to overcome a longer distance by diffusion in order that a reaction with the surface of the polymer can take place. This theory would also explain, why the admixtures in the nitrogen gas did not have a significant influence on the surface energies of the treated films.

The atmosphere close to the surface of the polymer contains the particles, which mainly react with the surface of the polymer. It is easily imaginable, that substances adsorbed onto the polymer surface influence the composition of the gas close to the polymer surface in greater concentrations than 100 ppm. The adsorbed substances have thus the greater impact on the surface treatment than the gaseous admixtures in the nitrogen. Therefore, no significant differences in the surface energies of the samples treated with the concentrations up to 100 ppm of nitrous oxide and acetylene could be measured. In the next section, the results of the surface treatment with higher concentrations of the admixtures with up to 500 ppm are discussed.

### 11.3 Films treated with higher concentrations of the admixtures

The BOPP films treated with the industrially DBD system did not show differences in the surface energies, if nitrous oxide or acetylene were used to dope to the nitrogen gas. However, a white powder was produced in the plasma during the treatment, if the admixtures were added to the nitrogen. The white powder leads to contamination of the lower electrode. Therefore, higher concentrations than 100 ppm are not suitable for the industrial process.

To investigate whether concentrations of the admixtures from 100 ppm up to 500 ppm have an influence on the surface energy of the treated BOPP films, the laboratory scale DBD system was utilised again. The dopant gases were acetylene, nitrous oxide and carbon dioxide. Three gas cylinders with nitrogen gas doped with one of the reactive gases with concentration of 500 ppm were bought from the BOC group plc. By applying different pressures on the pure nitrogen gas line and the gas cartridges, the four different concentrations of the admixtures 125 ppm, 250 ppm, 375 ppm and 500 ppm were achieved in the gas chamber of the laboratory DBD system. The used pressure settings are listed in Table 11.

Table 11: Different pressure settings for the nitrogen gas line and the gas cartridge for achieving the different concentrations of the admixtures in the nitrogen gas

Concentration of the admixture [ppm]	Pressure on the nitrogen gas line [bar]	Pressure on the gas cartridge with the nitrogen gas and the admixture [bar]
125	1.5	0.5
250	1.0	1.0
375	0.5	1.5
500	0.0	2.0

The settings for the surface treatment were 1.5 A on the DC power supply for the current, a gap distance of 0.5 mm and a dielectric thickness of 0.63 mm. Three samples for each concentration of the different admixtures were treated with the three toothed sawtooth configuration. The contact angle measurements with water, ethylene glycol and diiodomethane were immediately conducted after the surface treatment on one of the three samples for each test liquid, whereby ten contact angles were conducted. The calculation of the dispersive part,

the polar part and the surface energy was conducted with the averaged value of the ten measurements. The error was estimated in the same way, as already made in Section 11.1. The results are presented in Figure 78 for the acetylene dopant, in Figure 79 for the nitrous oxide dopant and in Figure 80 for the carbon dioxide dopant.

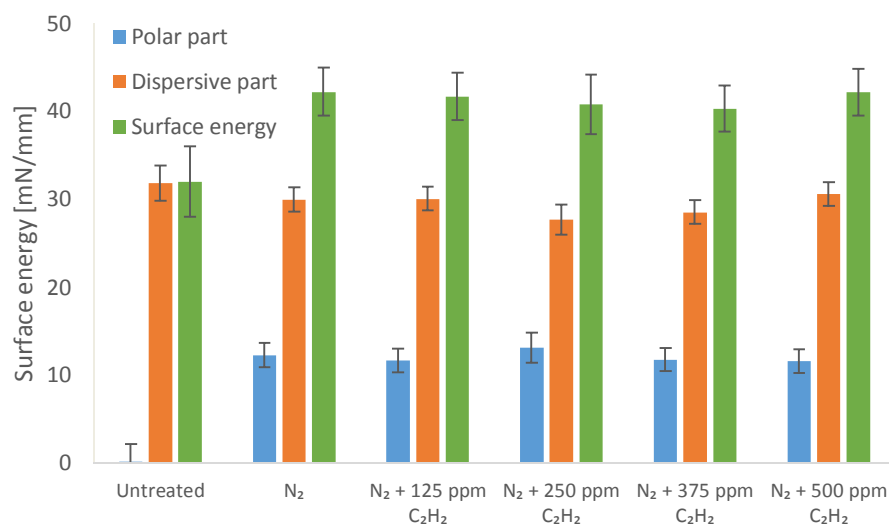


Figure 78: The polar part, the dispersive part and the surface energy of the BOPP films treated by the laboratory DBD system with admixtures of acetylene

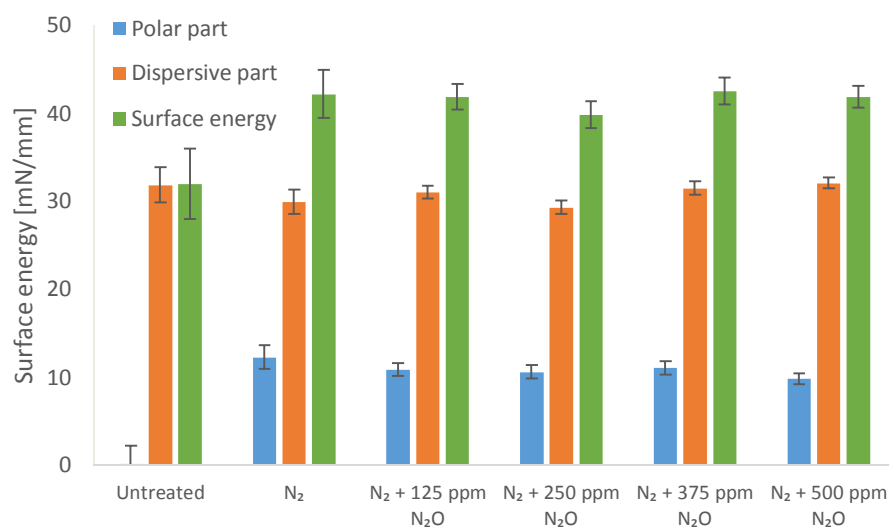


Figure 79: The polar part, the dispersive part and the surface energy of the BOPP films treated by the laboratory DBD system with admixtures of nitrous oxide

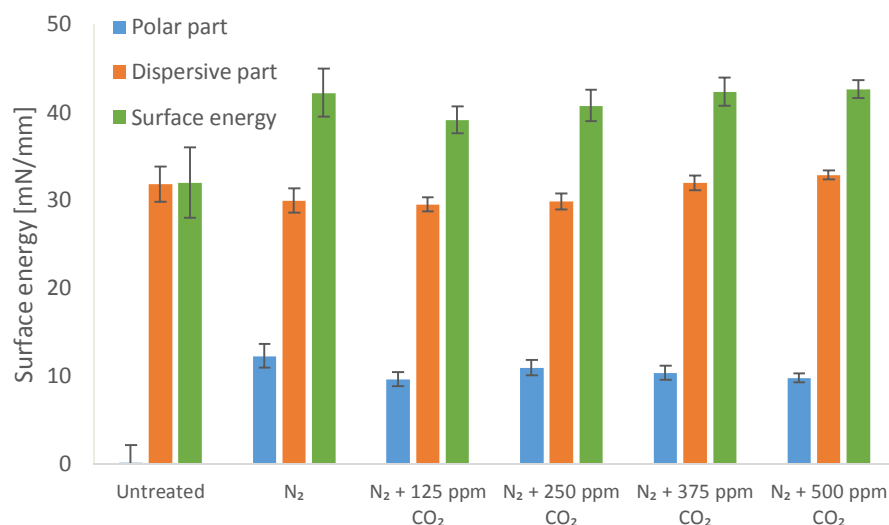


Figure 80: The polar part, the dispersive part and the surface energy of the BOPP films treated by the laboratory DBD system with admixtures of carbon dioxide

The investigation of the surface energies showed, that the plasma treatment significantly increases the polar part of the surface energy by approximately 12 mN/m, whereas the dispersive part stays unaffected. However, there are no significant differences for the polar part, the dispersive part or the entire surface energy between the treatment in pure nitrogen and the treatment in nitrogen with the different admixtures, also independent of the utilised concentration. Thereby, there is no influence of the admixtures on the surface energy of the BOPP films treated by the laboratory DBD system for concentrations of the admixtures in the nitrogen gas up to 500 ppm.

To investigate the aging behaviour of the samples treated by the laboratory DBD system, three additional samples were treated in nitrogen with the same settings of the DBD configuration. The contact angles were measured 30 days after the treatment with water, ethylene glycol and diiodomethane. The results for the polar part, the dispersive part and the entire surface energy are presented in Figure 81.

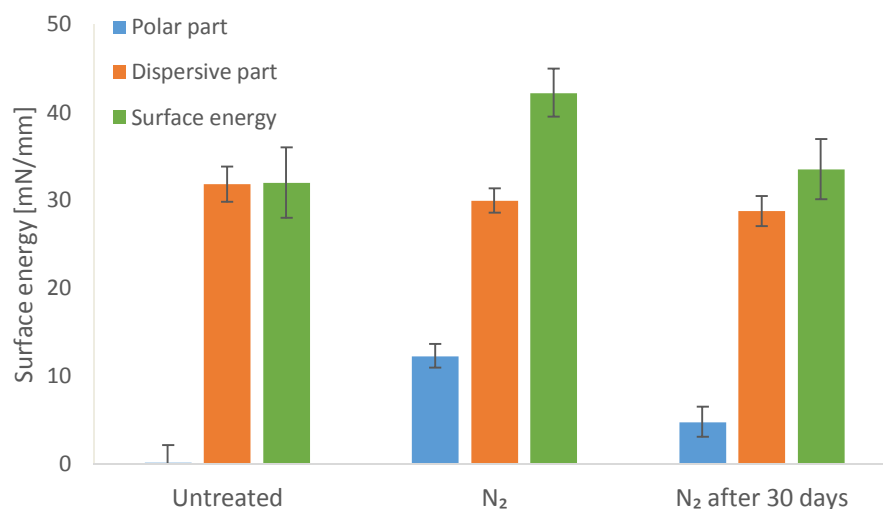


Figure 81: Aging behaviour of the BOPP samples treated in nitrogen with the laboratory DBD system

The results of Figure 81 indicate, that the surface energy of the BOPP films is reduced 30 days after the plasma treatment with the laboratory DBD system. The polar part decreases from approximately 12 mN/m to 5 mN/m while the dispersive part is not affected neither by the plasma treatment nor by the hydrophobic recovery. The entire surface energy is 30 days after the plasma treatment only slightly higher than the untreated sample.

This result is the complete opposite of the findings obtained with the surface treatments by the industrial DBD system, whose samples showed only a slow decrease of the surface energy during 30 days (shown in Figure 71). This means the utilisation of the nitrogen gas is not the only requirement for receiving surface treated BOPP films with slow hydrophobic recovery.

The surface treatment with the laboratory DBD system increased only the polar part of the treated BOPP films (shown in Figure 78, Figure 79 and Figure 80), whereas the plasma treatment with the industrial DBD system enhanced the polar part, as well as the dispersive part of the surface energy (shown in Figure 69 and Figure 70). The increase of the polar part is ascribed to the incorporation of electronegative chemical groups on the surface of the treated polymer. The reason for the increase of the dispersive part is the crosslinking between the polymer chains due to the plasma treatment.

The hydrophobic recovery of the plasma treated films is related to the rearrangement of the polymer chains at the surface, which carry the electronegative chemical groups. The rearrangement leads to the reorientation of the electronegative chemical groups from the surface towards the bulk of the polymer and thus to the reduction of the polar part of the surface energy. This behaviour could be observed for the surface energy of the BOPP films treated by the laboratory DBD system.

The BOPP films treated by the industrial DBD system showed an increase of the polar and of the dispersive part of the surface energy. This means, that electronegative chemical groups are attached to the surface of the polymer foil and in addition the polymer chains underwent some crosslinking through the plasma treatment. The estimated hydrophobic recovery of these films was strongly reduced in comparison to the films treated by the laboratory DBD system. An explanation for this behaviour is, that the crosslinking between the polymer chains hinder the rearrangement of the polymer chains. The electronegative chemical groups can thus keep their position at the surface of the polymer longer and the surface energy is reduced slower. The crosslinking of the polymer chains leads to the kinetic inhibition of the hydrophobic recovery.

The biggest difference between the surface treatment of the laboratory and the industrial DBD system is probably the amount of applied power to the nitrogen gas. For the comparison of two polymer films treated by two different DBD systems, the energy density applied to the polymer film,  $W_d$ , is utilised [90]. This value is calculated by dividing the product of the discharge area,  $A_{dis}$ , of the gap size,  $d$ , and the speed of the polymer film through the plasma,  $v$ , from the product of the discharge power,  $P_d$ , and the width of the electrode,  $h$ . The quotient of the width of the electrode,  $h$ , and of the speed of the film,  $v$ , is the residence time of the film in the plasma.

$$W_d = \frac{P_d \cdot h}{A_{dis} \cdot d \cdot v} \quad (30)$$

The calculation of the discharge power for the industrial DBD system was not possible, because the incorporation of a measurement capacitor in the high voltage circuit of the industrial DBD system was not permitted. Therefore, only a rough estimation of the two different energy densities are undertaken by replacing the discharge power by the power applied to the electrodes. The different characteristics of the two DBD systems are listed in Table 12.

Table 12: Characteristics for the rough estimation of the energy densities of the surface treatments with the laboratory and the industrial DBD system

	<b>Laboratory DBD system</b>	<b>Industrial DBD system</b>
Applied power	50 W	4 × 20 kW
Electrode area	11 cm <sup>2</sup>	4 × 1800 cm <sup>2</sup>
Speed of the polymer film	0.37 m/s	4.6 m/s
Gap size	0.5 mm	0.9 mm
Width of the electrode	25 mm	4 × 150 mm

The result of the energy density for the laboratory DBD system is  $6.1 \times 10^3$  kW/m<sup>3</sup>s and for the industrial DBD system  $1.6 \times 10^4$  kW/m<sup>3</sup>s. However, these values were calculated with the power applied to the electrodes and not with the discharge power. Therefore, the differences concerning the dielectric, such as the thickness and the material, were not considered in the calculation.

Nevertheless, it is recognisable, that the energy density applied to the BOPP film is about three times higher for the industrial DBD system than for the laboratory system. It is assumed, that the higher energy density is the reason for the crosslinking of the BOPP polymer chains, which leads to the increase of the dispersive part of the surface energy and to the kinetic inhibition of the hydrophobic recovery. But of course, this theory must be validated by further experiments. This will be part of the future work.

## 12 Conclusions

The aim of this PhD-project was the investigation of the DBD in nitrogen at atmospheric pressure as a surface treatment method for BOPP packaging foils. Therefore, a laboratory DBD system, consisting of a high voltage power supply, a gas chamber, a reel-to-reel system and different electrode configurations, was designed, built and implemented. Suitable factors were chosen to study their influence on the wettability of the treated polymer films. The factors were optimised by a D-optimal design of experiment.

The D-optimal experimental arrays revealed that the surface treatment with the sawtooth electrode configuration is superior regarding the increase of the surface energy and the power consumption in comparison to the flat electrode configuration. The investigation of the factors: current set on the DC power supply, the thickness of the dielectric and the size of the gas gap showed that an increased current and a low gas gap lead to an increased wettability of the treated films, if a sawtooth electrode is utilised. The experimental array with the flat electrode configuration demonstrated, that the dependence of the current setting on the surface energy is identical to the experiments with the sawtooth electrode, but the size of the gas gap has no influence on the wettability, if the flat electrode configuration is used. The thickness of the dielectric had for both electrode configurations no influence on the surface energy, but it is the main factor influencing the power consumed, which is increased with an increase of the dielectric thickness.

The investigations of the aging behaviour of the industrially treated samples revealed that the hydrophobic recovery of samples treated in the nitrogen plasma is slow. That is an important advantage over the more common plasma treatment in air, since treated films in an air plasma lose the main part of the increased surface energy in the first days after the surface treatment. The reduced hydrophobic recovery of the samples treated in the nitrogen plasma is connected to the crosslinking of the polymer chains on the surface of the treated BOPP foils. This is indicated by the increase of the dispersive part of the surface energy.

The samples industrially treated in nitrogen with a concentration up to 100 ppm of the reactive gases nitrous oxide or acetylene did not show a measurable difference to the samples treated in pure nitrogen. The same is valid for the samples treated by the laboratory DBD system with concentrations of nitrous oxide, acetylene or carbon dioxide with up to 500 ppm. However, the samples treated with the laboratory DBD system had a faster hydrophobic recovery and no increase of the dispersive part of the surface energy in comparison to the

industrially treated BOPP films. This fact led to the consideration, that the energy density applied to the polymer film is an important factor, which strongly influences the surface chemistry of the plasma treatment.

## 13 Future work

Based on the findings during this PhD-project, a number of open questions and further optimisations for the DBD configuration remain. These are:

The influence of the dielectric thickness on the surface treatment was intensely studied. However, no work was carried out about the type of dielectric utilised between the electrodes. Especially, the influence of the relative permittivity of the dielectric material on the consumed power and the plasma intensity would open the way for further improvements of the DBD technology.

During this project, only the filamentary discharge could be ignited. With a power supply, which is able to apply the electrical field for a duration lower than 100 ns to the nitrogen gas, also the homogeneous glow discharge could be utilised for the surface treatment of the BOPP films. The homogeneous plasma could add further improvement to the treated films in comparison to the filamentary discharge.

The surface topography of the treated films could be investigated by the atomic force microscopy. The influence of the plasma on the surface roughness of the treated films and the influence of the roughness on the increased surface energy would be interesting.

The energy density applied to the BOPP films during the surface treatment seems to be an important factor for the crosslinking of the polymer chains on the surface of the polymer foil. However, this theory needs more evidence. This could be done by the surface treatment of the BOPP samples with the industrial DBD system at different power settings. If the increase of the dispersive part of the surface energy would be lowered with reduced power applied to the electrodes, a strong argument for the made assumption would be found.

The hydrophobic recovery of the BOPP films treated by the industrial DBD system was observed for 30 days. This time scale should be increased until the surface energy reaches a stable value. This would provide detailed information about how long the treated films can be stored before processing by printing or lamination.

## 14 References

1. Thomas, M. and K.L. Mittal, *Atmospheric Pressure Plasma Treatment of Polymers: Relevance to Adhesion*. 2013: Wiley.
2. Upadhyay, D.J., et al., *Surface oxygenation of polypropylene using an air dielectric barrier discharge: the effect of different electrode-platen combinations*. *Applied Surface Science*, 2004. **229**(1-4): p. 352-364.
3. Weikart, C.M. and H.K. Yasuda, *Modification, degradation, and stability of polymeric surfaces treated with reactive plasmas*. *Journal of Polymer Science Part a-Polymer Chemistry*, 2000. **38**(17): p. 3028-3042.
4. Kogoma, M., M. Kusano, and Y. Kusano, *Generation and Application of Atmospheric Pressure Plasmas 2011*, New York: Nova Science Publishers, Inc.
5. Bardos, L. and H. Barankova, *Cold atmospheric plasma: Sources, processes, and applications*. *Thin Solid Films*, 2010. **518**(23): p. 6705-6713.
6. Boulos, I., P. Fauchais, and E. Pfender, *Thermal Plasmas*. 1994: Springer.
7. Meichsner, J., et al., *Nonthermal Plasma Chemistry and Physics*. 2012: CRC PressINC.
8. Tendero, C., et al., *Atmospheric pressure plasmas: A review*. *Spectrochimica Acta Part B-Atomic Spectroscopy*, 2006. **61**(1): p. 2-30.
9. Wagner, H.E., et al., *The barrier discharge: basic properties and applications to surface treatment*. *Vacuum*, 2003. **71**(3): p. 417-436.
10. Arora, R. and W. Mosch, *High Voltage and Electrical Insulation Engineering*. 2011: Wiley.
11. Pappas, D., *Status and potential of atmospheric plasma processing of materials*. *Journal of Vacuum Science & Technology A*, 2011. **29**(2).
12. Roth, J.R., et al., *The physics and phenomenology of one atmosphere uniform glow discharge plasma (OAUGDP (TM)) reactors for surface treatment applications*. *Journal of Physics D-Applied Physics*, 2005. **38**(4): p. 555-567.
13. Roth, J.R., *Industrial Plasma Engineering: Volume 1: Principles*. 2002: Taylor & Francis.
14. Kogelschatz, U., *Collective phenomena in volume and surface barrier discharges*, in *25th Summer School and International Symposium on the Physics of Ionized Gases - Spig 2010*, L.C. Popovic and M.M. Kuraica, Editors. 2010, Iop Publishing Ltd: Bristol.
15. Shamiri, A., et al., *The Influence of Ziegler-Natta and Metallocene Catalysts on Polyolefin Structure, Properties, and Processing Ability*. *Materials*, 2014. **7**(7): p. 5069-5108.
16. Lotz, B., S. Graff, and J.C. Wittmann, *Crystal morphology of the  $\gamma$  (triclinic) phase of isotactic polypropylene and its relation to the  $\alpha$  phase*. *Journal of Polymer Science Part B: Polymer Physics*, 1986. **24**(9): p. 2017-2032.

17. Natta, G. and P. Corradini, *Structure and properties of isotactic polypropylene*. *Il Nuovo Cimento* (1955-1965), 1960. **15**: p. 40-51.
18. Wagner, J.R., *Multilayer Flexible Packaging: Technology and Applications for the Food, Personal Care, and Over-the-Counter Pharmaceutical Industries*. *Plastics Design Library*. 2009: Elsevier Science.
19. Cáceres, C.A., et al., *Controlling in-line the energy level applied during the corona treatment*. *Polymer Testing*, 2012. **31**(4): p. 505-511.
20. Aerts, R., et al., *Gas Purification by Nonthermal Plasma: A Case Study of Ethylene*. *Environmental Science & Technology*, 2013. **47**(12): p. 6478-6485.
21. Assadi, A.A., et al., *Use of DBD plasma, photocatalysis, and combined DBD plasma/photocatalysis in a continuous annular reactor for isovaleraldehyde elimination - Synergetic effect and byproducts identification*. *Chemical Engineering Journal*, 2014. **254**: p. 124-132.
22. Moon, J.D. and J.S. Jung, *Effective corona discharge and ozone generation from a wire-plate discharge system with a slit dielectric barrier*. *Journal of Electrostatics*, 2007. **65**(10-11): p. 660-666.
23. Sun, Y.Z., F. Zhang, and leee, *Investigation of influencing factors in ozone generation using dielectric barrier discharge*. *Icpadm 2009: Proceedings of the 9th International Conference on Properties and Applications of Dielectric Materials*, Vols 1-3. 2009. 614-617.
24. Ueno, H., S. Kawahara, and H. Nakayama, *Fundamental Study of Barrier Discharge and Ozone Generation Characteristics for Multiple Needles to Plane Configuration*. *Ozone-Science & Engineering*, 2011. **33**(2): p. 98-105.
25. Falkenstein, Z. *Surface cleaning mechanisms utilizing VUV radiation in oxygen containing gaseous environments*. in *Conference on Lithographic and Micromachining Techniques for Optical Component Fabrication*. 2001. San Diego, Ca.
26. Helmke, A., et al., *Impact of Electrode Design, Supply Voltage and Interelectrode Distance on Safety Aspects and Characteristics of a Medical DBD Plasma Source*. *Contributions to Plasma Physics*, 2013. **53**(9): p. 623-638.
27. Schwabedissen, A., et al., *PlasmaLabel - A new method to disinfect goods inside a closed package using dielectric barrier discharges*. *Contributions to Plasma Physics*, 2007. **47**(7): p. 551-558.
28. Kogelschatz, U., B. Eliasson, and W. Egli, *From ozone generators to flat television screens: history and future potential of dielectric-barrier discharges*. *Pure and Applied Chemistry*, 1999. **71**(10): p. 1819-1828.
29. Sujar-Garrido, P., et al., *Dielectric barrier discharge plasma actuator to control turbulent flow downstream of a backward-facing step*. *Experiments in Fluids*, 2015. **56**(4).
30. Yan, H.J., et al., *Effect of a direct current bias on the electrohydrodynamic performance of a surface dielectric barrier discharge actuator for airflow control*. *Journal of Applied Physics*, 2015. **117**(6).

31. Bobkova, E. and V. Rybkin, *Peculiarities of Energy Efficiency Comparison of Plasma Chemical Reactors for Water Purification from Organic Substances*. Plasma Chemistry and Plasma Processing, 2015. **35**(1): p. 133-142.
32. Rodriguez-Mendez, B.G., et al., *Bacterial inactivation in water by means of a combined process of pulsed dielectric barrier discharge and silver-modified natural zeolite*. Journal of Physics D-Applied Physics, 2014. **47**(23).
33. Lin, Q.F., et al., *Degradation of Alizarin Red by Hybrid Gas-Liquid Dielectric Barrier Discharge*. Plasma Science & Technology, 2014. **16**(11): p. 1036-1041.
34. Shibata, T. and H. Nishiyama, *Acetic Acid Decomposition in a Coaxial Dielectric Barrier Discharge Tube with Mist Flow*. Plasma Chemistry and Plasma Processing, 2014. **34**(6): p. 1331-1343.
35. Belmonte, T., G. Henrion, and T. Gries, *Nonequilibrium Atmospheric Plasma Deposition*. Journal of Thermal Spray Technology, 2011. **20**(4): p. 744-759.
36. Cai, L., et al., *Optimization of saturation current density of PECVD SiN coated phosphorus diffused emitters using neural network modeling*. Journal of Electronic Materials, 1996. **25**(11): p. 1784-1789.
37. Cheng, L.L., et al., *Preparation of SnS films using solid sources deposited by the PECVD method with controllable film characters*. Journal of Alloys and Compounds, 2012. **545**: p. 122-129.
38. Elgamel, H.E.A., *High efficiency polycrystalline silicon solar cells using low temperature PECVD process*. IEEE Transactions on Electron Devices, 1998. **45**(10): p. 2131-2137.
39. Lee, J., et al., *Enhancement of Interface Properties between Passivation Layers and InSb by Using Remote PECVD*. Physics of Semiconductors: 30th International Conference on the Physics of Semiconductors, 2011. **1399**.
40. Massines, F., et al., *Atmospheric Pressure Low Temperature Direct Plasma Technology: Status and Challenges for Thin Film Deposition*. Plasma Processes and Polymers, 2012. **9**(11-12): p. 1041-1073.
41. Nagasawa, H., et al., *Characterization and gas permeation properties of amorphous silica membranes prepared via plasma enhanced chemical vapor deposition*. Journal of Membrane Science, 2013. **441**: p. 45-53.
42. Premkumar, P.A., et al., *Smooth and Self-Similar SiO<sub>2</sub>-like Films on Polymers Synthesized in Roll-to-Roll Atmospheric Pressure-PECVD for Gas Diffusion Barrier Applications*. Plasma Processes and Polymers, 2010. **7**(8): p. 635-639.
43. Schafer, J., et al., *Complex analysis of SiO<sub>x</sub>CyHz films deposited by an atmospheric pressure dielectric barrier discharge*. Surface & Coatings Technology, 2011. **205**: p. S330-S334.
44. Silva, J.A., et al., *Feasibility of antireflection and passivation coatings by atmospheric pressure PECVD*. Proceedings of the 4th International

- Conference on Crystalline Silicon Photovoltaics (Siliconpv 2014), 2014. **55**: p. 741-749.
45. Kogelschatz, U., *Filamentary, patterned, and diffuse barrier discharges*. IEEE Transactions on Plasma Science, 2002. **30**(4): p. 1400-1408.
46. Kogelschatz, U., *Dielectric-barrier discharges: Their history, discharge physics, and industrial applications*. Plasma Chemistry and Plasma Processing, 2003. **23**(1): p. 1-46.
47. Massines, F. and G. Gouda, *A comparison of polypropylene-surface treatment by filamentary, homogeneous and glow discharges in helium at atmospheric pressure*. Journal of Physics D-Applied Physics, 1998. **31**(24): p. 3411-3420.
48. Raether, H., *Die Entwicklung der Elektronenlawine in den Funkenkanal*. Zeitschrift für Physik, 1939. **112**(7-8): p. 464-489.
49. Raether, H., *Development of Kanal discharge*. Archiv für Elektrotechnik, 1940. **34**: p. 49-56.
50. Loeb, L.B. and J.M. Meek, *The Mechanism of Spark Discharge in Air at Atmospheric Pressure. I*. Journal of Applied Physics, 1940. **11**(6): p. 438-447.
51. Chu, P.K., *Low temperature plasma technology : methods and applications*. 2014.
52. Massines, F., et al., *Physics and chemistry in a glow dielectric barrier discharge at atmospheric pressure: diagnostics and modelling*. Surface & Coatings Technology, 2003. **174**: p. 8-14.
53. Kanazawa, S., et al., *STABLE GLOW PLASMA AT ATMOSPHERIC-PRESSURE*. Journal of Physics D-Applied Physics, 1988. **21**(5): p. 838-840.
54. Okazaki, S., et al., *APPEARANCE OF STABLE GLOW-DISCHARGE IN AIR, ARGON, OXYGEN AND NITROGEN AT ATMOSPHERIC-PRESSURE USING A 50-HZ SOURCE*. Journal of Physics D-Applied Physics, 1993. **26**(5): p. 889-892.
55. Massines, F., et al., *Glow and Townsend dielectric barrier discharge in various atmosphere*. Plasma Physics and Controlled Fusion, 2005. **47**: p. B577-B588.
56. Massines, F., et al., *Recent advances in the understanding of homogeneous dielectric barrier discharges*. European Physical Journal-Applied Physics, 2009. **47**(2).
57. Massines, F., et al., *The Role of Dielectric Barrier Discharge Atmosphere and Physics on Polypropylene Surface Treatment*. Plasmas and Polymers, 2001. **6**(1): p. 35-49.
58. Golubovskii, Y.B., et al., *Effect of the barrier material in a Townsend barrier discharge in nitrogen at atmospheric pressure*. Journal of Physics D-Applied Physics, 2006. **39**(8): p. 1574-1583.
59. Es-sebbar, E., N. Gherardi, and F. Massines, *Effects of N<sub>2</sub>O and O<sub>2</sub> addition to nitrogen Townsend dielectric barrier discharges at atmospheric*

- pressure on the absolute ground-state atomic nitrogen density*. Journal of Physics D-Applied Physics, 2013. **46**(1).
60. Naude, N., et al., *Electrical model and analysis of the transition from an atmospheric pressure Townsend discharge to a filamentary discharge*. Journal of Physics D-Applied Physics, 2005. **38**(4): p. 530-538.
  61. Luo, H.Y., et al., *Homogeneous dielectric barrier discharge in nitrogen at atmospheric pressure*. Journal of Physics D-Applied Physics, 2010. **43**(15).
  62. Gherardi, N. and F. Massines, *Mechanisms controlling the transition from glow silent discharge to streamer discharge in nitrogen*. Ieee Transactions on Plasma Science, 2001. **29**(3): p. 536-544.
  63. Li, F.L., et al., *Numerical Investigation of a Parallel-Plate Atmospheric-Pressure Nitrogen/Ammonia Dielectric Barrier Discharge*. Plasma Chemistry and Plasma Processing, 2012. **32**(3): p. 547-564.
  64. Starostin, S.A., et al., *On the formation mechanisms of the diffuse atmospheric pressure dielectric barrier discharge in CVD processes of thin silica-like films*. Plasma Sources Science & Technology, 2009. **18**(4).
  65. Bogaczyk, M., et al., *Spatio-temporally Resolved Investigation of Surface Charges, N-2(A(3)Sigma(+)(u)) Metastables and Discharge Development in Barrier Discharges*. Journal of Advanced Oxidation Technologies, 2012. **15**(2): p. 310-320.
  66. Bogaczyk, M., et al., *Surface charge accumulation and discharge development in diffuse and filamentary barrier discharges operating in He, N<sub>2</sub> and mixtures*. Journal of Physics D: Applied Physics, 2012. **45**(46): p. 465202.
  67. Brandenburg, R., et al., *The transition between different modes of barrier discharges at atmospheric pressure*. Journal of Physics D-Applied Physics, 2009. **42**(8).
  68. Gherardi, N., et al., *Transition from glow silent discharge to micro-discharges in nitrogen gas*. Plasma Sources Science & Technology, 2000. **9**(3): p. 340-346.
  69. Ayan, H., et al., *Application of nanosecond-pulsed dielectric barrier discharge for biomedical treatment of topographically non-uniform surfaces*. Journal of Physics D-Applied Physics, 2009. **42**(12).
  70. Ayan, H., et al., *Nanosecond-pulsed uniform dielectric-barrier discharge*. Ieee Transactions on Plasma Science, 2008. **36**(2): p. 504-508.
  71. Jiang, H., et al., *Comparison of AC and Nanosecond-Pulsed DBDs in Atmospheric Air*. Ieee Transactions on Plasma Science, 2011. **39**(11): p. 2076-2077.
  72. Zhang, S., et al., *Atmospheric-Pressure Diffuse Dielectric-Barrier-Discharge Plasma Generated by Bipolar Nanosecond Pulse in Nitrogen and Air*. Ieee Transactions on Plasma Science, 2012. **40**(9): p. 2191-2197.
  73. Shao, T., et al., *A Comparative Study of Water Electrodes Versus Metal Electrodes for Excitation of Nanosecond-Pulse Homogeneous Dielectric*

- Barrier Discharge in Open Air*. Ieee Transactions on Plasma Science, 2013. **41**(10): p. 3069-3078.
74. Zhang, S., et al., *Comparison of atmospheric air plasmas excited by high-voltage nanosecond pulsed discharge and sinusoidal alternating current discharge*. Journal of Applied Physics, 2013. **114**(16).
75. Yang, D.Z., et al., *A diffusive air plasma in bi-directional nanosecond pulsed dielectric barrier discharge*. Journal of Physics D-Applied Physics, 2010. **43**(45).
76. Shao, T., et al., *Discharge characteristic of nanosecond-pulse DBD in atmospheric air using magnetic compression pulsed power generator*. Vacuum, 2012. **86**(7): p. 876-880.
77. Xu, D.A., et al., *Experimental study of the hydrodynamic expansion following a nanosecond repetitively pulsed discharge in air*. Applied Physics Letters, 2011. **99**(12).
78. Li, L., et al., *Generating diffuse discharge via repetitive nanosecond pulses and line-line electrodes in atmospheric air*. Review of Scientific Instruments, 2013. **84**(10).
79. Shao, T., et al., *Generation of Atmospheric Pressure Plasma by Repetitive Nanosecond Pulses in Air Using Water Electrodes*. Plasma Science & Technology, 2011. **13**(6): p. 735-739.
80. Yang, D.-Z., et al., *A homogeneous dielectric barrier discharge plasma excited by a bipolar nanosecond pulse in nitrogen and air*. Plasma Sources Science & Technology, 2012. **21**(3).
81. Shao, T., et al., *ICCD Observation of Homogeneous DBD Excited by Unipolar Nanosecond Pulses in Open Air*. Ieee Transactions on Plasma Science, 2011. **39**(11): p. 2062-2063.
82. Yang, D.Z., et al., *Production of atmospheric pressure diffuse nanosecond pulsed dielectric barrier discharge using the array needles-plate electrode in air*. Journal of Applied Physics, 2011. **109**(7).
83. Walsh, J.L. and M.G. Kong, *10 ns pulsed atmospheric air plasma for uniform treatment of polymeric surfaces*. Applied Physics Letters, 2007. **91**(25).
84. Jia, L., et al., *A diffuse plasma generated by bipolar nanosecond pulsed dielectric barrier discharge in nitrogen*. European Physical Journal D, 2014. **68**(5).
85. Choi, Y.H., J.H. Kim, and Y.S. Hwang, *One-dimensional discharge simulation of nitrogen DBD atmospheric pressure plasma*. Thin Solid Films, 2006. **506**: p. 389-395.
86. Cheng, K.W., et al., *One-dimensional simulation of nitrogen dielectric barrier discharge driven by a quasi-pulsed power source and its comparison with experiments*. Computer Physics Communications, 2011. **182**(1): p. 164-166.
87. Khamphan, C., et al. *Secondary electron emission by nitrogen metastable states in atmospheric-pressure glow discharge*.

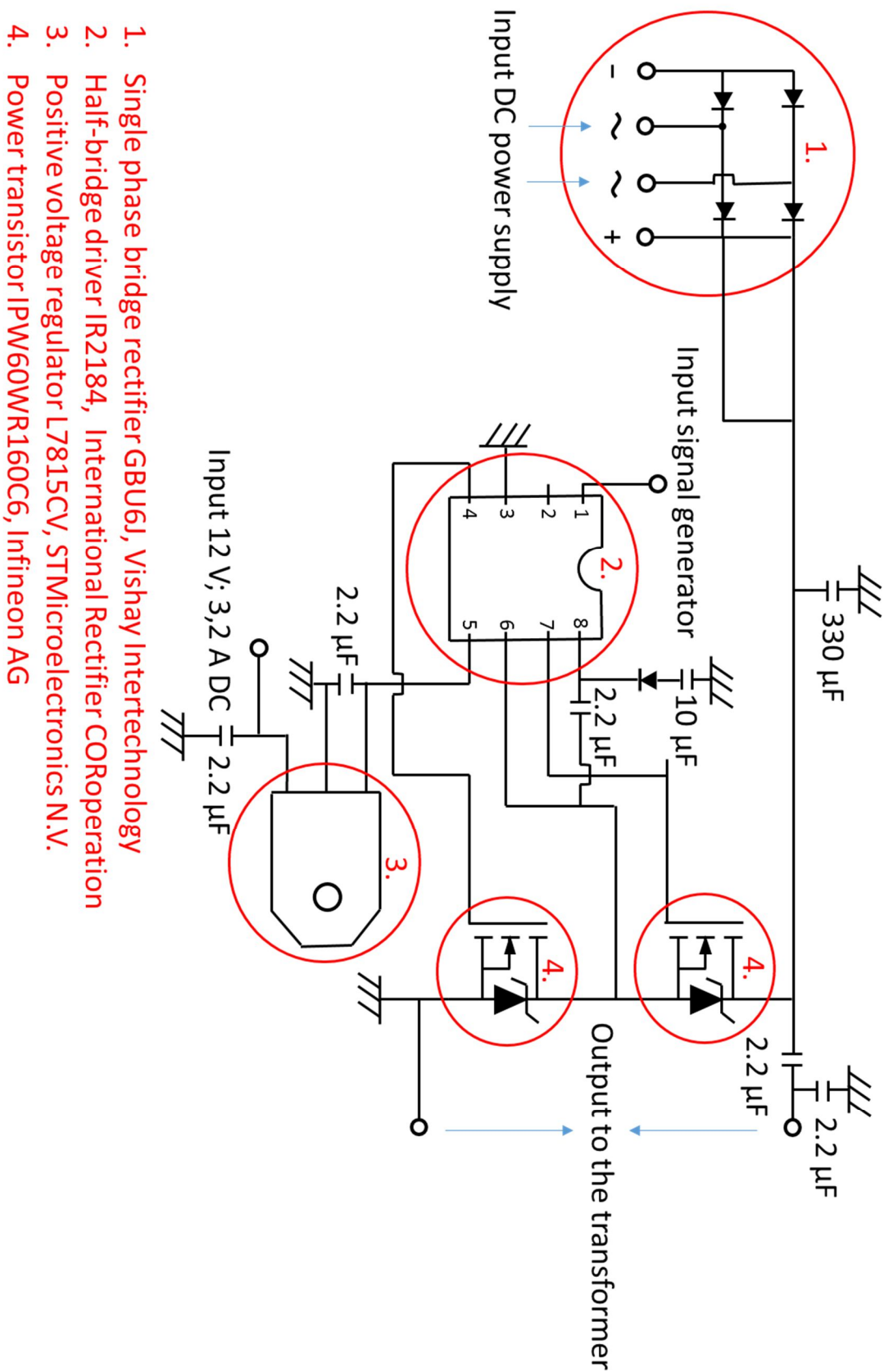
88. Calvert, P.D., *Polymer degradation and stabilisation*. N. Grassie and G. Scott, Cambridge University Press, Cambridge, 1985. pp. 222, price £27.50, \$54.50. ISBN 0-521-24961-9. British Polymer Journal, 1986. **18**(4): p. 278-278.
89. Bhat, N.V. and D.J. Upadhyay, *Plasma-induced surface modification and adhesion enhancement of polypropylene surface*. Journal of Applied Polymer Science, 2002. **86**(4): p. 925-936.
90. Guimond, S., et al., *Biaxially oriented polypropylene (BOPP) surface modification by nitrogen atmospheric pressure glow discharge (APGD) and by air corona*. Plasmas and Polymers, 2002. **7**(1): p. 71-88.
91. Wang, K., et al., *Surface modification of polypropylene non-woven fabric using atmospheric nitrogen dielectric barrier discharge plasma*. Applied Surface Science, 2010. **256**(22): p. 6859-6864.
92. Kostov, K.G., et al., *Study of polypropylene surface modification by air dielectric barrier discharge operated at two different frequencies*. Surface & Coatings Technology, 2013. **234**: p. 60-66.
93. Nishime, T.M.C., et al., *Surface characteristics analysis of polypropylene treated by dielectric barrier discharge at atmospheric pressure*, in *14th Latin American Workshop on Plasma Physics*, L. Bilbao, F. Minotti, and H. Kelly, Editors. 2012, IOP Publishing Ltd: Bristol.
94. Grundmann, S. and C. Tropea, *Experimental damping of boundary-layer oscillations using DBD plasma actuators*. International Journal of Heat and Fluid Flow, 2009. **30**(3): p. 394-402.
95. Pipa, A.V., et al., *Experimental determination of dielectric barrier discharge capacitance*. Review of Scientific Instruments, 2012. **83**(7).
96. Wang, C.Q., G.X. Zhang, and X.X. Wang, *Comparisons of discharge characteristics of a dielectric barrier discharge with different electrode structures*. Vacuum, 2012. **86**(7): p. 960-964.
97. Young, T., *An essay on the cohesion of fluids*. Philosophical Transactions of the Royal Society of London, 1805. **95**: p. 65-87.
98. Rudawska, A. and E. Jacniacka, *Analysis for determining surface free energy uncertainty by the Owen-Wendt method*. International Journal of Adhesion and Adhesives, 2009. **29**(4): p. 451-457.
99. Fowkes, F.M., *DONOR-ACCEPTOR INTERACTIONS AT INTERFACES*. Journal of Adhesion, 1972. **4**(2): p. 155-&.
100. Fowkes, F.M., *Calculation of work of adhesion by pair potential summation*. Journal of Colloid and Interface Science, 1968. **28**(3-4): p. 493-505.
101. Fowkes, F.M., *ATTRACTIVE FORCES AT INTERFACES*. Industrial & Engineering Chemistry, 1964. **56**(12): p. 40-52.
102. Owens, D.K. and R.C. Wendt, *Estimation of the surface free energy of polymers*. Journal of Applied Polymer Science, 1969. **13**(8): p. 1741-1747.

103. Van Oss, C.J., M.K. Chaudhury, and R.J. Good, *Interfacial Lifshitz-van der Waals and polar interactions in macroscopic systems*. Chemical Reviews, 1988. **88**(6): p. 927-941.
104. Wu, S., *Polar and nonpolar interactions in adhesion*. The Journal of Adhesion, 1973. **5**(1): p. 39-55.
105. Wu, S. *Calculation of interfacial tension in polymer systems*. Wiley Online Library.
106. Fox, H.W. and W.A. Zisman, *The spreading of liquids on low-energy surfaces. III. Hydrocarbon surfaces*. Journal of Colloid Science, 1952. **7**(4): p. 428-442.
107. Fox, H.W. and W.A. Zisman, *The spreading of liquids on low-energy surfaces. II. Modified tetrafluoroethylene polymers*. Journal of Colloid Science, 1952. **7**(2): p. 109-121.
108. Rabel, W., *Einige Aspekte der Benetzungstheorie und ihre Anwendung auf die Untersuchung und Veränderung der Oberflächeneigenschaften von Polymeren*. Farbe und Lack, 1971. **77**(10): p. 997-1006.
109. Kaelble, D.H., *Dispersion-polar surface tension properties of organic solids*. 1970.
110. Żenkiewicz, M., *Methods for the calculation of surface free energy of solids*. Journal of Achievements in Materials and Manufacturing Engineering, 2007. **24**(1): p. 137-145.
111. Kwok, D.Y. and A.W. Neumann, *Contact angle measurement and contact angle interpretation*. Advances in Colloid and Interface Science, 1999. **81**(3): p. 167-249.
112. Leroux, F., et al., *Polypropylene film chemical and physical modifications by dielectric barrier discharge plasma treatment at atmospheric pressure*. Journal of Colloid and Interface Science, 2008. **328**(2): p. 412-420.
113. Šíra, M., et al., *Surface modification of polyethylene and polypropylene in atmospheric pressure glow discharge*. Journal of physics D: Applied physics, 2005. **38**(4): p. 621.
114. Milling, A.J., *Surface characterization methods: principles, techniques, and applications*. Vol. 87. 1999: CRC Press.
115. Krüss-GmbH. *Young-Laplace fit*. <http://www.kruss.de/de/service/schulung-theorie/glossar/young-laplace-fit/> [14/06/2015].
116. Wolf, R.A., *Atmospheric pressure plasma for surface modification*. 2012: John Wiley & Sons.
117. Stojilovic, N., *Why Can't We See Hydrogen in X-ray Photoelectron Spectroscopy?* Journal of Chemical Education, 2012. **89**(10): p. 1331-1332.
118. Eriksson, L., *Design of experiments: principles and applications*. 2008: MKS Umetrics AB.
119. Plackett, R.L. and J.P. Burman, *The design of optimum multifactorial experiments*. Biometrika, 1946: p. 305-325.

120. Taguchi, G., *Introduction to quality engineering: designing quality into products and processes*. 1986.
121. Shah, K.R. and B.K. Sinha, *Theory of optimal designs*. Vol. 54. 2012: Springer Science & Business Media.
122. Stryczewska, H.D., et al., *Power systems of plasma reactors for non-thermal plasma generation*. Journal of Advanced Oxidation Technologies, 2013. **16**(1): p. 52-62.
123. Meiners, A., M. Leck, and B. Abel, *Efficiency enhancement of a dielectric barrier plasma discharge by dielectric barrier optimization*. Review of Scientific Instruments, 2010. **81**(11).
124. Osawa, N., et al., *Generation of Uniform Discharge by Dielectric Barrier Discharge Device in Atmospheric-pressure Air*. Electrical Engineering in Japan, 2012. **180**(4): p. 1-9.
125. Osawa, N. and Y. Yoshioka, *Generation of Low-Frequency Homogeneous Dielectric Barrier Discharge at Atmospheric Pressure*. IEEE Transactions on Plasma Science, 2012. **40**(1): p. 2-8.
126. Cernak, M., et al., *Generation of a high-density highly non-equilibrium air plasma for high-speed large-area flat surface processing*. Plasma Physics and Controlled Fusion, 2011. **53**(12).
127. Cernakova, L., et al., *Surface modification of polypropylene non-woven fabrics by atmospheric-pressure plasma activation followed by acrylic acid grafting*. Plasma Chemistry and Plasma Processing, 2005. **25**(4): p. 427-437.
128. Wang, C.Q. and X.N. He, *Polypropylene surface modification model in atmospheric pressure dielectric barrier discharge*. Surface & Coatings Technology, 2006. **201**(6): p. 3377-3384.
129. Chvatalova, L., et al., *The effect of plasma treatment on structure and properties of poly(1-butene) surface*. European Polymer Journal, 2012. **48**(4): p. 866-874.
130. Cui, N.Y. and N.M.D. Brown, *Modification of the surface properties of a polypropylene (PP) film using an air dielectric barrier discharge plasma*. Applied Surface Science, 2002. **189**(1-2): p. 31-38.
131. Wang, T., et al., *Effect of Reactor Structure in DBD for Nonthermal Plasma Processing of NO in N<sub>2</sub> at Ambient Temperature*. Plasma Chemistry and Plasma Processing, 2012. **32**(6): p. 1189-1201.
132. Changquan, W., et al., *Study on parameter optimization of polypropylene surface modification in atmospheric pressure dielectric barrier discharge*, in *2007 IEEE International Conference on Automation and Logistics*. 2007, IEEE, ELECTRON DEVICES SOC & RELIABILITY GROUP, 345 E 47TH ST, NEW YORK, NY 10017 USA: Jinan, China. p. 770-775.
133. Reichen, P., *Plasma Surface Modification in the Afterglow of Micro-barrier Discharges*. 2009, ETH Zürich: Zürich. p. 212.

134. Mangolini, L., et al., *Effects of current limitation through the dielectric in atmospheric pressure glows in helium*. Journal of Physics D: Applied Physics, 2004. **37**(7): p. 1021.
135. Sawant, S. *Find phase difference between 2 sinusoidal signals*. <http://www.mathworks.com/matlabcentral/fileexchange/29075-find-phase-difference-between-2-sinusoidal-signals> [22/01/2015].
136. Wolf, R. and A.C. Sparavigna, *Role of plasma surface treatments on wetting and adhesion*. Engineering, 2010. **2**(06): p. 397.
137. Kwon, O.-J., et al., *Surface characteristics of polypropylene film treated by an atmospheric pressure plasma*. Surface and Coatings Technology, 2005. **192**(1): p. 1-10.
138. Novak, I. and S. Florian, *Investigation of long-term hydrophobic recovery of plasma modified polypropylene*. Journal of Materials Science, 2004. **39**(6): p. 2033-2036.
139. Strobel, J.M., et al., *Aging of air-corona-treated polypropylene film*. Journal of Adhesion Science and Technology, 1991. **5**(2): p. 119-130.
140. Upadhyay, D.J., et al., *Surface oxygenation of polypropylene using an air dielectric barrier discharge: the effect of different electrode-platen combinations*. Applied surface science, 2004. **229**(1): p. 352-364.
141. Süzer, S., et al., *XPS and water contact angle measurements on aged and corona-treated PP*. Journal of applied polymer science, 1999. **74**(7): p. 1846-1850.
142. Yun, Y.I., et al., *Aging behavior of oxygen plasma-treated polypropylene with different crystallinities*. Journal of adhesion science and technology, 2004. **18**(11): p. 1279-1291.
143. Morra, M., E. Occhiello, and F. Garbassi, *Contact angle hysteresis on oxygen plasma treated polypropylene surfaces*. Journal of Colloid and Interface Science, 1989. **132**(2): p. 504-508.
144. Pascual, M., et al., *Study of the aging process of corona discharge plasma effects on low density polyethylene film surface*. Journal of materials science, 2008. **43**(14): p. 4901-4909.
145. Guimond, S. and M.R. Wertheimer, *Surface degradation and hydrophobic recovery of polyolefins treated by air corona and nitrogen atmospheric pressure glow discharge*. Journal of Applied Polymer Science, 2004. **94**(3): p. 1291-1303.
146. Hughes, I. and T. Hase, *Measurements and their uncertainties: a practical guide to modern error analysis*. 2010: Oxford University Press.

**Appendix A: Circuit diagram of the amplifier**



- 1. Single phase bridge rectifier GBU6J, Vishay Intertechnology
- 2. Half-bridge driver IR2184, International Rectifier CORoperation
- 3. Positive voltage regulator L7815CV, STMicroelectronics N.V.
- 4. Power transistor IPW60WR160C6, Infineon AG

**Appendix B: Matlab program code for the low-pass filter**

```
function y = lowpass(x)
%LOWPASS Filters input x and returns output y.

% MATLAB Code
% Generated by MATLAB(R) 8.3 and the Signal Processing Toolbox 6.21.
% Generated on: 21-Dec-2014 15:03:44

persistent Hd;

if isempty(Hd)

    Fpass = 0.004; % Passband Frequency
    Fstop = 0.009; % Stopband Frequency
    Apass = 1;     % Passband Ripple (dB)
    Astop = 60;   % Stopband Attenuation (dB)

    h = fdesign.lowpass('fp,fst,ap,ast', Fpass, Fstop, Apass, Astop);

    Hd = design(h, 'ifir');

    set(Hd, 'PersistentMemory', true);

end

y = filter(Hd,x);
```

**Appendix C: Matlab program code for calculating the phase difference**

```

Filename: givepd.m
% Author: Shashank G. Sawant
% email: sgsawant@gmail.com
% Description: Given 2 sinusoidal signals of the
% same frequency, the function gives the "phase difference" between the
% 2 given signals
% The phase difference is in RADIANS!!!!!!
% The output is limited to radians
% Time Stamp: 2010 October 19 2043hrs

% pd - output phase difference (in radians)
% v - first sinusoidal signal
% i - second sinusoidal signal
% Note: v and i should have the same frequency
function pd=givepd(v,i)
L=length(v);
if(L~=length(i))
    error('The length of the 2 sinusoidal input vectors is not same!!!');
end

% The following block calculates the FFT
NFFT = 2^nextpow2(L);
V = fft(v,NFFT)/L;           %Fourier Transform of signal v

% The following block calculates the phase of the most significant
% frequency component
[value,index]=max(2*abs(V(1:NFFT/2+1)));
pV = angle(V(index));

% The following block calculates the FFT
NFFT = 2^nextpow2(L);
I = fft(i,NFFT)/L;           %Fourier Transform of signal i

% The following block calculates the phase of the most significant
% frequency component
[value,index]=max(2*abs(I(1:NFFT/2+1)));
pI = angle(I(index));

% The following is the phase difference between the 2 signals
pd=pV-pI;

% The code below limits the output to radians
while 1
    if pd>pi
        pd=pd-2*pi;
    elseif pd<-pi
        pd=pd+2*pi;
    else
        break;
    end
end

return;
end

```

### Appendix D: Error calculation for the surface energy

The error of the slope and the y-intercept of a regression line with the equation:

$$y = m \cdot x + t$$

is given according to [146] by:

$$\Delta m = \sqrt{\frac{\Delta y}{n-2}} \cdot \sqrt{\frac{\sum_{i=1}^n x_i^2}{n \cdot \sum_{i=1}^n x_i^2 - (\sum_{i=1}^n x_i)^2}}$$

$$\Delta t = \sqrt{\frac{\Delta y}{n-2}} \cdot \sqrt{\frac{n}{n \cdot \sum_{i=1}^n x_i^2 - (\sum_{i=1}^n x_i)^2}}$$

$$\Delta y = \sum_{i=1}^n (y_i - m - t \cdot x_i)^2$$

The error of the dispersive part of the surface energy is  $\Delta t$ , the error of the polar part is  $\Delta m$  and the error of the entire surface energy is calculated by the sum of  $\Delta t$  and  $\Delta m$  according to the error propagation:

$$\Delta \gamma_s = \sqrt{\left( \frac{\partial(\gamma_s^p + \gamma_s^l)}{\partial \gamma_s^p} \cdot \Delta t \right)^2 + \left( \frac{\partial(\gamma_s^p + \gamma_s^l)}{\partial \gamma_s^l} \cdot \Delta m \right)^2} = \Delta t + \Delta m$$